Waveguide Heterodyne Mixers at THz-Frequencies — Superconducting Hot Electron Bolometers on 2-μm Si_3N_4 Membranes for GREAT and CONDOR

Inaugural-Dissertation
zur
Erlangung des Doktorgrades
der Mathematisch-Naturwissenschaftlichen Fakultät
der Universität zu Köln

vorgelegt von
Pedro Pablo Muñoz Pradas
aus Madrid in Spanien

Köln 2007

Berichterstatter: Prof. Dr. J. Stutzki

Prof. Dr. J. Jolie

Tag der mündlichen Prüfung: 23. April 2007

Abstract

Many interesting astronomical objects, such as galaxies, molecular clouds, star-forming regions, protostars, evolved stars, planets, and comets, have rich submillimeter spectra. In order to avoid line blending and to resolve line shapes, most of this information can only be obtained using high resolution spectroscopy. The incoming signals are very weak and the receiver must be therefore extremely low-noise. High resolution spectroscopy of weak sources is carried out primarily using heterodyne receivers. Direct detection is intrinsically more sensitive than heterodyne but is constrained by the spectrometers which are needed to achieve the required spectral resolution ($\sim 10^7$, see chapter 1).

In a heterodyne receiver the astronomical signal is downconverted to much lower frequencies and amplified prior to spectral analysis. Therefore, much lower relative spectral resolution is needed to achieve the same absolute spectral resolution (easily in exceed of 10^7). In the heterodyne receiver the astronomical signal is mixed with a stronger monochromatic source (Local Oscillator, LO) to the difference frequency (Intermediate Frequency, IF). A basic part of the receiver is the mixer, which is a device with a non-linear response to the signal intensity amplitude and downconverts the received signal to the IF ($\sim$ 1–10 GHz), which is then amplified. Since the mixer is the first active component in the receiver, it has the greatest influence on the total receiver noise (see chapter 1).

Best mixer performance is currently achieved with Superconductor-Insulator-Superconductor (SIS) junctions, but their highest operation frequency is intrinsically limited by the energy gap of the superconductors used. Above $\sim$1 THz superconducting phonon-cooled Hot Electron Bolometers (HEB) are nowadays the mixer of choice for heterodyne receivers. Superconducting phonon-cooled HEBs consist of an ultrathin (<5 nm) superconducting NbTiN (or NbN) layer between two normal conducting electrodes (heat sinks) and embedded in a THz coupling environment. The HEB is operated at 4.2 K. The RF power is coupled into the superconducting film. The power dissipation in the film brings it to its critical temperature ($\sim$ 8–9 K) in which a small variation in the dissipated power results in a large variation in the device resistance. The resistance change is translated into an IF voltage variation by the bias current. Since the dissipated power is proportional to the square of the sum of the signal intensities, the voltage drop over the HEB resistance is modulated at the intermediate frequency of the receiver, which can be amplified and analyzed by the following spectrometer.

The cooling performance of the HEB limits the response time in which

the HEB can follow the variations of the dissipated power and therefore its IF bandwidth. The main cooling mechanism of the superconducting layer is the phonon transport to the substrate (phonon-cooled HEB). Therefore, to enhance the IF bandwidth the superconducting NbTiN or NbN layer has to be made extremely thin (<5 nm). An IF bandwidth of at least several GHz is desired to register spectral lines with large Doppler width. This corresponds to a HEB response time τ of just some tens picoseconds.

The few groups worldwide developing HEB-based THz-receivers have concentrated on a lens-substrate mixer mount. It is easy in handling due to the thick device substrates but the coupling efficiency of a planar antenna/dielectric lens system to a Gaussian beam is often not as good as that of a high performance waveguide horn. The mixers fabricated during this thesis use waveguide mounts. Waveguide manufacturing is technically demanding at THz frequencies due to the small dimensions. Scaling the dielectric substrate to frequencies beyond 1 THz becomes increasingly difficult. In order to avoid RF loss due to waveguide modes in the substrate channel, a quartz substrate at 1.9 THz would have to be 10 μm thick or less.

Considerably thinner substrates have been realized in this thesis by fabricating the mixer device on a thin (i.e. 2 μm) membrane layer deposited on a bulk silicon carrier wafer. The membrane is released by backside etching of the wafer after device fabrication. A large supporting frame is needed around the device for handling and contacting. A possible approach is to fabricate the frame and the mixer simultaneously on one wafer. In the process presented here the membrane-HEB devices and the supporting frames are fabricated separately avoiding the loss of wafer "real estate" for the support frames and thus allowing for up to 690 devices to be simultaneously produced on a single 30 mm square wafer. Fabricating many identical devices for arrays is possible even if many devices are damaged during fabrication. Further it is possible to test many different parameter-variations on one single wafer. The price to pay is a slightly more involved assembly procedure, which has been realized for the first time for 1.4 and 1.9 THz in this thesis.

The fabrication of the phonon-cooled HEBs was fully realized at the KOSMA clean room facilities. The sputter deposition of ultra-thin NbTiN films with critical temperatures as high as 8.5 K is one of the technological highlights, already described at [1].

This thesis focused on the optimization of the contact interfaces between the electrodes and the ultrathin superconducting layer. Etching the interface previous to deposition of the electrodes leads to a better control over the interface. The effect of the etching parameters on the HEBs has been inves-

tigated. To restore the superconducting film properties that might be affected by the cleaning process, a NbTiN layer (20 nm) is deposited on top of the contact area. The additional superconducting layer between the bolometer thin film and the heat sinks has a positive effect on the mixer performance but introduced complications in the fabrication process which have been solved in this thesis.

The fabricated waveguide HEB mixers on thin silicon nitride membranes for GREAT on SOFIA and CONDOR on APEX have been demonstrated at LO frequencies of 1.4 THz and 1.9 THz with good noise performance and excellent stability (Allan Stability time over 30 s) as compared to results of the few other groups. The noise temperature shows a flat response over the measured IF-bandwidth (1.2–1.75 GHz). The 1.4 THz mixer has already been used at the APEX telescope.

Zusammenfassung

Viele interessante astronomische Objekte, wie Galaxien, Molekülwolken, Sternentstehungsregionen, Protosterne, Sterne in späten Entwicklungsstadien, Planeten und Kometen haben sehr interessante Submillimeterspektren. Die meisten dieser Informationen können jedoch nur mit hochauflösende Spektroskopie gewonnen werden, um die Überlappung von Linien zu vermeiden und die Linienform aufzulösen. Die ankommenden astronomische Signale sind jedoch äußerst schwach, so dass sehr rauscharme Empfänger für deren Nachweis erforderlich werden. Hochauflösende Spektroskopie von schwachen Quellen wird hauptsächlich mit Heterodynempfängern durchgeführt. Die sonst rauscharmen Direktdetektoren sind hierfür im Nachteil, da die vorgelagerten Spektrometer unrealistische Dimensionen annehmen müssten, um die erforderliche spektrale Auflösung zu liefern ($\sim 10^7$, siehe Kap. 1).

In einem Heterodynempfänger wird das Signal der astronomischen Quelle ω_s mit einer vergleichsweise starken monochromatischen Quelle (Lokaloszillator, LO) ω_{lo} gemischt um die Zwischenfrequenz (ZF) $\omega_{zf} = |\omega_s - \omega_{lo}| \ll \omega_s$ zu erzeugen. Daher ist das benötigte relative Auflösungsvermögen des nachgelagerten Spektrometer nun viel kleiner um das gleiche absolute Auflösungsvermögen zu erreichen. Ein wesentlicher Bestandteil jedes Heterodynempfängers ist der Mischer, ein elektronisches Bauteil mit einer nichtlinearen Kennlinie, der das Eingangssignal in die ZF (∼1–10 GHz) transformiert. Da der Mischer das erste aktive Bauelement im Empfänger ist, sind seine Empfindlichkeit und Rauschen für das Gesamtrauschen vom Empfänger besonders bestimmend (siehe Kap. 1).

Beste Mischerempfindlichkeiten werden derzeit mit Supraleiter-Isolator-Supraleiter (SIS) Tunnelkontakte erzielt, aber ihre höchst erreichbare Frequenz wird durch die materialintrinsische Energielücke der verwendeten Supraleiter begrenzt. Oberhalb 1 THz sind supraleitende phononen-gekühlte Hot-Electron-Bolometer (HEB) heutzutage die bevorzugten Mischer für Heterodynempfänger. Supraleitende phononengekühlte HEBs bestehen aus einer ultradünnen (<5 nm) supraleitenden NbTiN (oder NbN) Schicht zwischen zwei normalleitenden Elektroden (Wärmesenken) und sind eingebettet in einer THz-Hochfrequenzschaltung. Das HEB wird bei 4.2 K betrieben. Die RF Leistung wird in den supraleitenden Film eingekoppelt. Die dissipierte Energie im Film heizt ihn zu seiner kritischen Temperatur (∼ 8–9 K) auf, wodurch eine kleine Veränderung der absorbierten RF-Leistung in eine großen Veränderung des Widerstandes übersetzt wird. Die Widerstandsänderung wird durch den Biasstrom in eine Spannungsänderung umgewandelt. Da die dissipierte Leistung proportional zum Quadrat der Summe der Signalintensitäten ist,

wird die Spannung über dem HEB bei der Zwischenfrequenz des Empfängers moduliert, die durch das folgende Spektrometer analysiert werden kann.

Die Effektivität der Kühlung der dissipierten Leistung bestimmt dabei die Reaktionszeit des Bolometers, innerhalb der es auf Änderungen der eingestrahlten Leistung reagieren kann und bestimmt daher die ZF-Bandbreite. Die Kühlung erfolgt hauptsächlich über phononentransport in das Substratgitter (phononengekühlte HEB). Die ZF-Bandbreite kann erhöht werden, indem die supraleitende NbTiN oder NbN Bolometerschicht möglichst dünn (<5 nm) hergestellt wird. Um spektrale Linien mit großer Doppler-Breite werden ZF-Bandbreiten von mehreren GHz benötigt. Dies entpricht eine HEB-Reaktionszeit von wenigen zehn Pikosekunden.

Die weltweit wenigen Gruppen, die HEB-basierten Empfänger entwickeln, haben sich auf quasioptische Mischer (Substrat-Linse) konzentriert. Einerseits ist die Handhabung einfacher weil die Substrate dick bleiben dürfen. Andererseits ist die Kopplungseffizienz von einem guten Horn zu einem Gaußschen Strahl häufig überlegen. Die Mischer, die im Rahmen dieser Arbeit hergestellt worden sind, basieren auf Wellenleitern. Die Herstellung von THz-Hohlleitern ist wegen der kleinen Maße eine technische Herausforderung. Um RF-Verluste durch die Wellenleitermoden im Substrat zu vermeiden, darf ein Quarzsubstrat bei 1.9 THz maximal 10 μm dick sein.

Beträchtlich dünnere Substrate sind in Rahmen dieser Arbeit verwirklicht worden, indem die Mischer auf einer dünnen (d.h. 2 μm) Membran fabriziert wurden, welche auf einem Siliziumwafer aufgebracht war. Die Membran wird nach Herstellung der Mischer durch Wegätzens des Siliziums freigesetzt. Ein großer stützender Siliziumrahmen um die Membran wird benötigt, um die Handhabung und Kontaktierung zu erleichtern. Dieser Rahmen kann beispielsweise zusammen mit dem HEB auf dem gleichen Wafer hergestellt werden. Im hier vorgestellten Prozeß werden die Membran-HEB Mischer und die Siliziumrahmen auf getrennten Wafern hergestellt. Die sich ergebende Flächenersparnis auf dem Mischerwafer erlaubt die gleichzeitige Herstellung von 690 Mischer auf einem einzelnen 30 mm $\times$ 30 mm Wafer. Dies ist günstig wenn viele Mischer für einen Array benötigt werden, oder wenn die Herstellungs-Ausfallquote hoch ist. Es erlaubt außerdem viele verschiedene Parametervariationen auf einem Wafer zu testen. Dafür ist der Einbau in den Mischerblock etwas komplizierter, welcher zum ersten Mal für 1.4 und 1.9 THz hier demonstriert worden ist.

Die Herstellung der phononengekühlten HEBs wurde vollständig im institutseigenen Reinraum realisiert. Eine der technologischen Highlights war die Sputter-Ablagerung von ultradünnen NbTiN-Filmen mit hohen kritischen

Temperaturen (8.5 K), die bereits in [1] beschrieben worden sind. Der Schwerpunkt der hier vorliegenden Arbeit lag bei der Optimierung der Kontakte zwischen den Elektroden und der ultradünnen supraleitenden Schicht. Wenn die Kontaktfläche vor der Ablagerung der Elektroden geätzt wird, sind die Mischereigenschaften besser reproduzierbar. Die Wirkung der unterschiedlichen Ätzparameter auf die HEBs wurde untersucht. Um die eventuell geschädigten supraleitenden Filmeigenschaften wiederherzustellen, wird eine zusätzliche 20 nm NbTiN Schicht auf die Kontaktfläche gesputtert. Diese Schicht hat eine positive Wirkung auf das Mischverhalten aber brachte gewisse Schwierigkeiten im Fabrikationsprozess mit sich.

Die hergestellten Hohlleiter HEB-Mischer auf Siliziumnitridmembranen für GREAT auf SOFIA und CONDOR auf APEX sind in Rahmen dieser Arbeit bei LO-Frequenzen von 1.4 THz und von 1.9 THz mit einer im internationalen Vergleich guten Empfindlichkeit und sehr guter Stabilität demonstriert worden (Allan-Stabilitätszeit über 30 s). Die Rauschtemperatur zeigt einem flachen Verlauf über die gemessene ZF-Bandbreite (1.2–1.75 GHz). Der 1.4 THz Mischer ist bereits am APEX Teleskop für astronomische Messungen verwendet worden.

Contents

Chapter 1

Introduction

This work is mainly dedicated to the fabrication and testing of superconducting phonon-cooled hot electron bolometer heterodyne mixers. Nevertheless, this was not the end in itself but was embedded in an astrophysical project, which should be therefore outlined here.

1.1 Astrophysics at the THz Gap

Progress in astrophysics and astronomy has always been related to the technology needed to make astronomical observations. This is especially true for the THz region, as it still remains one of the least explored parts of the electromagnetic spectrum (and is therefore called the THz *gap*). This is partly due to the opacity of the atmosphere and partly to the technological constrains in this region of the electromagnetic spectrum. The THz gap is the region of the electromagnetic spectrum covering the frequency range between 300–30 μm (1–10 THz), located between the traditional RF microwave and the far-IR domains (see fig. 1.1).

In this regime the electromagnetic wavelength is on the order of magnitude

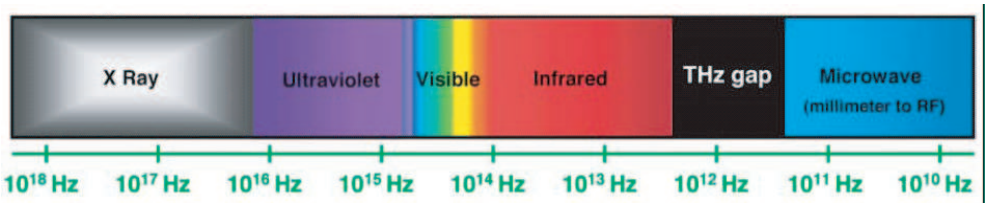

Fig. 1.1: *Representation of the electromagnetic spectrum illustrating the position of the THz gap [2].*

of conventional electronic component size (2 THz $\sim$ 150 μm), which was a fundamental science and engineering problem up to recent years [2].

The THz region of the electromagnetic spectrum allows astronomers to observe the cold universe. Detailed information of the observed astronomical objects such as velocity and pressure distribution can only obtained with high resolution spectroscopy.

The mixers produced in this thesis have been designed for heterodyne detection at 1.4 and 1.9 THz. In this short introduction I will only mention the most important lines which are intended to be observed with these mixers.

In the interstellar medium (ISM), one of the most important cooling lines for the understanding of their energy balance is the fine structure transition of atomic carbon **C^+ at** 158 μm ($\approx$ **1.9 THz**). It is the brightest line in the Milky Way submillimeter-wave spectrum and provides a detailed look at star forming regions where surrounding dust and gas is illuminated by hot young ultraviolet emitting stars. THz radiation generated behind dust clouds can be still detected from the earth, unlike optical light.

Spectroscopically resolved high rotational transitions of **CO** (at **1267 GHz, 1382 GHz and 1496 GHz**) reveal physical and kinematic conditions deep inside high mass star forming regions too.

H_2D^+ is a key ion in the formation of deuterated molecules as well as the last kinematic tracer to freeze out in cold molecular clouds. The ground transition of H_2D^+ is at **1370 GHz**.

The **N^+** transition at **1461 GHz** is the third strongest line detected in our Galaxy. It traces the warm ionized medium, which is thought to be ionized by supernovae explosions. N^+ is particularly prominent in starburst galaxies [3].

Since the THz radiation is strongly absorbed by atmospheric water vapor, Earth-based observations are strongly handicapped. Few high and dry sites offer some visibility up to 1.5 THz. For higher frequencies, airborne, balloon or space telescopes are required. The devices produced during this work have been tested at the KOSMA 3 m submillimeter telescope on the Gornergrat near Zermatt (Switzerland) at 0.8 THz and in the Atacama Pathfinder EXperiment (APEX) [1] at 1.4 THz. A further device will fly on board of SOFIA (Stratospheric Observatory for Infrared Astronomy), which is an airborne telescope in the last phase of its completion, operating at 1.9 THz.

[1] A 12 m telescope currently established at Llano de Chajnantor in Chile's Atacama desert.

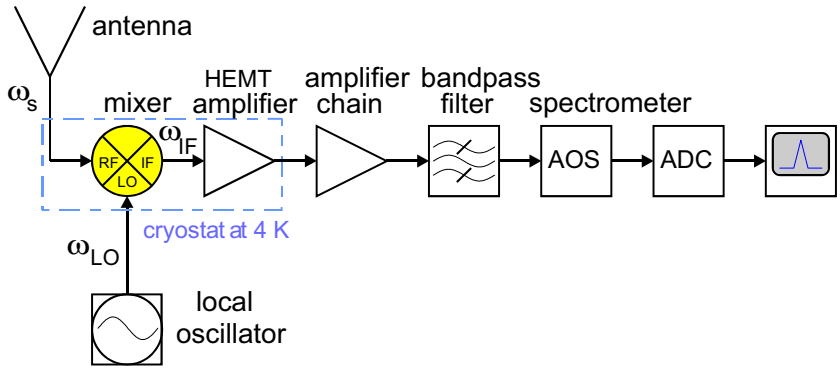

Fig. 1.2: *Basic components of a heterodyne receiver: The signal (ω_s) is superposed with a local oscillator signal (ω_{LO}) and feeded into a frequency mixer. The resulting intermediate frequency (ω_{IF}) is further amplified and analyzed by a spectrometer.*

1.2 Direct vs. coherent detection

The mixers fabricated in this thesis are used in heterodyne receivers.

In a heterodyne receiver system the signal is downconverted into the microwave band where it is spectrally analyzed (see fig. 1.2). The radio frequency (RF) signal is picked up by an antenna or waveguide probe at the frequency ω_s and the many magnitudes stronger and at a slightly offset-frequency monochromatic output of a "local" oscillator (LO) at frequency ω_{LO} are combined in the *mixer*, which is a nonlinear device generating the difference frequency $\omega_{IF} = |\omega_{LO} - \omega s|$, also known as the intermediate frequency (IF). For radioastronomical spectroscopy, the IF signal is processed by a multichannel spectrometer, such as an acoustooptical spectrometer (AOS) [4]. The IF signal is a replica of the original RF signal containing full phase and amplitude information and very high spectral resolution is possible. The basic reason that coherent detection is capable of very high spectral resolution, easily in excess of 10^6, is that the spectroscopy is actually done after downconversion by the "backend", at radio or microwave frequencies, using amplified signals and requiring substantially lower relative resolution ($\eta = \nu/\Delta\nu$).

The preserved phase information of a coherent detector provides a fundamental limit of its sensitivity. This can be explained by using the Heisenberg uncertainty relation $\Delta E \Delta t \geq h/2\pi$ in a semiclassical way. For n photons with the phase ϕ, the uncertainty relation is

$$\Delta n \Delta \phi > \frac{1}{2}$$

$\Delta\phi \leq 1/2$ is necessary for a phase coherence, therefore Δn must be at least 1 to satisfy the uncertainty relation. This introduces a limitation of the sensitivity in a coherent receiver which is known as the quantum limit. The minimum output noise power of a coherent receiver is $h\nu$ per unit bandwidth [5] or as an equivalent noise temperature

$$T_{quantum} = h\nu/k \sim 5 \text{ K} \cdot \nu 100 \text{ GHz}.$$

Fig. 1.2 shows that a heterodyne receiver consists of a mixer, amplifiers, bandpass filter and spectrometer. The sensitivity of the total system beyond the quantum limit is limited by the noise each component adds to the signal. The noise contribution of every individual component (i) is usually expressed by its noise temperature T_i which is defined as the equivalent noise input power divided by $k_B\Delta\nu$ (with bandwidth $\Delta\nu$). The total noise temperature of the receiver then is given by the generalized expression

$$T_{rec} = T_1 + \frac{T_2}{G_1} + \frac{T_3}{G_1 G_2} + \frac{T_4}{G_1 G_2 G_3} + \cdots, \tag{1.1}$$

where G_i is the gain (transmission) of the i-component. T_1 is the noise temperature and G_1 the gain of the first component. The equation can be simplified to

$$T_{rec} = T_{opt} + \frac{T_m}{G_{opt}} + \frac{T_{IF}}{G_{opt} G_m}, \tag{1.2}$$

where T_{opt} is the noise temperature generated from the optics, T_m is the mixer noise temperature, G_{opt} is the gain of the optics, G_m the mixer gain and T_{IF} the summarized noise temperature of the remaining components. Because usually the optics and the mixer have a gain $G < 1$ it is clearly evident that the noise and gain contribution of the optics and the mixer is crucial for receiver performance. Calculation of the total system sensitivity of the telescope needs therefore to include the contributions of the optical components and, in case of a groundbased (and to a lesser extent airborne) observatory, the atmospheric transmission. Particularly at submillimeter wavelengths, atmospheric transmission, optics directivity and transmission as well as the alignment accuracy of the quasi-optical components become the dominant contributions to noise temperature with decreasing wavelength.

The minimum detectable signal temperature ΔT^A_{min} is commonly defined as the signal at receiver input ΔT^A_{min} which exceeds by a factor of two the peak-to-peak noise voltage value produced by antenna and receiver at receiver output.

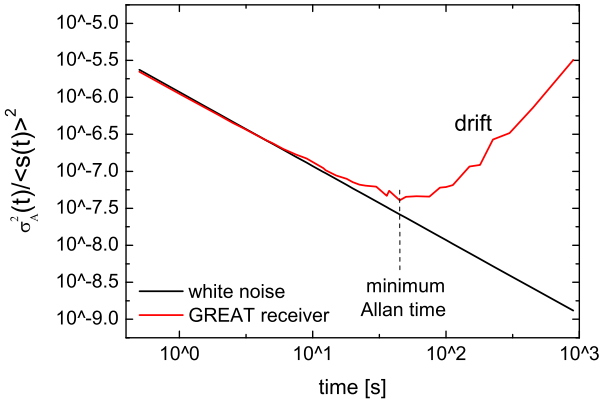

Fig. 1.3: *Normalized spectroscopic Allan variance at 1.9 THz for the GREAT receiver using a NbTiN membrane HEB mixer. $\delta\nu = 50$ MHz. The variance decreases following the radiometer equation for white noise. The increase in the variance with time is due to the drift noise. The crossover from white noise to drift noise is known as the Allan stability time or Allan minimum time*

For uncorrelated white receiver noise the value of ΔT^A_{min} can be calculated using the radiometer equation

$$\Delta T^A_{min} = \frac{T_{rec}}{\sqrt{\Delta\nu\,\tau}}\,. \tag{1.3}$$

Here $\Delta\nu$ is the detection bandwidth (fluctuation bandwidth at the resolution desired for the observation) and τ the integration time of the measurement. A detailed deduction of 1.3 can be seen for instance in [6] or [7].

The noise of any receiver can be seen as a combination of two terms: white noise and drift. There is a maximum integration time, known as the minimum Allan time τ_A, beyond which the signal/noise ratio drops slower than the white noise, or even increases (see fig. 1.3). Through beam switching (i. e. on-off) the drift noise can be outscored if the switch cycle time is smaller than τ_A. When the observed source is spatially extended, the fast chopping of the secondary mirror is often not sufficient to switch between on-off. Therefore, the telescope main dish needs to be moved[2] and the mechanical constrains require the Allan time to be $\sim$ 10 s or more. The HEB mixers produced in this thesis fulfil this requirement in excess ($\tau_A \sim$ 30–50 s), as it will be shown in chapter 6.

In the centimeter and millimeter bands, low-noise preamplifiers are used prior to downconversion and the mixers usually do not need to be low-noise.

[2] A detailed comment on observation methods is not given in this work.

Unfortunately there are no low-noise amplifiers for submillimeter signals. Therefore low-noise superconducting mixers are used as the first active component. Nowadays Superconductor-Isolator-Superconductor tunnel junctions (SIS) mixers are used in heterodyne receivers at frequencies below 1–1.2 THz. For higher frequencies, superconducting Hot Electron Bolometer (HEB) mixers are in use. In this work the HEBs developed at KOSMA for 1.4 and 1.9 THz are presented.

As already mentioned above, heterodyne receivers downconvert the THz signal preserving information about both the amplitude and phase. This results in the fundamental quantum limit for the sensitivity of coherent detection. Direct detectors register the amount of incoming photons without preserving phase information. Therefore direct detectors have in principle a sensitivity advantage (if high resolution spectroscopy is not required, see below).

The fundamental limits of direct detectors originate in the fluctuation of photon flux (shot noise $\sim\sqrt{n}$, Poisson distribution). If the largest source of shot noise arises at the dark current fluctuations of the detector the sensitivity is said to be detector limited. Background limited detection is the case when the thermal radiation of the environment (i. e. telescope dish) makes the largest noise source. The sensitivity η is expressed in Noise Equivalent Power (NEP). Best results are achieved with superconducting devices (NEP $\approx 10^{-19}$ W/$\sqrt{\text{Hz}}$, see for instance [8, 9, 10]). To obtain spectral information using direct detectors a photon energy selection has to occur before the photon arrives to the detector. Spectrometers are used for high spectral resolution and sensitivity as for instance a Fabry Pérot Spectrometer (FPS). FPS have a small available solid angle with high finesse. For multipixel arrays with a large detection area gratings are used to disperse the light onto an array of detectors. Each pixel receives the light from the grating corresponding to a different wavelength channel[3].

The main physical constrain with spectrometers is that their size grows proportional to the spectral resolution. For a resolution $R=\lambda/\Delta\lambda$, the linear size must be of order $R\lambda$. As an example, a grating spectrometer achieving $R=10^6$ at $\lambda=200$ μm ($\nu\approx 1.5$ THz) would require a 200 m grating! Additionally, to avoid thermal background noise the grating must be kept cold, $kT\ll h\nu$.

There is a crossover between the spectral resolution of direct detectors which is technologically limited and the sensitivity of the coherent detectors which is quantum limited. High spectral resolution $\sim 10^7$ in the THz region

[3] See for example the photodetector array PACS [11]).

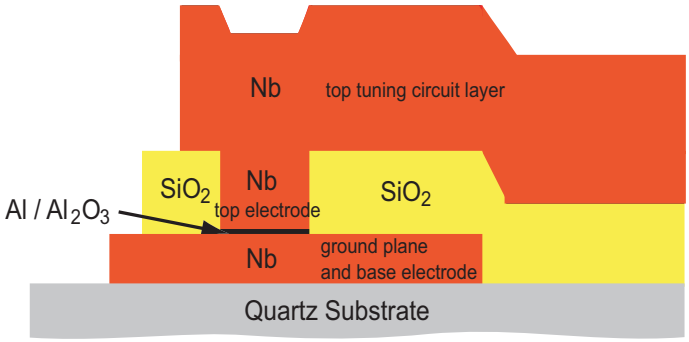

Fig. 1.4: *Schematic cross section of a Superconductor-Insulator-Superconductor (SIS) device (taken from [12]) with standard Nb-Insulator-Nb trilayer including the integrated tuning circuit (top wiring and ground plane)*

is done with heterodyne receivers.

1.3 Superconducting Mixer Devices

SIS tunnel junctions (see fig. 1.4) are nowadays the standard mixing devices for radio frequencies up to ≈1 THz. Receivers using SIS mixers have very low noise temperatures (just a few times the quantum limit) and the SIS mixers require low LO-power, which is important at these frequencies. SIS mixers are fabricated with thin films and microfabrication methods as used in the semiconductor industry are required. Typical thicknesses are 100–150 nm for the junction electrodes and only 1–2 nm for the tunnel barrier. An extraordinary nonlinearity is created by the gap in available energies for quasiparticles on both sides of an SIS tunnel barrier. In an ideal SIS junction at absolute zero no dc current can flow below the threshold voltage $V_g = 2\Delta/e$, while above V_g the dc current is near the normal state value. This perfectly sharp nonlinearity is smeared over some range δV_g in real SIS junctions operating at liquid helium temperature. A SIS mixer consists of such a junction embedded in a coupling structure. The mixer behaves classically if radiation with quantum energy $h\nu/e$ smaller than δV_g is applied. At millimeter wavelengths, the quantum energy $h\nu/e$ may be larger than the voltage width δV_g for onset of quasiparticle tunneling in a SIS junction [13]. Contrary to classical mixers, quantum mixers (such as SIS) exhibit conversion gain, radiation-induced negative resistance and sensitivity limited only by irreducible quantum noise [14].

Quasiparticle mixing is limited by the combined double energy gaps

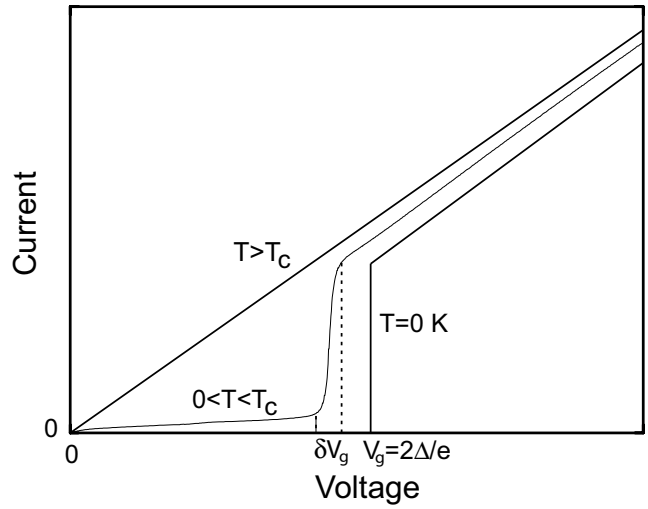

Fig. 1.5: *SIS current voltage characteristic without applied RF power: The tunnel current between the superconducting electrodes at $T = 0$ K is compared with the tunneling between the same materials in the normal state at $T > T_c$ (modified from [12]). The measured I-V curve at $T = 4.2$ K shows the non vanishing subgap current, a slightly reduced gap and a smeared nonlinearity over δV_g.*

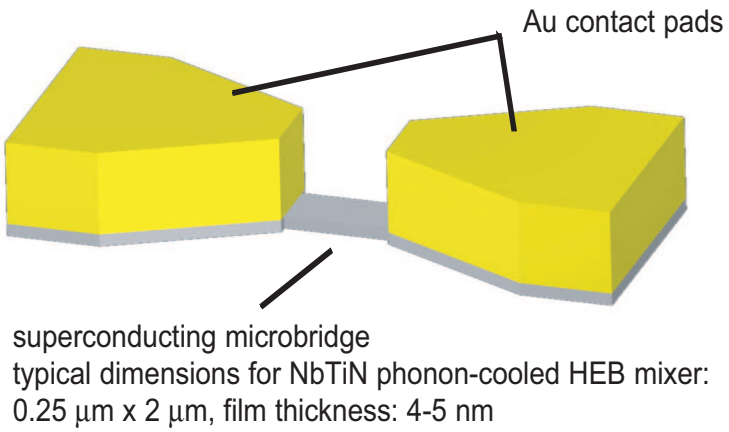

Fig. 1.6: *Schematic representation of a HEB device.*

$2\Delta_1 + 2\Delta_2$ of the SIS junction electrodes which, for a standard niobium SIS junction, is theoretically 1.4 THz ($4\Delta/h$), but practically limits operation to about 1.2 THz [15]. Theoretically, SIS junctions made of Nb-Al/AlN-NbTiN should have a mixing limit frequency of 1.9 THz [16]. The highest operation frequency of a SIS mixer reported is 1.2 THz using a Nb-Al/AlN-NbTiN SIS junction and with an uncorrected receiver noise temperature of 550 K [17].

For higher frequencies, superconducting Hot Electron Bolometer (HEB) mixers are nowadays the devices of choice. Although their noise temperatures are still higher than those of SIS devices, they do not have a threshold frequency and can operate well over 1.2 THz. Heterodyne measurements with HEBs have been reported at frequencies as high as 5.3 THz with a receiver noise temperature of 8800 K [18]. HEB mixers are made of very thin (≤ 10 nm) and small ($< 1 \times 1$ μm^2) superconducting microbridges and thus also require microfabrication (see fig. 1.6). Unlike SIS tunnel elements, HEB devices do not generate the IF signal through photon assisted tunneling, but are ultra-fast thermal detectors (chapter 2). HEBs fall into the category of power detectors or square-law detectors. When two signals $V_{LO}(t)$ and $V_s(t)$ at slightly different frequencies ω_{LO} and ω_s are injected into the mixer, the

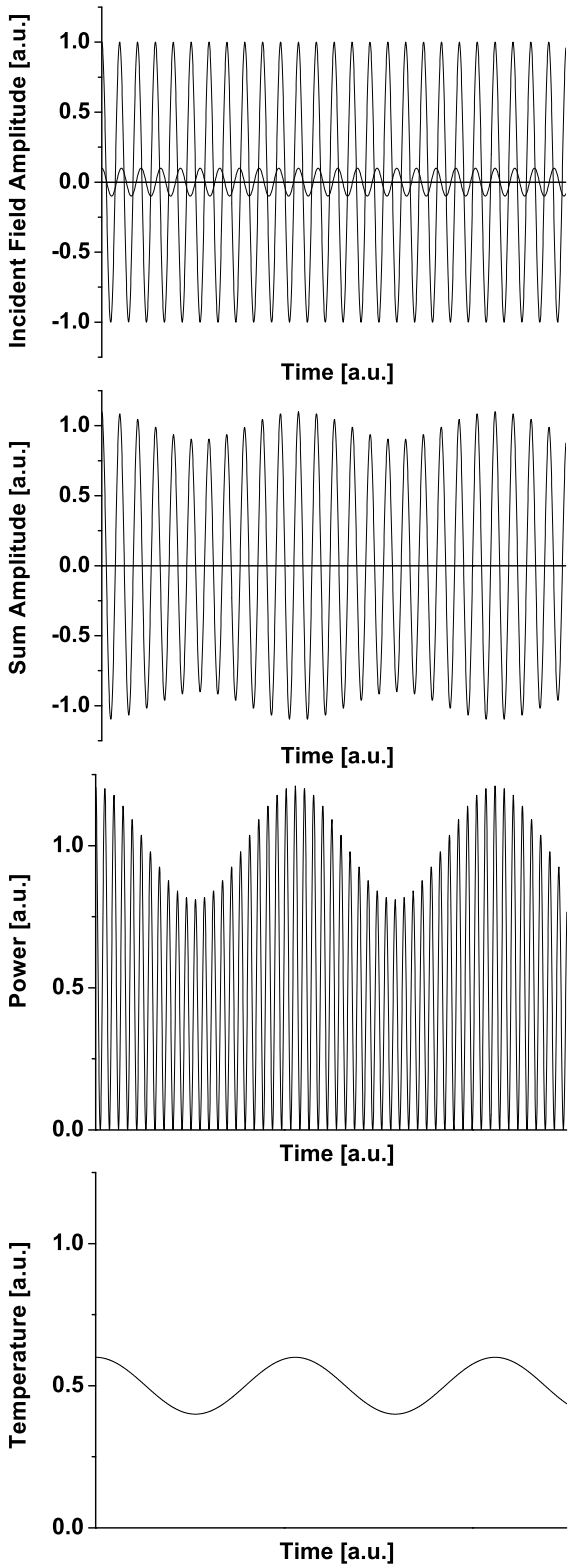

Fig. 1.7: *Visualization of the square-law aspect of the HEB mixing process. The electron temperature can only follow the intermediate frequency. The parameters used to generate this plot are:* $\omega_{IF} = 0.1\omega_s$, $E_s = 0.1E_{LO}$

power is calculated as:

$$\begin{aligned} P(t) &= \frac{1}{R}\left[|V_{LO}|\cos(\omega_{LO}t)+|V_s|\cos(\omega_s t)\right]^2 \qquad (1.4)\\ &= P_{LO}+P_s+P_{LO}\cos(2\omega_{LO}t)+P_s\cos(2\omega_s t)\\ &+ 2\sqrt{P_{LO}P_s}\cos\left[(\omega_{LO}+\omega_s)t\right]\\ &+ 2\sqrt{P_{LO}P_s}\cos[(\omega_{LO}-\omega_s)t]\,, \qquad (1.5) \end{aligned}$$

with $P_{LO}=|V_{LO}|^2/R$ and $P_s=|V_s|^2/R$.

Calculation of expression 1.4 delivers time-oscillating terms at frequencies $2\omega_{LO}$, $2\omega_s$, $\omega_{LO}-\omega_s$ and $\omega_{LO}+\omega_s$. The HEB is not able to react to the fast oscillations of the RF signals. Yet, since the RF-frequencies ω_{LO} and ω_s are chosen to be only slightly different, the temperature of the HEB can actually oscillate at the beating frequency $\omega_{LO}-\omega_s$, which is usually in the 1–10 GHz range (Equation 1.5). Due to the resistance dependence on temperature of the superconducting microbridge material, the modulation of the temperature generates a (generally strong) oscillation of device resistance [19][20][21]. Apparently, there is no intrinsic limitation for the mixing frequencies as long as the photons are able to dissipate their energy in the microbridge.

The main focus of this work is the development of HEB mixing devices for the CONDOR receiver at 1.4 THz and GREAT at 1.9 THz. A main challenge was to reduce the noise temperature of the mixers. A central decision aiming this goal was to manufacture the mixers for a waveguide environment.

1.3.1 Waveguide and Quasi-optic Arrangements

As stated in 1.2, minimizing losses in the first stages of an astronomical receiver is of utmost importance. Losses due to the atmosphere can only be decreased by observing from high altitudes (earth-, aircraft- or spacecraft-based). The next crucial step is the coupling of the free-space electromagnetic waves into the mixer prior to heterodyne mixing.

The input frequencies of the mixers presented in this thesis are $\nu \sim$ 1–2 THz ($\lambda \approx$300–150 μm) and the coupling circuit (such as a planar antenna or a waveguide probe) is of the order of magnitude of the wavelength. Generally, it is integrated with the HEB on the mixer chip. The coupling of the beam can be generally realized in two ways:

- Quasi-optical lens + planar antenna.
- Waveguide cavity + waveguide probe.

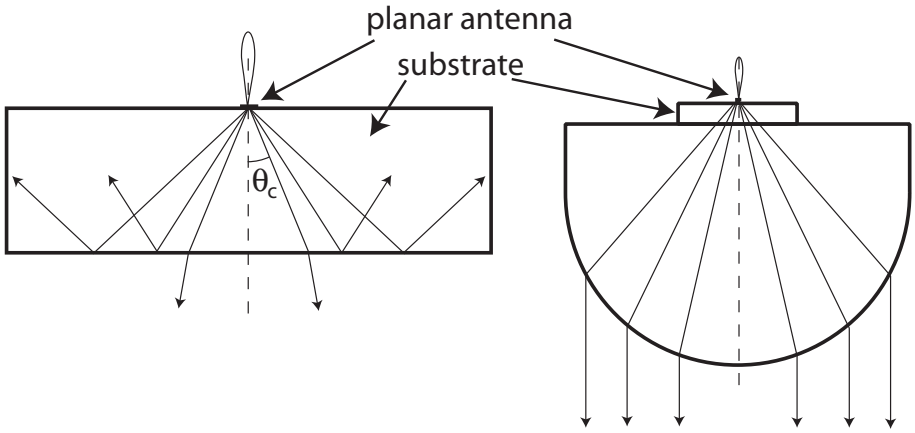

Fig. 1.8: *Left: Planar antenna on a dielectric substrate. All the power radiated above the critical angle θ_c is trapped in the substrate and coupled to substrate modes. Right: A hyperhemispherical lens consists of a hemisphere which is extended by a cylindric section. The lens synthesizes a dielectric half space and virtually solves the problem shown on the left. A small portion of the radiation power can also be coupled from the front side, as symbolized by the small parasitic lobe.*

In the first case a physically small planar antenna (with a small effective aperture to collect the incoming radiation) is integrated with the HEB on the chip. The radiation power must be collimated and coupled into the antenna. Just placing the planar antenna at the focal plane of a collimating reflector or lens is not effective, since the radiation power couples much better into the dielectric substrate than into the antenna[4]. Besides, a large part of the radiation is reflected at the substrate-air interface (see fig. 1.8 on the left). To prevent this, the substrate is expanded with a semi-infinite dielectric substrate. The infinite dielectric is created using a lens of a material with the same dielectric constant attached to the backside of the antenna substrate (see also fig. 1.8 right). The substrate lens is usually hemispherical, hyperhemispherical, elliptical or extended hemispherical [22].

In the second case a waveguide probe is integrated with the HEB and a horn antenna is used to couple the free space signal into the waveguide (see. fig. 1.9). It accepts a matched beam shape and matches the waveguide impedance to the impedance of the free space wave. The waveguide consists of a closed rectangular channel with conducting inner walls. If the channel width is half the wavelength of the signal and the height is matched,

[4] $\frac{P}{P_r} \sim \frac{1}{\varepsilon_r}$, being P the radiation power coupled into the antenna, P_r the radiation power coupled into the dielectric substrate and ε_r the dielectric constant of the substrate.

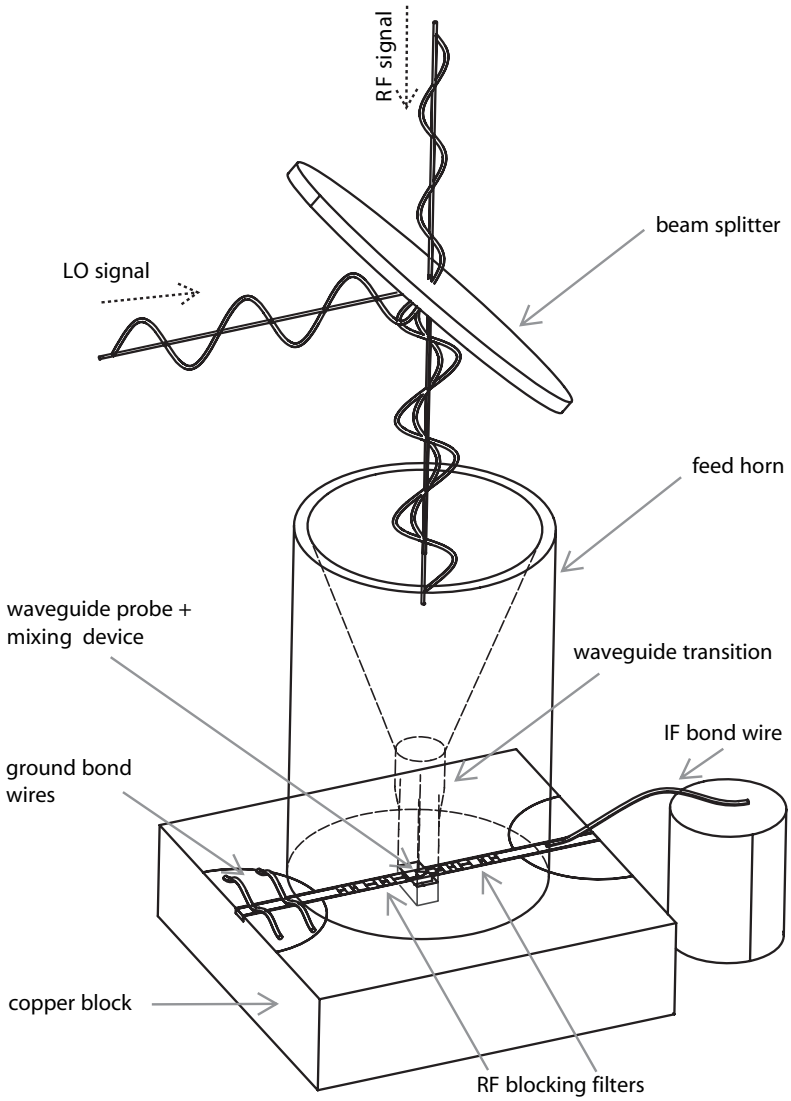

Fig. 1.9: *Graphic representation of a waveguide mixer. The RF-signal (e. g. from a telescope and LO-signal are overlapped using a beam splitter (see chapter 6) and coupled into the waveguide by the feed horn. The waveguide probe couples the signal into a microstrip mode which is absorbed and frequency- downconverted by the mixing device. The RF blocking filters are microstrip structures which reflect the THz-frequency signals back to the mixing device to avoid losses. Illustration from [23]*

.

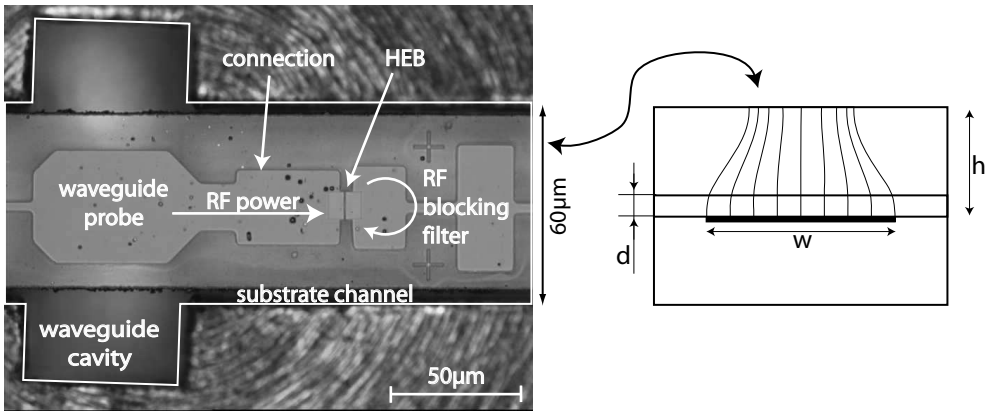

Fig. 1.10: *Left: Microscope picture of a 1.9 THz waveguide cavity and substrate channel carrying a silicon nitride membrane with an HEB mixer and integrated waveguide circuit. Right: Schematic cross-section view into the substrate channel with the freestanding silicon nitride membrane strip and the microstrip beneath it. The thin lines represent an approximation of the E-fied lines of the undesired quasi-TEM mode. For the calculation of the cutoff-frequency the membrane strip is assumed to be as wide as the substrate channel.*

signal transport with very low dispersion and losses is possible (fundamental waveguide mode). The maximum (cutoff) wavelength λ_c of a wave which can propagate in a waveguide of maximal side dimension a is:

$$\lambda_c = 2a\,. \tag{1.6}$$

In our case the signal is transported to a waveguide probe, which is suspended in the waveguide and couples the waveguide modes into microstrip modes. For perfect coupling the impedances of the probe and of the waveguide must be matched. This is accomplished through a backshort at appropriate depth underneath the probe. At the waveguide probe the signal is coupled into the guiding microstrip. It should be avoided that a part of the power is coupled into a quasi-TEM wave which propagates through the substrate channel [24]. The lowest order transverse resonance frequency ν_c for this mode (i. e. the lowest frequency for which quasi-TEM propagates) is given by

$$\nu_c = \frac{c}{\sqrt{\frac{d}{h}(\varepsilon_r - 1) + 1}} \frac{1}{2w + 0.8h}, \tag{1.7}$$

being d the substrate thickness, h the height of the microstrip over the substrate channel and the dielectric membrane, ε_r the dielectric constant of the

substrate and w the width of the microstrip (see fig. 1.10). The substrate mode is not symmetrical in the substrate channel, since the microstrip radiates more likely into the dielectric as into free space [22]. To avoid losses at 1.9 THz through the substrate channel a quartz substrate can have a maximum thickness of $\approx$ 10–15 μm ($\varepsilon_r \approx 4$). The thickness of the substrate can be maximized by reducing the width of the microstrip on the substrate. There is a limit to this reduction though, since first, a too narrow connection to the probe can couple less power from the waveguide probe to the HEB. Further, a too narrow microstrip in the substrate channel prevents an effective blocking of the RF after the HEB. Experience with fused quartz substrates at KOSMA has shown that the limit to which substrates with microstrip lines on one side can be polished down before they break is $\sim$ 30–40 μm [25].

In this thesis the fused quartz substrate has been substituted by 2-μm silicon nitride (Si_3N_4) membrane strips ($\varepsilon_r \approx 4$ at 1 GHz, depends on deposition conditions [26]). This practically eliminates the substrate mode propagation far beyond 1.9 THz even for wide microstrips (up to 40 μm). The assembly of the membrane in the waveguide is in comparison to "thick" substrates more elaborate and requires special techniques which are explained in chapter 5. Decreasing the substrate thickness by an order of magnitude opens up the possibility of using waveguides up to very large frequencies (provided these are etched in silicon).

Waveguide mixers at THz frequencies demand considerably more technical effort than quasi-optical mixers. The waveguide cavity dimensions have to be reduced in order to fulfill equation (1.6). Besides, since the skin depth gets smaller for shorter wavelengths the surface roughness of the waveguide walls become important. The tolerances of the waveguide together with the reduced substrate thickness make waveguide arrangements for THz frequencies very difficult to manufacture.

Despite manufacturing difficulties, waveguide mixers offer a set of advantages that make them to be the technology of choice for heterodyne mixers whenever it is possible to realize:

- Waveguide horns provide single mode structure and an extremely high gaussivity of the beam, enabling outstanding coupling to the telescope beam (98% instead of $\leq$ 95% for quasi-optic mounts).

- Waveguide mounts are easier to adjust to an existing telescope beam. In a quasi-optic mount the positioning of the planar antenna on the dielectric lens is difficult and critical. Non-centric placing or slightly

tilted substrate leads to dramatic changes in the radiation pattern of the antenna, which is then difficult to adjust to the telescope beam.

- Intrinsic blocking of frequencies below the cut-off frequency, avoiding saturation of the mixing device.
- Compact designs for array and satellite applications can be readily achieved with waveguide mounts.
- Waveguide probes need less space on the production wafer than open structure antennas and a larger number of devices can be produced in one batch.

1.4 Thesis' Overview

The aim of this thesis was to provide waveguide mixer devices for CONDOR operating at 1.4 THz and GREAT at 1.9 THz. The basic challenge was to manufacture low-noise HEB mixing devices on membranes with the waveguide technologies for frequencies beyond 1 THz. During this thesis, a new fabrication process for *phonon-cooled* HEB (see chapter 2) was established and an existing membrane concept [27] (see chapter 5) was successfully implemented for frequencies beyond 1 THz.

The manufacturing of the devices at the microfabrication laboratory is described in chapter 3. The DC-testing of the device batches (chapter 4) and the RF testing of selected devices (chapter 6) had a direct feedback on the fabrication process, which had to be continuously improved.

Results of the both HEB mixing devices at 1.4 THz and 1.9 THz are presented in chapter 6 too.

Chapter 2

Hot Electron Bolometer — Principles

2.1 Basic definition

A bolometer consists of a radiative heat absorber with the heat capacity C which transforms radiation into heat ΔW. The consequent change in temperature $\Delta T = \Delta W/C$ is then measured by an appropriate thermometer and is proportional to the amount of radiation. The absorber is in thermic contact (heat conductivity G) with a bath having the temperature T_b (see fig. 2.1). In analogy to the electrical circuit quantities, the characteristic response time $\tau = C/G$ can be interpreted as the time the bolometer needs to return to its original configuration after a radiation event has been registered.

A bolometer can operate as a heterodyne mixer since the temperature shift is proportional to the power absorbed and therefore to the square of the sum of the astronomical signal ω_s and the signal of the local oscillator ω_{LO}:

$$\delta T \propto \frac{V(t)^2}{R} \propto [V_{LO}\cos(\omega_{LO}t) + V_s\cos(\omega_s t)]^2 \quad (2.1)$$

$$\propto V_{LO}V_s\cos[(\omega_{LO} - \omega_s)t] + \mathcal{O}(\omega_{LO} + \omega_s) + \mathcal{O}(\mathrm{dc}). \quad (2.2)$$

Equation (2.2) shows that the temperature oscillates at the *Intermediate Frequency* (IF) $\omega_{LO} - \omega_s$ and much faster at the sum frequency $\omega_{LO} + \omega_s$. Under some circumstances, it is possible to measure the temperature oscillations at the IF. Hence, the bolometer can perform as a mixer. The maximum measurable IF must be lower than the relaxation rate of the bolometer $(\tau)^{-1}$. Otherwise the bolometer temperature will be unable to follow the IF (the sum frequency is in any case too high to be measured by these means). As a heterodyne mixer in the THz range, the bolometer should be able to follow

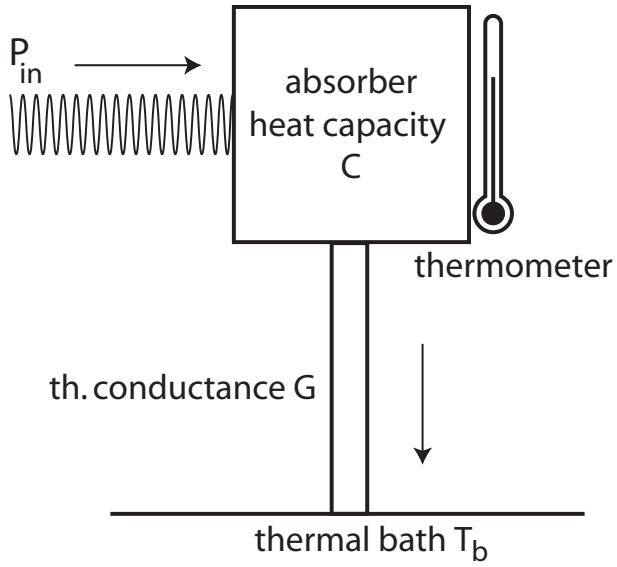

Fig. 2.1: *Schematic diagram of a bolometer. The arrows symbolize the energy flow.*

intermediate frequencies of at least 1 GHz. That corresponds to a maximum characteristic response time of $\tau = 1/\omega_{IF} \approx 0.16$ ns. To reach such short response times, the bolometer must have an extremely low heat capacity as well as an excellent coupling to the thermal reservoir.

2.2 Hot Electron Bolometer

In a *hot-electron* bolometer (HEB), the electrons act as the absorber and are heated by dc and rf power above the temperature of the lattice, which acts as the thermal bath. In this model, also called two-fluid model, the HEB is a system with two different subsystems which can interact with each other but are not in instantaneous thermal equilibrium. If the resistance of the electronic system depends on the electron temperature, then the resistance can be used as a thermometer. Since the electrons have a very low mass, and hence a very low heat capacity C, τ can reach very low values, even low enough to follow the IF.

There are two different ways of implementing a HEB, depending on the material which is used: Semiconductors or superconductors.

2.2.1 Semiconductor Hot-Electron-Bolometer

The first hot electron bolometers were based on lightly doped InSb. At cryogenic temperatures, the electrons get decoupled from the lattice and can be heated beyond the lattice temperature by radiation. The mobility of the electrons μ (and therefore the resistance) depends on temperature ($\mu \propto T_e^{3/2}$) [28].

Nowadays, semiconductor hot electron bolometers are no more in use as mixers for astronomy because their bandwidth is very limited. In InSb, the maximum intermediate frequency is constrained by the cooling mechanism of the electron-phonon inelastic interaction. For InSb, this interaction rate is $\approx (0.1\mu s)^{-1}$, which limits the intermediate frequency bandwidth to about 1 MHz. For THz-astronomy applications this is unacceptably low. Here, a bandwidth *of at least* 1–2 GHz is desired.

2.2.2 Superconducting Hot-Electron-Bolometer

A superconductor near T_c can be a very sensitive bolometer, since the resistance depends strongly on temperature. In dirty-limit[1] thin metal films at cryogenic temperatures the electron-electron interaction rate is much faster than the electron-phonon interaction rate. In this case dc and rf power can heat the electrons in a shorter timescale than the lattice, which can be regarded as the thermal bath of the electrons. Additionally, in dirty-limit metals, the electron momentum relaxation time is very short (<1 fs), so that power can be absorbed up to very high frequencies ($\sim$100 THz). It has been reported that dirty-limit Nb superconducting thin films absorb radiation uniformly from 10^{10} to 10^{15} Hz with approximately the same efficiency [29].

There are two main different theoretical models explaining how the resistance variations are achieved in a superconducting HEB:

Lumped-element model In this model the bridge dimensions are considered as small enough and eventual parameter variations over the bridge length are discarded (i. e. temperature variations). The HEB is regarded as one finite element (lumped-element). The resistance dependence of the HEB at the superconducting transition at T_c produces the voltage oscillations at the intermediate frequency (see fig. 2.2).

[1] Very thin films do not show the same properties of a bulk pure sample of the same material. This can be due to the influence of impurities and lattice defects which cannot be fully avoided when manufacturing such thin films. The influence of the substrate plays i. e. a major role.

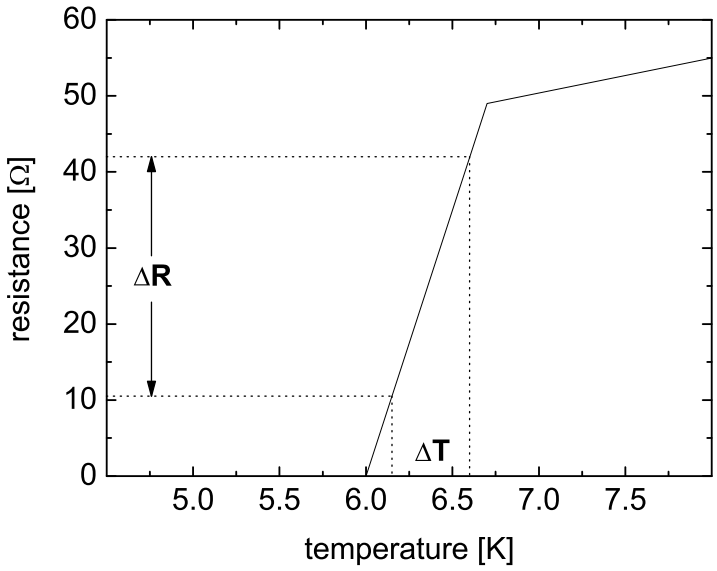

Fig. 2.2: *Simplified plot of the superconducting transition in the microbridge. A small temperature shift ΔT produces a measurable resistance change over the whole bridge length. In the lumped element model, this is the responsible mechanism for the IF modulation of the resistance.*

Distributed model In this approach a temperature distribution over the length of the microbridge is considered (see fig. 2.4). In the superconducting thin film an electronic normal conducting region (hotspot) is produced by the dissipated heat in the microbridge, while the rest of it remains superconducting. The modulation of the resistance at the intermediate frequency is created by the hotspot length oscillations. Different variations of this models are presented in this work. Using this approach excellent simulations of measured data could be demonstrated [30].

2.3 Lumped element model

Certain parameters such as temperature and heat conductivity are supposed to be the same over the whole volume of the HEB. In this model the bridge is considered to be brought to the superconducting transition by the dc-bias current as well as by the RF-power heat dissipation. At T_c the film shows a steep resistance dependence on temperature. A small periodic shift in the electron temperature at the IF will produce resistance oscillations. Under the

current bias, this leads to an alternating voltage at the IF. The calculations for the conversion efficiency and for the mixer noise in the following sections are based in approximations of the HEB as a lumped element [31].

2.3.1 Conversion efficiency

An important figure of merit for mixers is the conversion efficiency η, also called conversion *gain*, which is defined as the ratio of the available output power at the IF to the available input power at the RF. Obviously, a high conversion gain is desired in order to reduce the total receiver noise temperature (equation 1.2).

In order to get a quantitative approximation for the conversion efficiency η the power input and the energy transfer is set into the energy conservation law ($P_{in} = P_{out}$) delivering for η [31]:

$$\eta = \frac{4RR_L}{(R+R_L)^2}\frac{P_{LO}}{2R}\left(\frac{I_{dc}(dR/dT)}{G_{eff}}\right)^2\frac{1}{1+(\omega_{IF}\tau_{eff})^2}, \tag{2.3}$$

R being the instantaneous resistance of the microbridge, which depends on temperature and hence on time, R_L the load resistance at the IF (i. e. the input resistance of the IF amplifier) P_{LO} the power coupled from the local oscillator, I_{dc} the dc bias current, dR/dT the resistance dependence on the temperature (the slope of the superconducting transition at the operation point), and

$$G_{eff} \equiv G(1-\alpha), \tag{2.4}$$

$$\tau_{eff} \equiv \frac{\tau}{1-\alpha}, \tag{2.5}$$

$$\tau \equiv C/G, \tag{2.6}$$

$$\alpha \equiv \frac{I_{dc}^2 dR/dT}{G}\frac{R_L-R}{R_L+R}. \tag{2.7}$$

The first factor in (2.3) results from the impedance mismatch between the device output impedance and the input impedance of the IF amplifier. The parameter α varies between zero and one. It is zero for a perfect impedance matching. α is a quantitative measure of the so called *electro-thermal feedback*. In a material in which the resistance increases with temperature, heat dissipation results in increase of resistance and has therefore an influence on the dissipation too ($P = I^2R$ or V^2/R), which further affects the temperature and so forth.

Under a current bias a small increase in the resistance causes the dissipated dc power to increase, since $P_{dc} = I^2R$. A power increase causes an additional temperature rise. If the dR/dT is positive, as is the case for superconducting bolometers, increasing the temperature serves to further increase the resistance, and there is positive feedback. For $\alpha = 1$, there is a thermal runaway. The temperature will increase until the normal state is reached, in which $dR/dT \to 0$ and therefore also $\alpha \to 0$. If the dc power supply is a voltage bias, then it will serve to stabilize the system temperature, since $P_{dc} = V^2/R$, which will cause a decrease in the dissipation power when the temperature rises.

For a perfect matching between the device output impedance and the input impedance of the IF amplifier the electro-thermal feedback can be ignored ($\alpha = 0$), equation (2.3) simplifies to

$$\eta^\star = \frac{P_{LO}}{2R}\left(\frac{I_{dc}(dR/dT)}{G}\right)^2 \frac{1}{1+(\omega_{IF}\tau)^2}, \tag{2.8}$$

where $\eta^\star$ is the conversion gain when the impedances are matched ($\alpha = 0$). Since we will now only consider this special case, we will write in the following η instead of $\eta^\star$ to keep the notation simple.

From (2.8) follows that η falls by 3 dB at the intermediate frequency

$$\omega_{3dB} = \frac{1}{\tau},\ \nu_{3dB} = \frac{1}{2\pi\tau} = \frac{1}{2\pi}\frac{G}{C}. \tag{2.9}$$

The intermediate frequency ν_{3dB} is usually called rolloff-frequency and is defined as the IF at which the conversion gain drops by 3 dB. To calculate ν_{3B} considering the electrothermal-feedback τ must be substituted by τ_{eff}.

The theoretical calculation of η in the lumped element model confirms the intuitive assumption that a steep superconducting transition increases the conversion gain is confirmed. It is important to remark that an increase in the thermal conductivity G, which is necessary to increase the IF-bandwidth (2.9) also results on a reduction of the conversion gain.

2.3.2 Mixer noise

The mixer noise figure is the power per frequency at the rf input required to give a signal to noise of one at the output IF. In the Rayleigh-Jeans limit[2]

[2] In the THz range there are better approximations. More details on this issue will follow in chapter 6.

$(h\nu \ll k_b T)$

$$P = k_b B T \Rightarrow \frac{P}{B} = k_b T,$$

k_b being the Boltzmann constant and B the bandwidth. We can therefore express noise as the temperature a matched resistor would be at to radiate $k_B T$ power per frequency into the receiver.

The figure *mixer noise* regards not only the output noise power of the mixer but its contribution to the system's overall noise, which is given by:

$$T_{mix} \equiv \frac{T_{out}}{\eta}, \tag{2.10}$$

T_{out} being the mixer output noise and η its conversion efficiency.

The mixer output noise sums up from three different main sources (ordered with increasing weight in the total sum):

- Quantum noise
- Johnson noise
- Thermal fluctuation noise

The contribution of quantum noise (see chapter 1) and Johnson noise (generated by the electron temperature in any resistor) to the total mixer noise of a HEB is nowadays relatively small. The thermal fluctuation noise, arising from temperature fluctuations produced by the random energy exchange between the electrons and their environment, is by far the largest noise contribution for HEBs. Superconducting HEBs are designed to greatly amplify temperature fluctuations in resistance fluctuations and therefore thermal fluctuations are the largest noise source [32]. Other noise sources may be included when the mixing mechanisms of the superconducting HEBs are better understood (probably not using a lumped-element model). The mixer noise in the lumped element approximation can be expressed as:

$$\begin{aligned} T_{mix} &\equiv \frac{T_{out}}{\eta} \\ &= \frac{T_{th}}{\eta} + \frac{T_{Johns}}{\eta} \\ &= \frac{2T_e^2 G}{P_{LO}} + \frac{2RT_e G^2}{P_{LO} I_{dc}^2 (dR/dT_e)^2} \left(1 + (\omega_{IF}\tau)^2\right). \end{aligned} \tag{2.11}$$

The first term is due to the thermal fluctuation noise, while the second term is due to the Johnson noise. The first term is not dependent on the IF

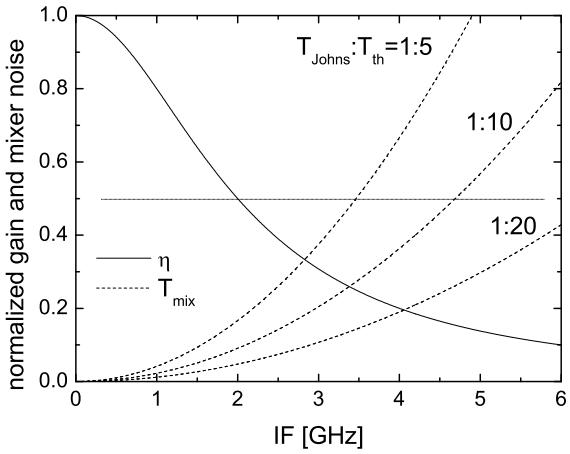

Fig. 2.3: *The conversion gain η has been plotted for $\nu_{3dB} = 2$ GHz using equation(2.8) in normalized units for increasing IF (continuous line). The mixer noise dependence on IF for a theoretical mixer with the same gain rolloff-frequency (broken lines) is plotted in normalized units for different quotients of the Johnson noise T_{Johns} and thermal fluctuation noise T_{th}. A typical relation is 1:10 [31, page 26] resulting in a noise rolloff-frequency of 4.7 GHz, 2.3 times more than the corresponding gain rolloff-frequency.*

because both T_{th} and η depend in the same way on ω_{IF}. The second term depends on the IF because the Johnson noise T_{Johns} is actually white, whereas the conversion efficiency η decreases as the IF increases (2.8).

Since T_{mix} and η show a different dependance on the IF, it is clear that the *gain* rolloff-frequency cannot be the same as the frequency needed to make the mixer noise rise by a factor of two, which is the definition of the noise bandwidth. The gain rolloff bandwidth is generally shorter than the noise rolloff bandwidth. This fact is illustrated on fig. 2.3 for different fractions of the Johnson noise T_{Johns} to the thermal fluctuation noise T_{th}. Using this theoretical framework, the relation T_{Johns}/T_{th} can be calculated if the gain and the noise IF rolloff-bandwidth are known:

$$\frac{T_{th}}{T_{Johns}} = \left(\frac{\nu_{rolloff-noise}}{\nu_{3dBgain}} \right)^2 - 1. \tag{2.12}$$

Since it is much easier to experimentally determine the noise temperature than the gain, most of the reported IF-bandwidths as well as in this thesis are *noise* IF bandwidths.

2.4 Hotspot model

The hotspot model is a distributed model to describe HEBs. This theory was originally proposed by [33, 34] and developed for HEBs by [35] by focusing on an electronic hot spot. In the new formulated concept for mixing the temperature oscillations modulate the length of a fully normal domain in the middle of the bolometer bridge.

In the lumped element model we have considered the superconducting transition to be responsible for the strong resistance variations which produce the voltage oscillations at the intermediate frequency. In that model the whole bridge was considered as one unit with uniform temperature. In the hotspot model, the bridge is basically divided in two different regions.The main distinction here is the presence of superconducting and normal conducting states along the bolometer bridge, which is mostly considered as having one-dimensional geometry. The division of the bolometer bridge in two phases can only be done provided that the superconducting coherence length ξ is much shorter than the bridge dimensions, which is the case for NbTiN ($\sim$5 nm) or NbN ($\sim$3 nm). The center of the microbridge is normalconducting because its temperature has already exceeded the critical value ($T > T_c$). The extremities of the bridge, which are in good thermal contact with the heat sinks (at the bath temperature T_b) are assumed to be superconducting[3] ($T_e < T_c$). The resistance oscillations are brought about by the variations in length of the normal conducting region in the middle (*hotspot*), produced by the dissipated power oscillations at the IF. Optimal operation can be achieved when the hotspot length can vary over a maximal range.

The central tool to calculate figures as the conversion gain or to predict the current to voltage dependence of the HEB using the hotspot model are the heat-balance equations. The energy input to a bridge section is outweighed to the energy output.

The simplest simulations using the hotspot model make only a difference between superconducting and normalconducting regions. For each region a different heat balance equation is considered using the respective physical conditions for heat dissipation and heat conduction. The heat is produced through dc- and rf-dissipation ($j^2\rho + p_{rf}$) and is conducted to the next region by the temperature difference between them $[K(dT_e/dx)_x - K(dT_e/dx)_{x+\Delta x}]$ or by electron-phonon inelastic scattering at T_b. Inside and outside the hotspot

[3] In later models, though, the electron transparency to the heat sinks is known to be of the order of 5% and therefore a exponential decay of the electron temperature inside the heat sinks down to T_b will be assumed.

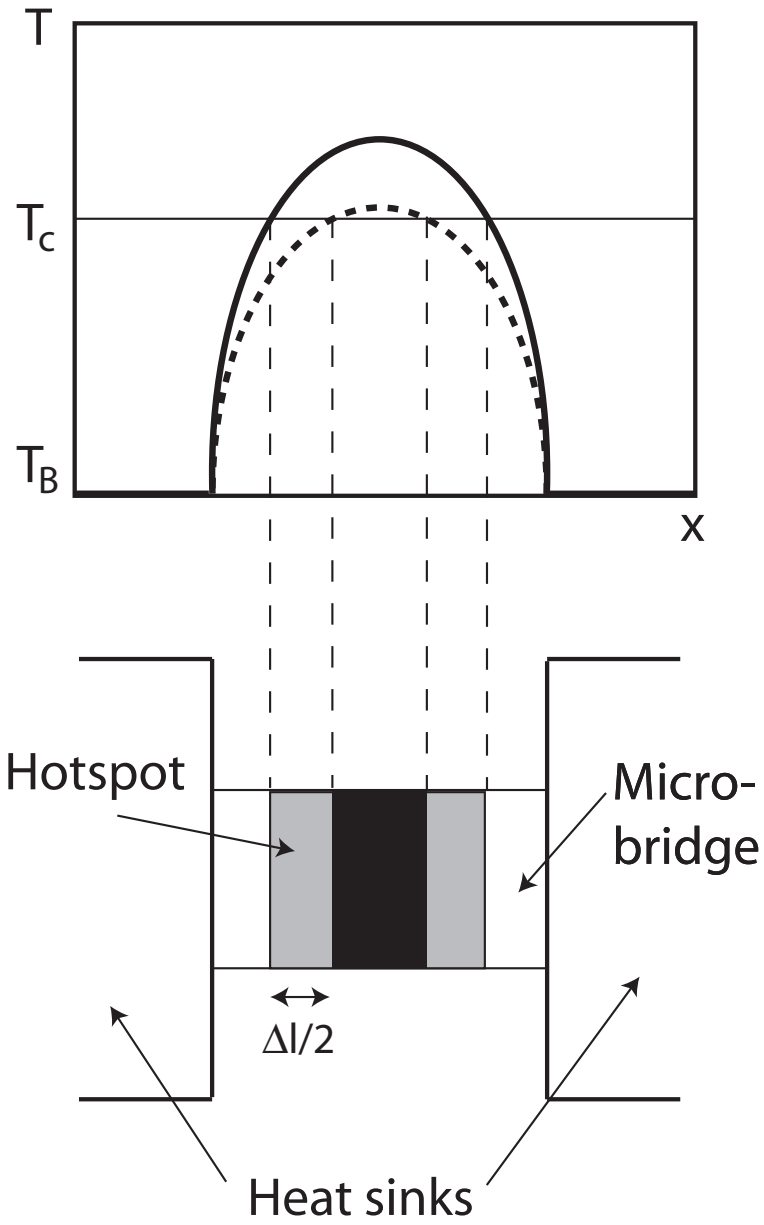

Fig. 2.4: *Plot of two temperature distributions over the bridge length. The bridge borders, being in thermal contact with the heat sinks, are at the bath temperature T_B (in most cases 4.2 K). The temperature rises to a maximum value at the middle of the bridge. The regions of the bridge at temperature $T > T_c$ are normal conducting and marked dark in the illustration. The temperature distribution represented by a broken line corresponds to a lower power dissipation.*

the valid heat balance equations are:

$$\text{Inside the hotspot: } -K\frac{d^2T_e}{dx^2}+\frac{c_e}{\tau_{eph}}(T_e-T_b) = j^2\rho+p_{rf} \qquad (2.13)$$

$$\text{Outside the hotspot: } -K\frac{d^2T_e}{dx^2}+\frac{c_e}{\tau_{eph}}(T_e-T_b) = p_{rf}, \qquad (2.14)$$

being the only difference the fact that outside the hotspot the bolometer bridge is superconducting and the dc-power does not dissipate any heat[4] $j^2\rho$, while both regions dissipate the same amount of rf-current heat p_{rf}. In this (rough) approximation, the heat conductivity K is supposed to be equal over the whole length. In reality K increases linearly with temperature in the normal conducting regions (Franz-Wiedemann-Law) and is exponentially proportional to the number of quasiparticles in the superconducting region.

At the hotspot boundaries in the bridge, as well as at the interfaces to the heat sinks, appropriate boundary conditions are posed to solve the equation system. The solution can be made analytically for very crude approximations but a numerical calculation is needed for better models.

Using equations (2.13) and (2.14) the temperature profile of the HEB and therefore its resistance can be calculated for different dc bias voltages and rf power. The resulting I/V graphs can be compared to the measured plots. For large bias voltages the simulation is good but for low bias voltages —in which the HEB is operated as a mixer— the calculated current diverges while approaching zero bias voltage. In this region, the hotspot length in the bolometer bridge has a large variation range and the change in voltage drop per absorbed rf power (responsivity) is high. The hotspot model fails to predict the HEB characteristics for low dc voltage. The high complexity of the superconducting state in a thin film in the dirty limit subject to high frequency (beyond and below the gap energy) dissipation as well as dc-current transport has still not been numerically modelled.

We have shown above the expressions for η and T_{mix} using the lumped-element model. The results are qualitatively surprisingly similar to those won with the hotspot model.

[4] In reality, the dc-currents are modulated at the IF and do cause heat dissipation in the superconducting region of the bridge.

2.5 Phonon Temperature Distribution and Current-Dependent Resistance

A new distributed model presented at [36] and later in [37, 30] considers the electronic temperature distribution along the bridge as well as the phonon temperature distribution. The mean electron coupling time in NbTiN and NbN τ_{e-e} is very short and hence the mean electron-electron interaction length $l_{e-e} = \sqrt{D\tau_{e-e}}$ is of the order of 10 nm. This means, that for devices with larger dimensions than l_{e-e} an electron temperature distribution should be considered [38, 39]. The lumped element approach is under these considerations not a realistic approximation.

The phonon temperature distribution in a thin superconducting film is less well studied. At the operating temperature the wavelength of a thermal phonon is about 30 nm, which is also below the dimensions of the bolometer bridge. The consideration of a phonon local temperature is therefore also reasonable.

Two coupled heat balance equations are used, one for the electron temperature T_e and one for the phonon temperature T_p:

$$\frac{\partial}{\partial x}\left(\lambda_e \frac{\partial}{\partial x} T_e\right) + p - p_{ep} = 0 \qquad \text{(electrons)}. \tag{2.15}$$

$$\frac{\partial}{\partial x}\left(\lambda_p \frac{\partial}{\partial x}\right) T_p + p_{ep} - p_{ps} = 0 \qquad \text{(phonons)}, \tag{2.16}$$

with λ_e and λ_p the heat conductivity for the electrons and phonons, respectively. The function $p = p_{RF} + p_{DC}$ represents the power absorption or generation per unit volume. A homogeneous power absorption from the LO can be assumed because $\hbar\omega \gg 2\Delta$. The dc power absorption varies locally and is expressed by $p_{DC} = j^2\rho$ dependent on the local value of ρ. p_{ep} is the power transfer from the electron gas to the lattice and p_{ps} the power transfer from the lattice to the substrate. Both are assumed to be temperature dependent [40, 41]:

$$p_{ep} = \frac{c_e}{4\tau_{ep}T_e^3}(T_e^4 - T_p^4) \tag{2.17}$$

$$p_{ps} = \frac{c_p}{4\tau_{esc}T_p^3}(T_p^4 - T_{bath}^4), \tag{2.18}$$

with $c_e = \gamma_e T_e$ and $c_p = \gamma_p T_p^3$ being the specific heat capacities for the electron and phonons, $\tau_{ep} \sim T_e^{-2}$ the mean electron-phonon interaction time and τ_{esc} the mean phonon escape time (into the substrate).

The temperature dependent resistivity can be measured (see chapter 4). Since the temperature is current dependent, the resistivity is current dependent too. The current- and temperature-dependent resistivity $\rho(T, j)$ can be approximated by a Fermi function [42, 43]

$$\rho(T, j) = \frac{\rho_n}{1 + e^{-\frac{T - T_c(j)}{\Delta T(j)}}} \tag{2.19}$$

which represents the local resistivity for a given local electron temperature T_e with ρ_n the resistivity in the normal state and ΔT the width of the superconducting transition. The critical temperature depends on the driven current. The inclusion of the current-dependent resistance has lead for the first time to an excellent simulation of the measured I/V plots of real HEBs [37] also for low bias voltage and seems therefore to be a central issue which had remained unconsidered until now (see chapter 4 for details on R/T and I/V plots of HEBs).

At the boundary to the heat sinks, the phonon temperature is set equal to the bath temperature and the electron temperature decays exponentially inside the contacts. Electrons diffuse into the heat sinks to an extent which is limited by finite interface transparency (apparently only 5% for the interface NbTiN/Au [44]).

The first numerical models only consider the intrinsic resistivity of the superconducting bridge. Newer models include sources of extra dissipation at the contacts which arises through the conversion of normal currents into superconducting currents [45].

2.5.1 Generation of resistance in the bridge due to vortex unbinding?

Another focus of ongoing research focuses on the actual generation process of dissipation in the thin superconducting film. The developing theories are still mostly just qualitative. Many of the needed numerical parameters of electronic and phonon states cannot be measured directly. The ultrathin films are on the boundary of being isolators and depend strongly on fabrication parameters and their characteristics cannot be found in the literature.

In a microscopic approach the local resistance generated by current induced vortex unbinding is considered [36, 30], with the vortices acting as the source of resistance. In the superconductor, upon approaching the resistive state vortex-antivortex pairs exist below the Kosterlitz-Thouless temperature $T_{KT} < T_c$. Above this temperature free vortices emerge with a density N_F. The

free vortices can move due to the Lorentz force, creating a time-dependent phase change, i. e., generating a voltage in the superconductor due to the Josephson relation. A current passing through the system contributes to the generation of free vortices by breaking the vortex-antivortex pairs.

The resistance of the NbN film is in principle given by

$$R = R_N 2\pi\xi^2 N_F(j, T_e) \tag{2.20}$$

in which R_N is the normal state resistance, $2\pi\xi^2$ the area of a vortex core and $N_F(j, T_e)$ the density of free vortices, depending on the current density J and temperature T_e. Although the dissipation leads to a higher temperature of the electron and vortex system, denoted by T_e, the current breaks the vortex-antivortex pairs by the Lorentz force, even in the absence of a temperature rise.

In this model, the free vortices are assumed to move freely in the solid lattice. In future models, the presence of trapping centers at lattice imperfections or impurities limiting the free movement of the vortices should be included in the considerations. Additionally, the effect of the bias voltage on the superconductor has to be considered too. The bias currents —declared as dc— oscillate at the IF (some GHz) and are not conducted lossless by the superconductor.

2.6 Energy transfer processes in the HEB — Cooling mechanisms

In this section we consider the step-by-step transformation of energy in the thin film in order to better understand how the electron gas cools down and how the relaxation rate τ^{-1} can be increased to achieve higher IF bandwidths.

The waveguide mode or the radiation in the quasi-optic lens is coupled through a probe or an antenna into an microstrip mode and is transported to the microbridge (fig. 1.9). The microbridge is (at least partly) held in the resistive state and both superconducting and normal conducting regions are expected to coexist in the microbridge.

Upon absorption of an energy quantum $h\nu$ by either a normal electron or a Cooper pair, the highly excited electron with energy close to $h\nu$ is created. In the case of absorption through a Cooper pair, only one high-energy electron is created due to the large physical size of Cooper pairs, while the second one becomes a low-energy quasi-particle.

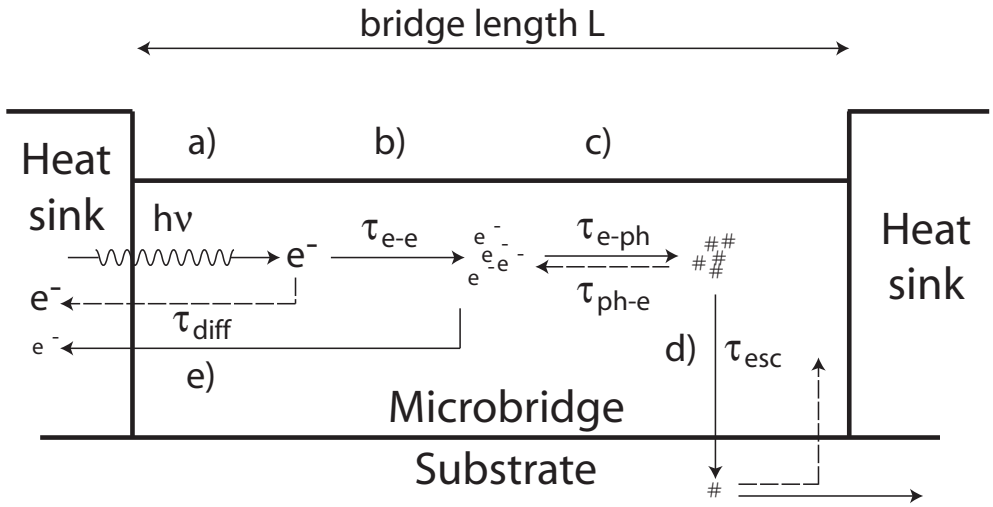

Fig. 2.5: *Symbolic representation of the subsequent steps transforming the energy in HEB from an microstrip mode via electron excitations to lattice and substrate heat. Also the electron out-diffusion is depicted. The electrons are symbolized through e^- and the phonons through #. Broken lines symbolize undesired processes that may appear under certain conditions.*

The excited electron starts to thermalize by electron-electron scattering and high-energy phonon exchange at an extremely fast rate $\tilde{\tau}_{e-e}^{-1}$ (typically $\tilde{\tau}_{e-e}$ ∼1–10 ps). $\tilde{\tau}_{e-e}$ is the inelastic electron-electron interaction time and for dirty-limit films it can be approximately given by

$$\tilde{\tau}_{e-e}^{-1}[s^{-1}] \approx 10^8 R_{\square} T, \tag{2.21}$$

T being the temperature in K and $R_{\square}$ being the sheet resistance in Ω [46, 31].

For the films used in this thesis:

Material	$R_{\square}[\Omega]$	T [K]	$\tilde{\tau}_{e-e}$ [ps]
Nb	13	6	13
NbN	580	8	2
NbTiN	250	8	5

The total interaction time $\tau_{e-e} > \tilde{\tau}_{e-e}$ corresponds to the electronic thermalization time, in which the electron temperature T_e —somewhat above the lattice temperature— is established for all conducting electrons in the thin film. For NbN $\tau_{e-e} \approx 7$ ps [47]. At this moment the electron gas temperature is noticed as a change in the device resistance. This process is depicted in fig. 2.5 b).

Further cooling of the electron gas can now occur in two different ways:

- Outdiffusion of the hot-electrons to the normalconducting regions outside of the bridge.
- Interaction with the lattice; creation of thermal (long-wave) phonons, for which the film is transparent.

2.6.1 Diffusion cooled hot-electron bolometer

The first possibility is that the hot electrons diffuse into the normal-conducting heat sinks as illustrated in fig. 2.5 e). To enhance this effect, superconducting materials with high electronic diffusivity D for the bridge material like Nb are preferred. The hot electrons diffuse into the heat sinks at a rate

$$\tau_{diff}^{-1} = \frac{\pi^2 D}{L^2}, \tag{2.22}$$

The maximum distance to the heat sinks from any point in the bridge $L/2$ must not be too long $L \simeq 100$–300 nm to allow short hot-electron diffusion times. For a 100 nm bridge with a diffusion constant $D = 1$ cm^2/s (Nb), a theoretical minimum time constant of order 10 ps can be expected, allowing a maximum IF bandwidth of 16 GHz to be achieved.

Superconducting HEBs especially designed to promote this cooling mechanism are called *diffusion-cooled* HEBs (see fig. 2.6) and were first proposed by [20]. The operation as a heterodyne mixer depends on fast electron diffusion to the heat sinks. This is achieved through:

- Short microbridge to allow for short diffusion paths.
- Microbridge material with large diffusion constant D.
- Transparent electronic interface between the bridge and the heat sinks.

Part of this thesis was dedicated to diffusion cooled HEBs and produced devices featuring a receiver noise temperature $T_{sys} \approx 1500$ K at 0.8 THz. The noise IF bandwidth could only be measured up to 4 GHz only knowing that the noise rolloff was beyond. Unfortunately, the stability of the HEB was very unsatisfactory. This may be due to the fact that the bridge dimensions were only ≈ 150 nm $\times$ 60 nm. Bridge geometry plays an important role in HEB design. Reducing the microbridge dimensions seems to raise the noise temperature and the mixer instability (at least for NbN phonon-cooled bolometers [48]). Since diffusion cooled bolometers depend on small size to have a good IF

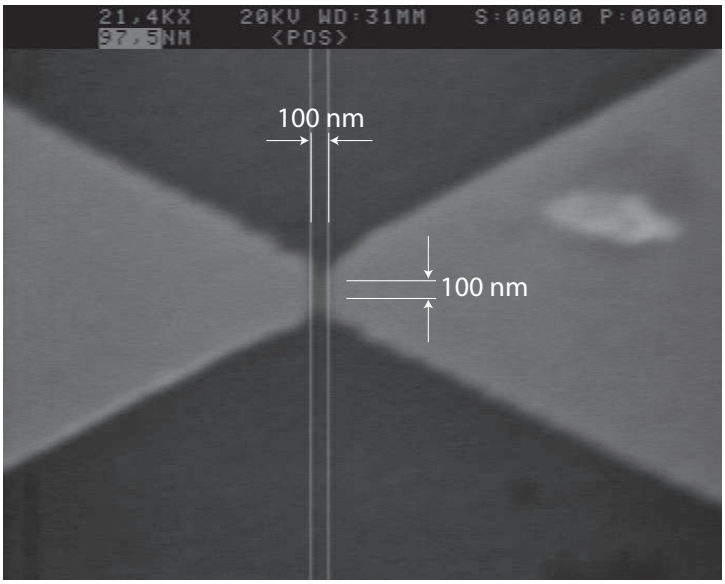

Fig. 2.6: *Scanning electron microscope photograph of a diffusion-cooled HEB. The heat sinks —which are visible here— are usually wider than the bridge itself, which cannot be seen due to low contrast. The Nb bridge is in the dark gap between the heat sinks. The bridge dimensions were ≈ 100 nm long, ≈ 100 nm wide and ≈ 10 nm thick.*

bandwidth, their performance seems to be intrinsically limited by the minimal dimensions still delivering stable operating mixers.

If the bridge is too short, the hot electrons could hypothetically diffuse out of the microbridge before the thermalization process is fully terminated. In this case the temperature change in the electron gas can eventually remain partly unregistered. This undesired mechanism could be responsible for the instability and loss in conversion gain reported for very small HEBs.

2.6.2 Phonon-cooled hot-electron bolometers

The interaction of the electrons with the lattice through the emission of thermal phonons is the second possibility of heat transfer we consider. It is illustrated in fig. 2.5 c)–d). HEBs designed to mainly use this cooling path are called phonon-cooled HEBs (fig. 2.7).

The interaction between the electron system and the lattice is characterized by the mean electron-phonon interaction time τ_{e-ph}. At this rate τ_{e-ph}^{-1} the electrons transfer their excess energy to the phonons. Afterwards the phonons must leave the microbridge transporting the heat to the substrate.

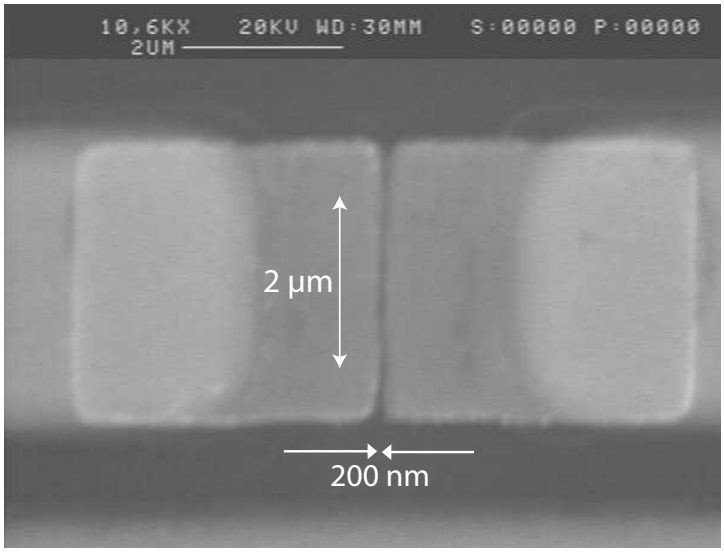

Fig. 2.7: *Scanning electron microscope photograph of a phonon-cooled HEB. The NbTiN bridge dimensions were ≈ 200 nm long, ≈ 2 000 nm wide and ≈ 5 nm thick. Due to the high normal state resistivity of very thin NbTiN and NbN films, the devices must be made very wide to match an impedance ∼ 50 Ω.*

This step is called the phonon escape (into the substrate) and is characterized by the phonon escape time τ_{esc}. If τ_{esc} is too long, the phonons give their energy back to the electrons at a rate τ_{ph-e}^{-1}. To avoid this undesired effect, the *thermostat condition* $\tau_{esc} < \tau_{ph-e}$ must be fulfilled. The relation between electron-phonon and the phonon-electron characteristic interaction times has been empirically studied [21] delivering:

$$\frac{\tau_{ph-e}}{\tau_{e-ph}} \approx \frac{c_{ph}}{c_e}, \tag{2.23}$$

c_{ph} and c_e being the heat capacity of the phonons and the electrons. Using (2.23), the thermostat condition can be expressed as:

$$\tau_{esc} < \frac{c_{ph}}{c_e}\tau_{e-ph}. \tag{2.24}$$

The phonon escape time τ_{esc} can be reduced by making the bridge film extremely thin (usually below 5 nm). For phonons with wavelengths shorter than the film thickness (optical phonons [49]) the travelling time from the top of the film to the substrate interface increases with film thickness. Also a transparent, non-reflecting interface to the substrate is of great importance.

For this reason, sometimes a buffer layer between the substrate and the bridge film is advantageous if the acoustic matching can be improved in this way. The transparency of the interface depends both on the matching of the lattice structure and on the sound velocity of each material. A large difference of the sound velocity leads to reflection of phonons with a large angle of incidence on the interface [50].

The electron-phonon coupling is intrinsically related to the critical temperature T_c. A high T_c is an indicator of good electron-phonon coupling (low τ_{e-ph}) and therefore good heat conductivity from the hot-electrons to the lattice. We may hence affirm that a high T_c is a condition for high IF bandwidth values. To take advantage of this effect, phonon-cooled HEBs are not made of Nb, but NbN or NbTiN, which have a higher T_c than Nb.

The need for an extremely thin film having a high T_c is a very difficult challenge, which has been successfully mastered at KOSMA. 4–5 nm thick NbTiN as well as NbN could be fabricated with a transition temperature of ≈ 8 K [1].

The largest HEB relaxation time is given by the larger time τ_{e-ph} or τ_{esc}. If the microbridge thin film has a poor electron-phonon coupling, heat cannot be removed from the hot-electrons at a sufficiently fast rate and the limiting time is τ_{e-ph}. If the electron-phonon scattering time is short but the hot-phonons remain in the bridge too long, then the effective cooling of the hot-electrons is retarded, because the hot-phonons rebound their energy back to the electrons (the thermostat condition is not fulfilled). Therefore, in this case the IF bandwidth is limited by τ_{esc}.

There is still a very small probability that hot phonons scatter back from the substrate into the microbridge. This is illustrated in fig. 2.5 by a broken line returning from the substrate to the microbridge. The probability of phonon backscattering is proportional to the bridge area on the substrate. This issue becomes increasingly important when the substrate is extremely thin and unable to serve as a thermal reservoir.

2.6.3 Phonon-cooled HEB on membranes

As already mentioned in section 1.3.1, for operation of waveguide mixers at high frequencies it is very important to reduce the thickness of the substrate. The HEB mixers produced in this thesis are fabricated on only 2 μm thick Si_3N_4 membranes. Removing the dielectric substrate virtually eliminates substrate losses and allows the use of large area waveguide probes at higher RF frequencies. Otherwise, the thermal conductivity and the heat capacity

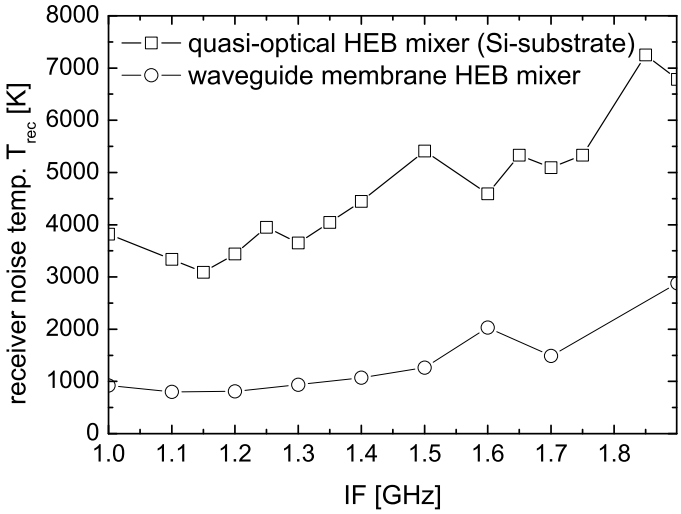

Fig. 2.8: *The receiver noise temperature measured for two similarly fabricated devices at different IFs show no different roll-off independently of their substrate thickness. More recent measurements with an optimized IF amplification show no roll-off up to 1.8 THz (see chapter 6).*

of the membrane are much lower than those of a thick substrate. The reduced thermal drain is eventually not enough to drive the heat away from the bridge. If the heat dissipated at the HEB cannot be efficiently transferred to the substrate, the cooling rate of the HEB is decreased and the IF bandwidth lowered.

The model presented by [51] contemplates these special boundary conditions. In his model two coupled heat balance equations for the electron and phonon temperatures are considered. They are comparable to the equations (2.15) and (2.16) but using an effective phonon conductance

$$\lambda_{p,eff} = \frac{\lambda_e}{10}\left(1+\frac{M}{F}\right),$$

M being the membrane thickness and F the bolometer bridge film thickness. In this model, the Andreev reflection of electrons at the hotspot boundary [52, 53] is considered and estimated to be as high as 12%, which is taken into account for the electron diffusion in the film.

The simulations performed for 1-μm membranes clearly show that the reduction of the substrate thickness, which usually acts as an energy reservoir, now increases the electron temperature in the film. The hotspot forms requiring less p_{LO} and p_{dc}, which implies a reduction of the LO power needed. The

calculated I/V characteristics of a pumped device with optimal mix operation look as if the HEBs were underpumped (i. e. absorbing less LO-power than optimum when compared to thick-substrate-based HEBs). This effect has also been observed in the membrane mixers considered in this thesis. Minimal noise was achieved by slightly "underpumped" operation (see chapter 6).

Our mixers operate on membranes which are 2 μm thick and therefore thicker than the simulated ones. Even for the simulated 1 μm a reduction of the rolloff-IF is not predicted.

The experimental comparison of HEB devices of similar dimensions both on membranes and on bulk silicon in our lab did not show differences in the noise bandwidth up to 1.7 GHz, which was the maximum measurable IF with our equipment (see fig 2.8).

Chapter 3

HEB Fabrication

In this chapter the HEB fabrication sequence is described in detail, which is based on the production of very thin metallic layers and their lithographic patterning.

3.1 Phonon-cooled HEBs

In this section the fabrication sequence for phonon-cooled HEBs on Si_3N_4 membranes is presented. As a starting point, two fabrication recipes for diffusion-cooled HEBs on fused quartz substrates [19] and on membranes [27] had been established. These recipes had to be optimized and adapted for the fabrication of phonon-cooled HEBs on membranes. Following the new fabrication sequence, the most remarkable optimizations will be described and motivated.

3.1.1 Fabrication sequence

A complete fabrication recipe can be consulted in [54]. In this section the basic steps are explained with symbolic diagrams and comments. Completion and DC-testing of a wafer takes a month if all steps work well.

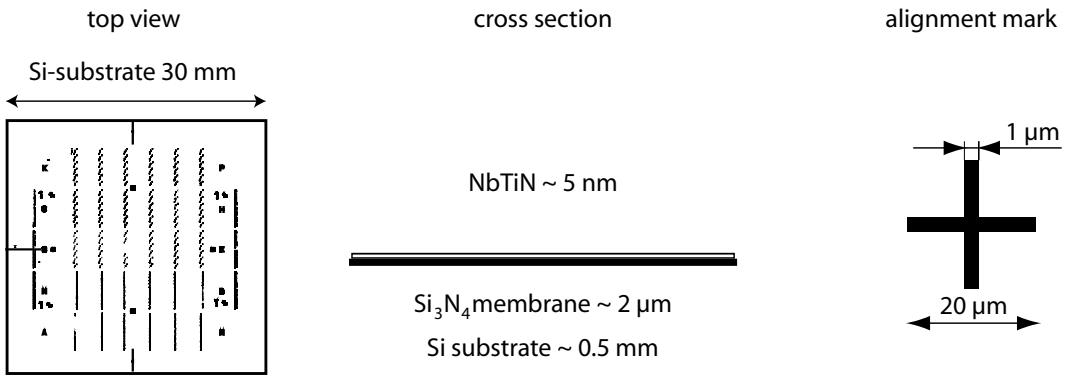

Fig. 3.1: *The Si wafer carries already the Si_3N_4 membrane [55] when processing at KOSMA starts. The first step is the sputtering of the ultra thin NbTiN (or NbN) bridge layer over the whole wafer area on the Si_3N_4 membrane. In the following, the alignment marks are defined by UV lithography and lift-off. A Nb/Au bilayer is sputtered to create the alignment marks on the wafer. On this schematic view the alignment marks are shown over the whole Si wafer on the left and amplified on the right. On a Si wafer 690 HEB devices can be simultaneously produced. On the wafer there are devices for 0.8, 1.2, 1.4 and 1.9 THz. The mask was designed within this thesis in cooperation with T. Tils [23]. The alignment marks are 20 µm large crosses. On the middle the cross section over the bridge length is shown (here the alignment mark is not visible).*

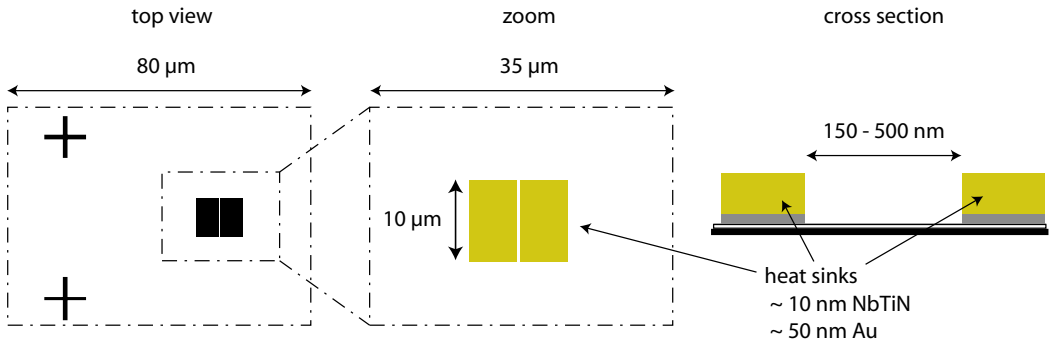

Fig. 3.2: *When the alignment marks are on the wafer, the heat sinks are patterned via Electron Beam Lithography (EBL). The distance between the heat sinks determines the bridge length. The heat sinks have a major influence on the superconducting bridge and therefore on mixer performance. An extended comment on this issue can be found in chapter 4.*

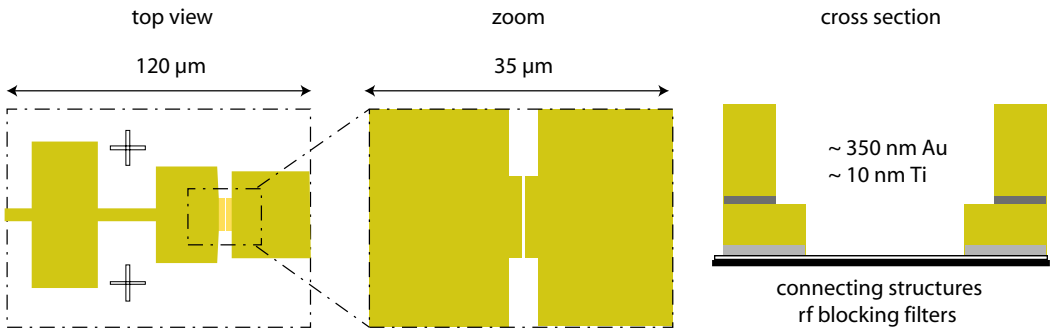

Fig. 3.3: *The filters are patterned using negative uv-lithography. The filters consist of an evaporated bilayer of thin (∼ 10 nm) Ti (for adhesion enhancement) and 350 nm Au for low-loss RF transport. A close-up of a 1.9 THz waveguide probe can be seen on the left.*

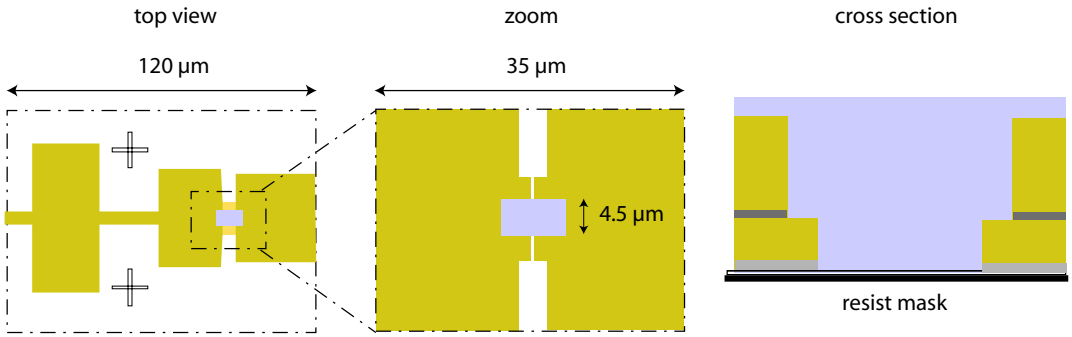

Fig. 3.4: *The original bridge layer (laying over the whole wafer) has to be selectively removed to define the bridge width. A negative electron beam resist is used for this purpose.*

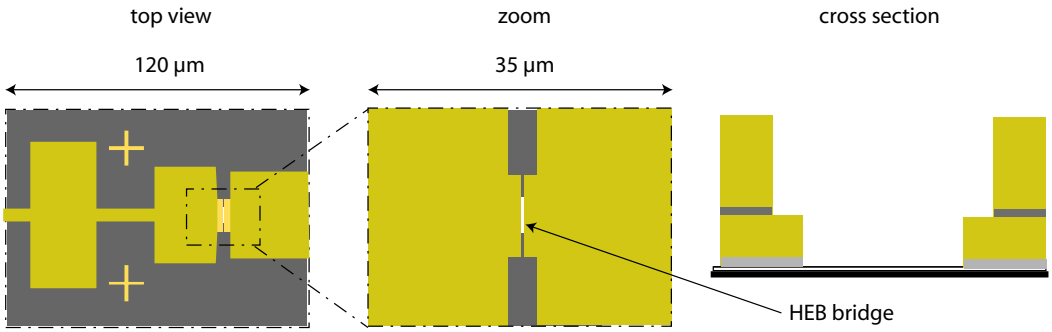

Fig. 3.5: *In this illustration, the Si_3N_4 is painted dark and the bridge clear. The resist has masked the film from the reactive-ion-etch (RIE) with SF_6 and Ar as etching gases. The etch time depends among others from random parameters and the etch success cannot be controlled optically since the underlying Si_3N_4 actually looks same as the (prior to the etch existing) NbN or NbTiN layer. To check if the bridge layer has been removed, a plain ohmmeter is used to determine the resistance measured over the blank parts of the wafer. The resistance grows sharply, when the metallic thin film has been etched away.*

3.1.2 Ultrathin NbTiN

For phonon-cooled HEBs a material with good electron-phonon coupling is needed. NbN or NbTiN are excellent candidates; their comparatively high transition temperature T_c is an indicator of good electron-phonon coupling [56]. Typical transition temperatures for bulk NbN or NbTiN are 16 K. The transition temperature of very thin films of the same metals depend strongly on the deposition method but their transition temperatures are always much lower. Below a certain thickness, it becomes increasingly difficult to grow a continuous film and often the transition temperature is below LHe.

To yield a large IF bandwidth, the thickness of the HEB film must be as small as possible. NbTiN and NbN superconducting films with thicknesses below $\approx$ 5 nm showing a transition temperature $T_c \approx 8.5$ K have been *reactive sputtered* on Si_3N_4 membranes at KOSMA [1].

Reactive sputtering is a method to deposit films which have a different composition from the target by adding a reactive gas to the conventional magnetron sputtering process. The reactions can take place at the target, in the gas phase and on the substrate. Target reactions result in actually sputtering a compound target. These usually have a lower sputter yield (which is the number of sputtered particles of the target per primary ion) than elements and result in a reduction in deposition rate [57]. Attempts to sputter from targets of stoichiometric superconducting compounds produced degraded superconducting properties of the thin film. This is due to the presence of oxides within the grain boundaries inside the target material [58]. Reactive sputtering is the favorable method for the deposition of thin NbN and NbTiN superconducting layers necessary for the fabrication of phonon-cooled HEBs. The films used for the HEBs used in this thesis have been produced by S. Bedorf [1].

The most critical aspect of reactive sputtering is the partial gas pressure of the reactive gas (nitrogen). Its partial pressure in the sputter chamber cannot be just controlled by its gas inlet rate, but is intrinsically linked to nonlinear chemical reactions happening in the chamber plasma and with the target. Normally, voltage or power stabilization is used for the reactive magnetron sputtering.

The nitrogen is first adsorbed by the chamber walls and the sputtered Nb or NbTi particles. When the nitrogen concentration is high enough to saturate the getter processes, the nitrogen creates a a NbN or NbTiN layer on the target surface. Since the sputter rate of these compounds are much lower than for the non-nitrogenized metals, the concentration of sputtered Nb or NbTi in the chamber decreases and much less nitrogen can be adsorbed.

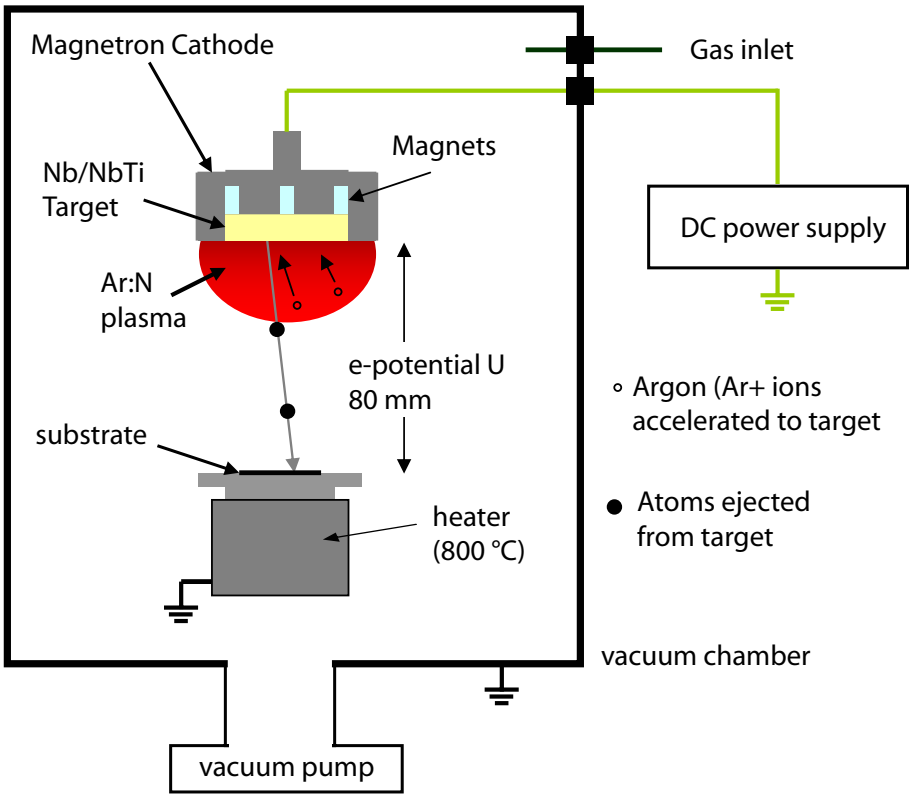

Fig. 3.6: *Schematic view of the sputter chamber showing the (heated) substrate and the target with its surrounding plasma. In this representation, a reactive plasma including N^+ is used to produce NbN or NbTiN, depending on the target material. In our sputtering machines four different sputter targets can be alternatively used. The substrate can be rotated underneath the desired target. Illustration from [1].*

Fig. 3.7: *Schematic representation of a thin compressive film (left) and a thin tensile film (right). A compressive film tends to build discontinuities. A tensile film tends to peel off the substrate. The gas pressure in the sputtering chamber can be varied to control film stress.*

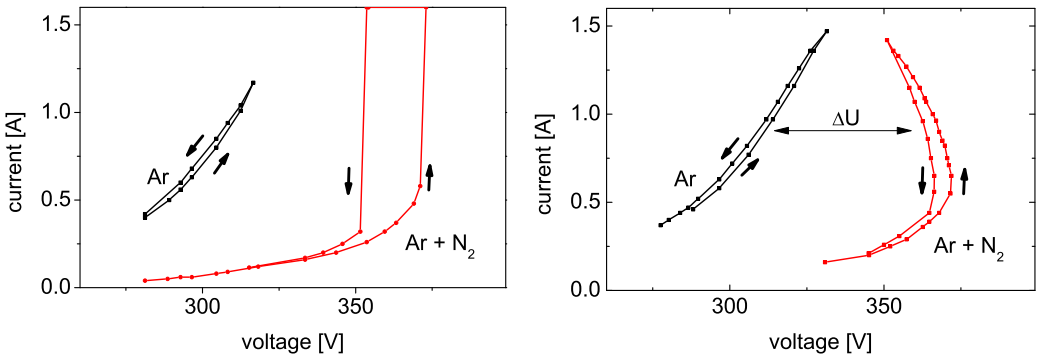

Fig. 3.8: *I/V curves of the magnetron sputter discharge for voltage stabilization on the left and current stabilization on the right. Data from [1].*

Its partial gas pressure rises sharply and the target becomes completely sealed with NbTiN or NbN. The current decreases by constant voltage. These films are deposited with excessive nitrogen and do not become superconducting.

If the N_2 concentration is reduced again or the power increased the sputtered NbTi or Nb concentration eventually rises and adsorbs the nitrogen such that its partial pressure in the chamber rapidly breaks down. The deposited film under such conditions has a too low nitrogen concentration.

The partial gas pressure can be kept constant by controlling the working point on the I/V curve of the glow discharge with a magnetron source operating under the condition of direct current stabilization [59]. The I/V plot for this arrangement, as shown in fig. 3.8 on the right, can be adjusted also for intermediate nitrogen concentrations. When the nitrogen concentration rises and the target becomes covered by a larger amount of NbN or NbTiN, the current between the electrodes is automatically increased to counteract the reduced sputter rate of the nitrogenized metal. A similar behaviour is observed when the nitrogen concentration decreases, the part of the target which is covered by NbN or NbTiN is reduced and the sputtering rate increases. The bias control reduces the current and the gas concentration can be stabilized.

Under current control conditions the gas pressure is hence proportional to the discharge voltage U. The quantity $\Delta U = U - U_{Ar}$ can be easily measured (U_{Ar} is the discharge voltage for a given current using pure Ar as working gas and U the voltage for reactive sputter at the same working current) and is a measure of the nitrogen partial pressure. Actually, the quality of the ultrathin NbN or NbTiN can be reproduced quite well if ΔU is kept constant.

A further necessary parameter to increase the quality of the ultrathin

bridge film is to heat the substrate to at least 600° during deposition. The high temperature enhances the island mobility in the first stages of film formation and enhances film superconducting properties even for very thin films (3–5 nm).

The films used in this thesis are made of ultrathin NbTiN (4–5 nm, $T_c = 8.5$ K).

3.1.3 Bolometer Bridge Length

The bolometer bridge length is determined by the distance of the heat sinks, which are patterned using Electron Beam Lithography (EBL) and thin film deposition on top of the ultrathin NbTiN layer.

Electron Beam Lithography (EBL) is a special technique to create extremely fine patterns as needed for the HEB bridge having structure dimensions going down to 100 nm. The main advantage of EBL over other optical lithography methods consists in the much shorter de Broglie wavelength of the electron beam in comparison to UV-light. Diffraction effects are therefore much smaller. Our UV-Lithography facility can only resolve patterns down to ≈ 1 μm. Otherwise, the EBL takes much longer as UV-lithography. Therefore, it is only used when structures in the sub-micron regime must be patterned.

Essentially, the EBL consists of a focused electron beam which is scanned across the wafer surface covered with a long-chain polymer resist (i. e. Poly-Methyl MethAcrylate, PMMA) which is locally depolymerized by the thermal and dissociating effect of the electron beam. The resulting monomers are soluble in an appropriate developer, while the polymeric long chains are not affected during development.

The sensitivity of the resist is influenced by the resist thickness and by the molecular weight of the polymer, being shorter chains with a low molecular weight more sensitive to the electron beam than longer chains. The molecular weight of the used PMMA must be accommodated to the electron beam energy to achieve a good contrast (vertical other nearly vertical resist side walls under compliance with the desired structure dimensions).

One of the greatest fabrication difficulties faced when producing phonon-cooled HEBs was to introduce a new bilayer resist system. Originally the heat sinks consisted of 70 nm thick gold. Gold is a soft metal and lift-off can be a problem, since it very likely stretches rather than breaks. Gold structures have usually more or less pronounced lift-off problems. For the heat sinks this problem is specially critical, since both heat sinks are so near, that a bridging

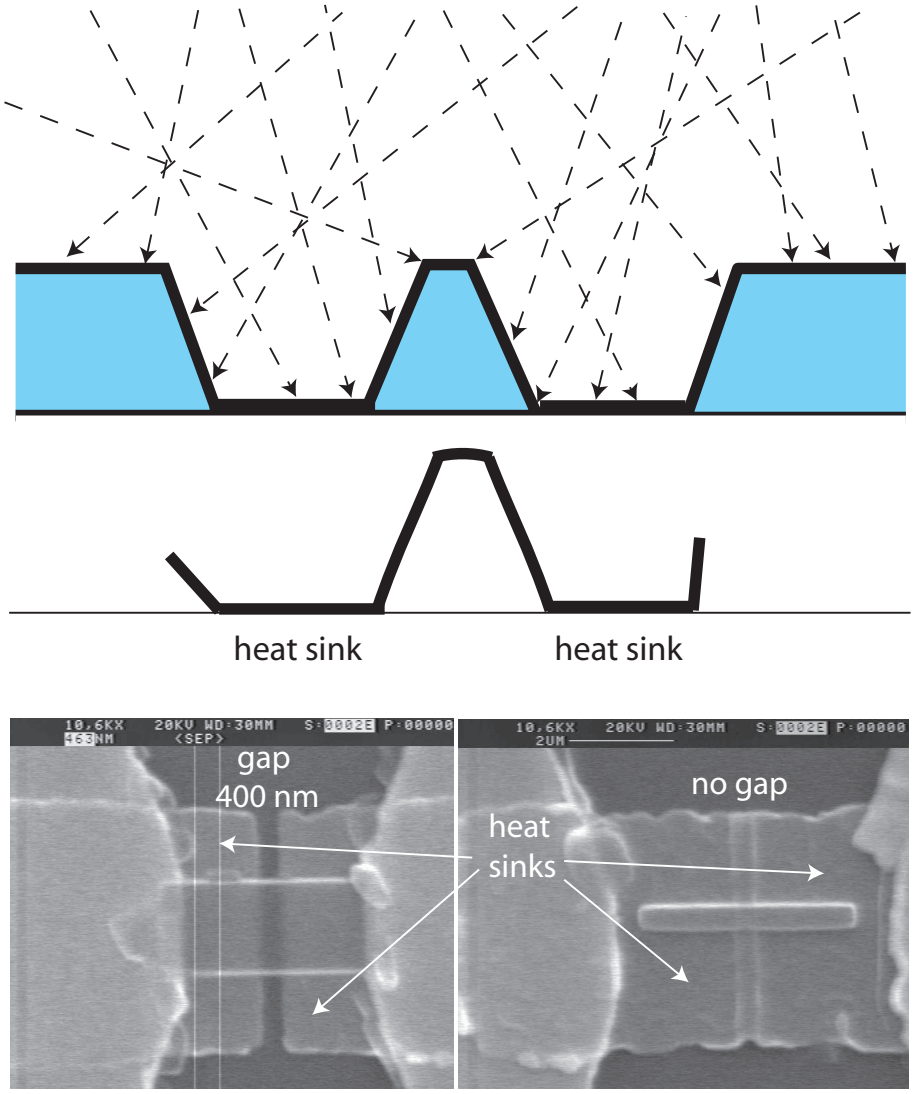

Fig. 3.9: *In the top illustration a side view of a substrate with a patterned resist on top (shaded areas) and a layer deposition (arrows and thick lines) can be seen. In the bottom two scanning electron microscope pictures show two different HEB devices from the same batch. The effect of a bad lift-off for non-undercut profiles is shown. After film deposition (top), the resist is removed but the film does not necessarily lift off, since it is hold by the attached film parts (middle). The heat sinks must be separated by a gap delimiting the length of the microbridge. The heat sinks are made by lift-off of a gold layer which is sputtered on a resist mask. The lift-off for device on the right picture did not work and the gap is shorted by the heat sink gold layer.*

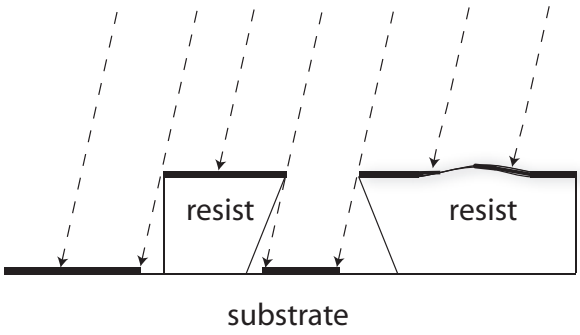

Fig. 3.10: *The broken lines symbolize the trajectory of the material particles in gaseous form, which deposit (thick lines) on the substrate and on the already existing structures on the substrate. The new film does not cover uniformly all surfaces. Shadows are created by the adjacent edges. Roughness is not flattened.*

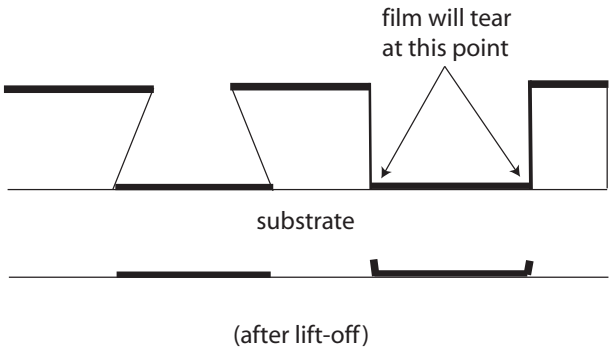

Fig. 3.11: *Schematic representation of a sputtered film on resist with an undercut profile and with vertical resist walls (cross section). After lift-off (bottom) the structures on the substrate have an (almost) definite end.*

gold rest short-circuiting the HEB is very probable as can be exemplarily seen in fig. 3.9. The solution to this problem used until then at KOSMA was to evaporate the gold rather than sputtering it. Evaporating the gold is very advantageous, since the directivity of the deposition makes it easy to find a breaking point for the gold when it is lifted-off (see fig. 3.10). Lift-off of heat sinks with evaporated gold could be achieved with a 400 nm thick PMMA monolayer resist achieving minimum bolometer bridge lengths of less than 100 nm. The heat sinks were bow-tie shaped with a sharp tip which helped increasing the contrast (see below: proximity effect).

Recent research developments have shown that an extra superconducting layer between the bridge and the gold heat sink could enhance mixer performance [60]. A very good interface between the extra superconducting layer

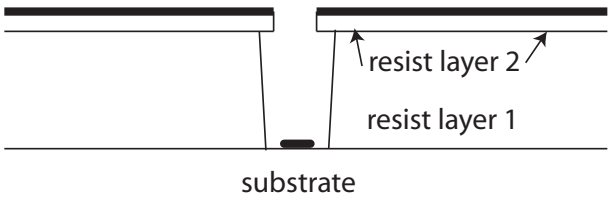

Fig. 3.12: *Schematic representation of a double resist layer on a substrate to produce an undercut profile.*

and the gold on top is needed to avoid any contact resistance. Hence, the superconductor and the gold layers should be deposited in situ, i. e. without exposing the wafer to air between both depositions. This can of course only be realized when both depositions take place subsequently in the same evacuation chamber. In our facilities this is only possible in the sputtering chamber. Both sputter targets are in the same chamber and the substrate can be mechanically conveyed to the position underneath the corresponding target for each deposition. Since sputter deposition needs a clear resist undercut to enable lift-off (or at least vertical resist walls, see fig 3.11), using a single layer PMMA lead to short-circuits on almost every single HEB on the wafer. The undercut profile is usually not naturally given for a monolayer resist (see left side of fig. 3.21 on page 59). Besides, the geometry needed for phonon-cooled HEBs with wide heat sinks leads to a large proximity effect and was a further factor decreasing the contrast of the development. A negative E-Beam resist cannot not been used either, since the area to be exposed would be too large (impracticably long exposure time) and the resolution of negative e-beam resists is usually insufficient for this application.

Therefore, a bilayer PMMA resist system had to be introduced to meet the new requirements: A quite thin layer of PMMA ($\approx$ 50 nm) is baked on a previously baked thick ($\approx$ 500 nm) copolymer (MMA-MAA) layer which is very sensitive to the electron beam. The thin upper layer provides the high definition. The thick underlying layer provides the undercut profile (see fig 3.12). This bilayer resist system made it possible in a first try to pattern *separated* sputtered heat sinks on the substrate. The minimum reached separation was though, still too large $\sim$0.5 μm.

The reason was that the undercut of the used resist combination was too large. The narrow ridge separating both heat sink structures was washed away by the developer (see left picture on fig 3.13).

Applying a (simplified) proximity effect correction and some tricks while developing lead to satisfactory minimum bridge lengths of 250 nm.

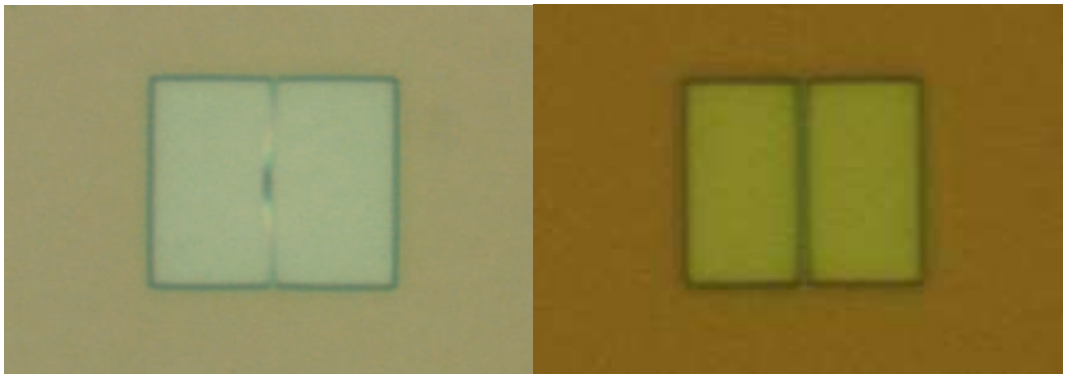

Fig. 3.13: *Optical microscope photograph of a patterned bilayer resist. Left: The bottom layer underneath the separating center bar has been developed away and the top layer is bent. Right: A successful development for a 400 nm gap. Notice the colour change underneath the center bar indicating that the bottom layer has already been partly developed.*

The Proximity Effect in the Electron Beam Lithography

The central phenomenon reducing the EBL resolution is the proximity effect. As already mentioned, the electron beam depolymerizes the long-chained PMMA or other organic polymers into monomers due to the thermal effect of the electrons. First, the electrons are lightly scattered during its path through the resist enlarging the beam width. Second, as the electrons penetrate into the substrate and become slower, the electrons can be scattered back into the resist. The resist receives unintended extra doses of electron exposure because back-scattered electrons from the substrate bounce back to the resist at regions which are far from the beam inlet point (see fig. 3.14). Thus, scattering effects during e-beam lithography result in wider images than what can be ideally produced from the e-beam diameter, degrading the resolution of the EBL system. The proximity effect has to be corrected by reducing the dose (time) of the exposure at densely packed regions and by altering the nominal dimensions of the heat sinks.

The intensity distribution caused by the proximity effect of an electron beam at a radial distance from the beam inlet point r can be modelled by the proximity function $f(r)$ consisting of two Gaussian distributions,

$$f(r) = \frac{k}{\pi(1+\eta)}\left[\frac{1}{\alpha^2}e^{\frac{-r^2}{\alpha}} + \frac{\eta}{\beta^2}e^{\frac{-r^2}{\beta^2}}\right]. \tag{3.1}$$

The first Gaussian corresponds to the forward scattering of the beam and

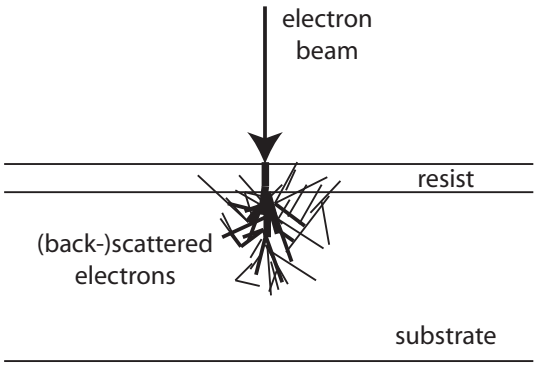

Fig. 3.14: *Proximity effect: Schematic side view of the electrons interaction with the resist and the substrate. When the electrons slow down, they can be scattered back to neighbour resist areas. The effective exposed area is broadened.*

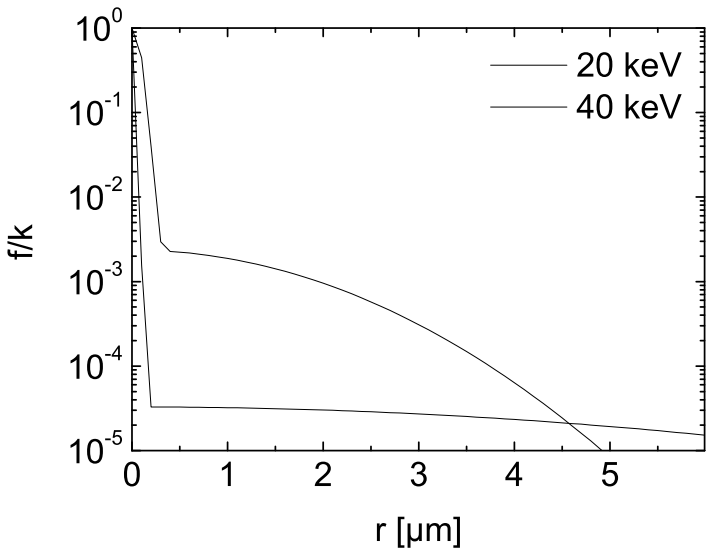

Fig. 3.15: *The intensity distribution $f(r)$ for a circular shaped beam is shown for different electron energies.*

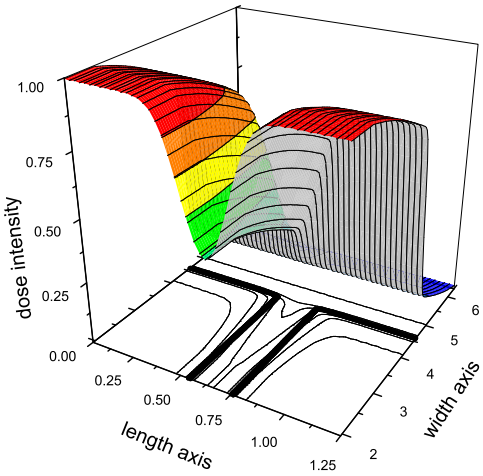

Fig. 3.16: *Zoomed view of the effective intensity distribution at a 250 nm gap (length axis). The intensity has been normalized to 100 units. A projection of the contour lines can be seen on the bottom. The thick lines represent the desired dimensions of the heat sinks.*

α is its standard deviation. The second Gaussian describes the backward scattering being β its standard deviation. k is a constant scaling factor. η quantifies the proportion of backscattering to forward scattering.

Using these parameters the proximity function for two different beam energies (20 keV and 40 keV) for a resist thickness of 550 nm can be calculated using equation 3.1 (see fig. 3.15).

For low electron energies ($\sim$ 20 keV) the effective dose tends to smear towards adjacent regions while for higher electron energies ($\geq$ 40 keV) the effective dose is homogeneously increased over a large region of the substrate. The correction of the proximity effect is more complex for low beam energies. The scanning electron microscope at KOSMA which is used for EBL delivers a maximum energy of 30 keV but is usually operated at 20 keV.

The proximity effect is so essential for the HEB fabrication because it easily leads to an overlap of the heat sinks. The narrow separating resist line is exposed by the scattered electrons and the heat sinks grow together. To avoid this, the exposure dose has been reduced near the edges (first order "proximity correction"). Simulations of the proximity effect on the exposure of the heat sinks can be seen in fig. 3.16. Technical details of the simulation tools can be seen in [54].

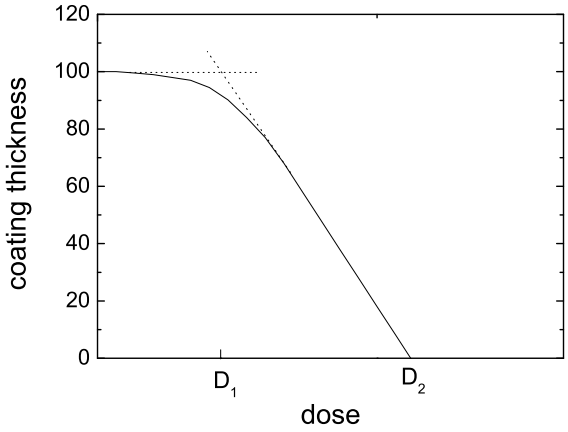

Fig. 3.17: *Generic gradation curve. Relative reduction of the resist thickness as a function of the radiation dose after development. The contrast γ is defined as the slope of the gradation curve.*

Heat sinks definition through overdevelopment.

The second factor determining the pattern resolution of EBL is the resist development. The sensitivity of the resist is defined as the exposure dose for which all of the film is removed. Ideally, the film thickness would drop abruptly to zero at the critical dose after development and remain inert to developer for lower doses. In practice, the resist thickness is etched by the developer also for lower radiation doses. The development is therefore characterized by the relative reduction of the resist thickness as a function of the radiation dose (gradation curve, see fig. 3.17). The contrast γ is defined by

$$\gamma = \left(\log \left(\frac{D_2}{D_1} \right) \right)^{-1}$$

being D_2 the sensitivity and D_1 the dose for which the resist is no more insoluble in developer (see fig. 3.17). The contrast depends on the resist/developer combination as well as other processing parameters such as developing time and temperature. As the bolometer bridge becomes shorter, the required contrast increases, since the space for resist wall gradients becomes scarce. In the limit, low contrast results in an overdeveloped resist line which is no more able to separate the heat sinks during lift-off.

For the used resist combination PMMA/Copolymer, a gradation curve should be considered for each layer. The sensitivity of the copolymer bottom layer is in principle larger than the top layer. Otherwise, the top PMMA layer

is only 50 nm thick and it developed with a high contrast at low exposure doses and short developing times.

After exposure the wafer was immersed in the commonly used PMMA developer consisting of a mixture of Methyl Isobutyl Ketone MIBK / Iso-Propanol Alcohol (IPA) (1:3) for 20–30 s. This is enough to develop the 50–60 nm thick PMMA top layer but the 500 nm copolymer bottom layer remained underdeveloped. If the development is resumed until the bottom layer is completely removed, the top layer becomes overdeveloped and the definition of the heat sinks is no more provided. To solve this problem, a second developing step has been introduced [61].

Different experiments have been performed with different concentrations of water/IPA and MIBK/IPA [62, 63] as a second developer. The most reliable results to remove the (under-) exposed copolymer was a mix of MIBK and IPA in volume concentrations 1:4. This solvent barely affects the already processed PMMA top layer but does etch the shorter polymers of the bottom layer. The gradation curves for MIBK:IPA volume ratio of 1:1, 1:2, 1:3 and 1:4 in [64] (see fig. 3.19) confirms that the reduction of the MIBK component in the solvent lowers the etch rate for large polymer chains.

Although this solvent hardly etches the top-PMMA layer for short developing times, it does affect the resist for sufficiently large developing time, which is actually needed to develop the bottom copolymer layer. This handicap can be largely reduced if the wafer is periodically hot dried on the 90° hot plate during the development of the copolymer. At the first stage of polymer development the solvent penetrates the glassy polymer film forming a rubbery and swollen gel layer at the resist surface [65]. During this stage, which happens more slowly for the PMMA top layer than for the copolymer bottom layer, the top layer is still not depleted. If the wafer is hot dried during this stage, the developer is fully removed. In the next developing cycle the development of the bottom layer can be continued while the developer only penetrates the top layer slowly. In this way, the development time for the bottom-layer can be prolonged without damaging the top layer. Pictures of an exemplary device during the different phases of developing are shown in fig. 3.18.

With this auxiliary method the minimum achieved HEB length (the distance between the heat sinks) has been 250 nm. Devices with lengths around 250–450 nm have been selected for the receivers GREAT and CONDOR. Smaller devices consume less LO-power but their performance is less satisfactory (see chapter 6 or [66] for instance).

The method of underexposing the resist and overdeveloping the wafer

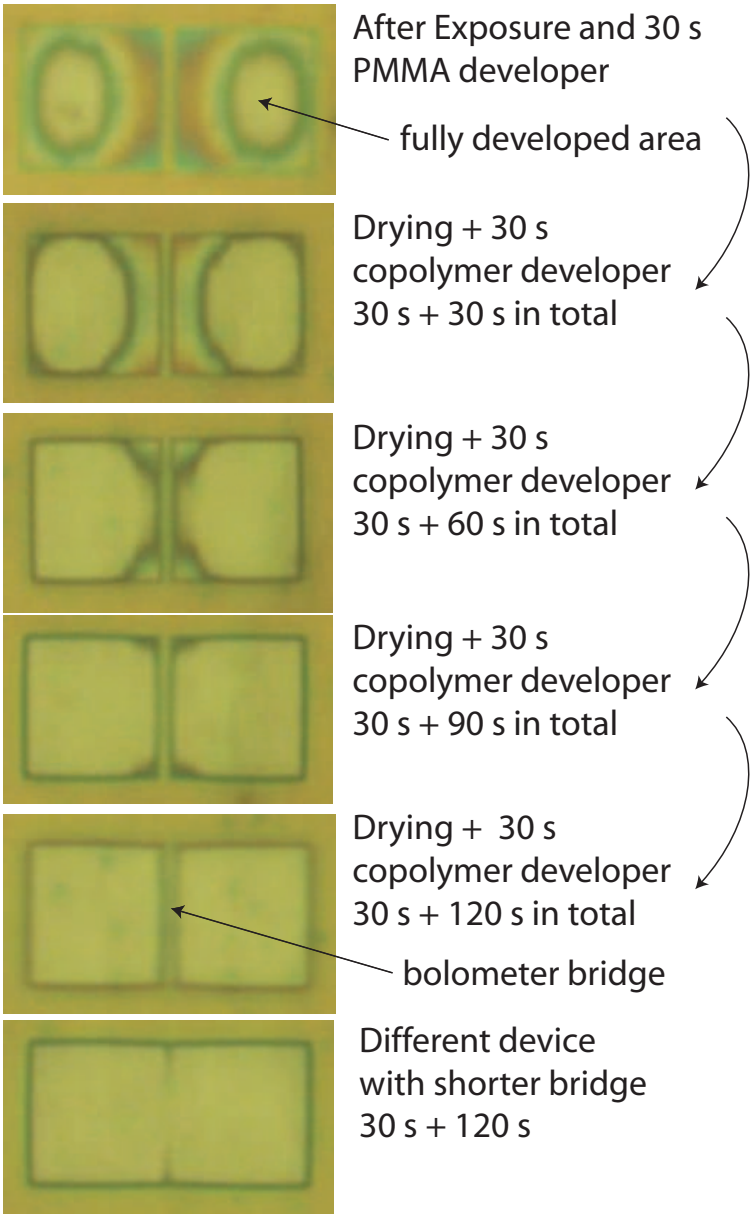

Fig. 3.18: *Microscope photographs of the exposed heat sinks of an exemplary device in different phases of its developing. Another device shown at the bottom with a smaller distance between the heat sinks could not be resolved. See text for details.*

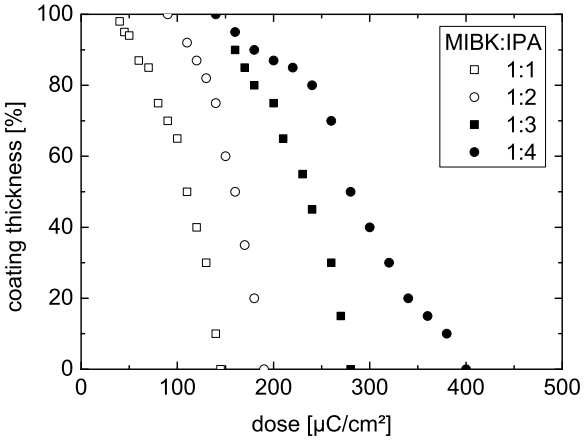

Fig. 3.19: *Experimental contrast curves for PMMA 1150K (molecular weight) using different developer mixtures of MIBK:IPA at 25° C Note the shift to higher doses for lower MIBK concentrations. Data taken from [64]*

.

using two different developers and periodically drying the resist has been very helpful but is not very reliable and should be replaced by other technique for regular production.

3.1.4 Bolometer bridge width definition.

The $\sim$5 nm thick NbN or NbTiN film required for phonon-cooled HEBs has a much larger square resistance ($R_{\square}$(NbN) $\approx$ 580, $R_{\square}$(NbTiN) $\approx$ 250) than the $\sim$10 nm thick Nb film used for diffusion-cooled HEBs ($R_{\square} \approx 13$). Therefore, Phonon-cooled HEBs can be much wider than diffusion-cooled HEBs while

Mask	RIE	ΔT_c
ma-N2403	NF_3, 7 W, 40s	0 K
ma-N2403	SF_6+CHF_3, 18 W, 30s	0 K
Al	SF_6+CHF_3, 18 W, 20s	-0.4 K

Tab. 3.1: *Experimental test on the influence of different etch parameters and masks on the transition temperature. A 5 nm NbTiN film as used for HEB production was diced into several pieces. Film T_c was measured before and after a RIE etch step using different etch parameters and different mask materials. The masks partly covered the test wafer while etching and were removed afterwards using soft wet solvents. ma-N2403 is a negative electron beam resist used in this thesis.*

having the same normal-state resistance. The HEB impedance must be close to the waveguide probe impedance, which can be varied by the probe layout inside certain limits. The design is easier if the impedance value is not too far from 50 Ω, which motivates bridge widths five times larger than the bridge length in the case of NbTiN. A further reason for the large bridge width was the empirical insight, that wide devices seem to operate more stable and noiseless than narrow devices (see chapter 6).

In the originally established method for diffusion-cooled HEBs, bridge widths of 60–70 nm were possible using an Al mask patterned with EBL on a relatively thin (220 nm) PMMA layer. Considering the new requirements of very wide bridges of some microns, a new method has been introduced allowing to save a fabrication step and preventing the bolometer bridge film from an eventual contamination with Al. The Al mask is sputtered directly on the bridge layer and present diffusion mechanisms [67] can deteriorate the superconducting quality of the bridge reducing the sensitivity of the mixer. The subsequent RIE ion impact and heating of the aluminium sheet can assist the diffusion activity.

For wider bridges requiring less absolute definition a negative resist (maN2403) can be used, which eliminates the need for the Al-layer. After EBL the resist itself serves as mask during the RIE. Negative e-beam resists function on the basis of radiation-initiated cross-linking reactions that result in the formation of interchain linkages, which generate a cross-linked, three-dimensional network, which is insoluble to the developer.

Single tests done on a thin NbTiN film show that the new procedure does not affect the transition temperature (see table 3.1.4).

Since the bridges are usually wider than 1 μm, it is also possible to define the bridges width via UV-lithography. This has still not be implemented.

3.1.5 Filter Lines

The filter lines as shown in fig. 3.3 for three different impedances have been designed to couple the waveguide mode into the stripline and to work as a low-pass filter for the IF and a blocking filter for the RF. The change from a dielectric quartz substrate ($\approx$40 μm thick) as used up to 0.8 THz RF to a 2 μm thick membrane has a great influence on the waveguide coupling impedance. Therefore, dedicated waveguide probes for thin membranes were designed and simulated by T. Tils [23] using Microwave Studio [68]. The calculated structures for three different device impedances 20, 40 and 100 Ω and for four different RFs 0.8, 1.2, 1.4 and 1.9 THz were then integrated into

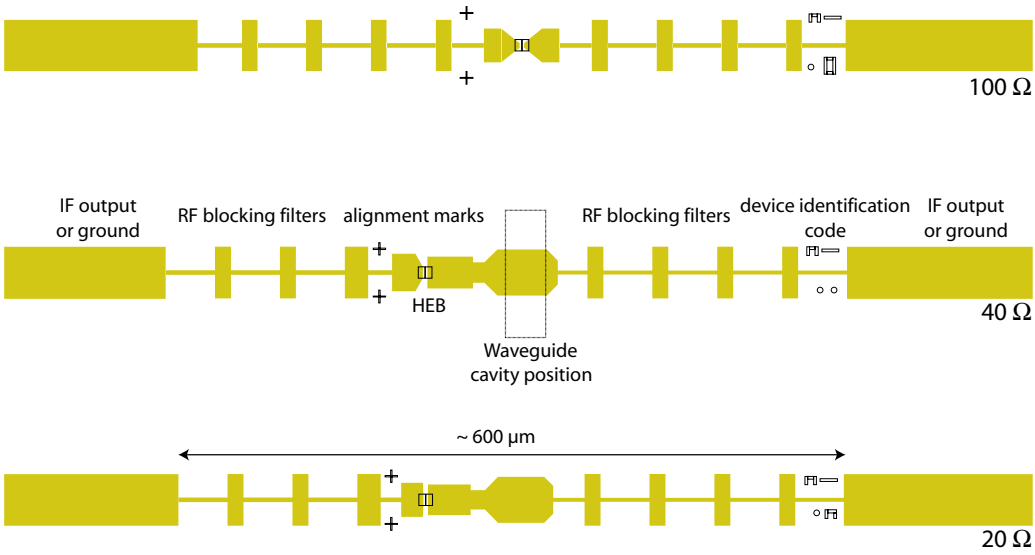

Fig. 3.20: *Three representative designs for 1.9 THz RF (top view).*

a new wafer layout allowing 690 HEB devices to be simultaneously fabricated on one wafer. Using the new layout, masks for all UV-lithography steps were produced by [69].

The wafer is divided in 6×5 columns. Twelve columns contain only devices for one RF, which is important when identical HEBs are needed (i. e. for a pixel array). Each of the resting eighteen columns contain all probe designs for every RF. This spreads the risk of total device loss which is present during the last fabrication step to free the membrane from the supporting Si substrate. In the case that only one column (out of these eighteen) stands all production stages, there will be devices for all different RFs and impedances, delivering mixers at all frequencies.

Difference between positive and negative lithography resists.

Photoresists are materials that undergo photochemical reactions when exposed to light. If the developer removes the exposed parts it is a positive resist. Otherwise it is called a negative resist (see fig. 3.21).

The filters are patterned by UV-lithography. The new mask was designed to use a negative resist which improves lift-off. The better side wall definition of the filters can be seen in fig. 3.22. The original configuration of the filters was a Nb/Au bilayer, which was deposited in the sputtering chamber. To simplify the layer sequence and reduce the number of superconductors, a new filter composition Ti/Au was chosen. Reducing the number of supercon-

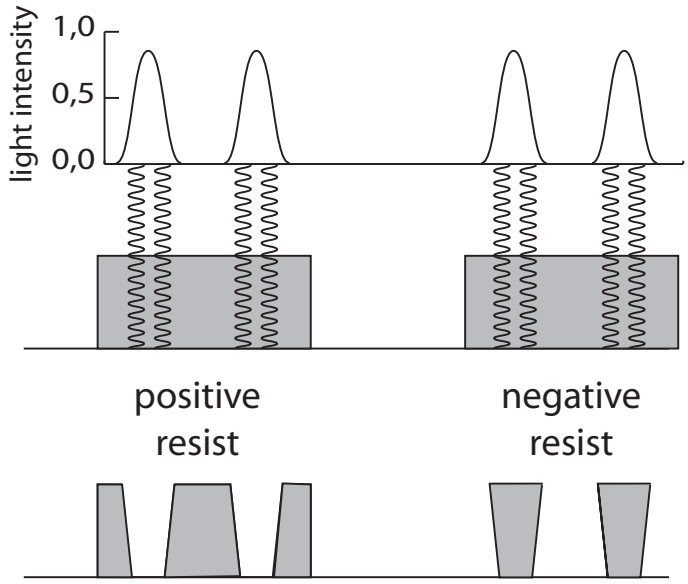

Fig. 3.21: *Schematic illustration of the behaviour of different resists irradiated by light (cross section). The top drawing illustrates a resist layer while exposure. The bottom drawing illustrates the resist after development.*

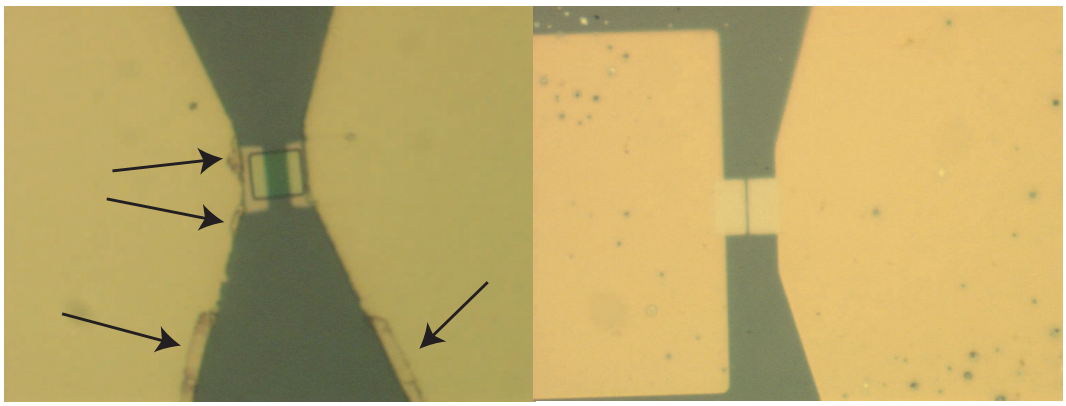

Fig. 3.22: *Optical microscope pictures of the heat sinks and the filter structures. Notice the definition difference for the filter structures. Left side: the old method with positive resist and sputtering shows lift-off residues (pointed out by the arrows). Right side: the new introduced method with negative resist and evaporation shows soft side walls and no lift-off residues.*

Fig. 3.23: *Schematic representation of the steps to pattern a layer via masking and etching. In the first step (left) the metal layer covers the whole wafer. In the second step (middle) resist structures are brought via lithography onto the metallic layer. In the third step (right) the metallic layer is etched and the resist is subsequently removed away. The surfaces which were covered by the resist were protected during the etch step and remain therefore on the substrate.*

ductors could have simplified the interpretation of the electric characteristics of the devices. The new bilayer Ti/Au was evaporated instead of sputtered, since Ti is not available as a sputter target at KOSMAs sputter chamber. No noticeable changes have been observed in the device characteristics but for the introduction of a small series resistance due to the conduction resistance of the filter lines, which did not exist before.

3.1.6 Sputter etch processes

When the ions are not accelerated towards a target but towards the wafer, the sputtering effect of a plasma can also be used to physically remove a thin layer from a surface. Normally this is done using some (protecting) mask material, which prevents the plasma from removing the whole film. In this way a pattern can be transferred to the film (see fig. 3.23).

Reactive Ion Etch (RIE)

In the fabrication of phonon-cooled HEBs, the RIE is used to selectively remove the bridge layer. Another application is the etching of Si_3N_4 for the patterning of membrane structures, as will be outlined in chapter 5.

NbN and NbTiN are etched with chemically active fluor. The F^- ions generally lead to chemical reactions with the surface producing volatile compounds and supporting the mechanical sputter etch. The etch time and power are not reproducible: On the superconductor, an oxide layer, eventually also chemically inert resist byproducts, mask the metallic layer from the chemically active etch gases for an undefined time length. During this time, which is different for each batch, only physical ion bombardment etches the surface.

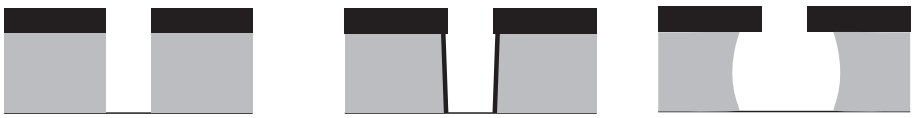

Fig. 3.24: *Schematic illustration of the difference between fully anisotropic (left), isotropic with side-wall passivation (middle) and fully isotropic (right) etch. The resist mask is black and the etched material grey.*

Physical sputtering results from bombardment by ions that move along electric field lines. Since field lines are always perpendicular to an equipotential surface, then physical etch profiles are inherently vertical in contrast to the isotropic profiles observed with (wet) chemical etching. When the sputtering ions react chemically with the surface, then also isotropic etching is observed. For some materials and gas compositions the reaction products are non-volatile and deposit on the etched surface masking it from further chemical reactions. The surfaces perpendicular to the field lines are physically etched while the side walls remain masked. This is called side-wall passivation (see fig. 3.24).

Soft sputter etch for surface clean

Prior to vacuum processes such as evaporation and deposition by sputtering it is useful to clean the substrate surface in situ.

Glow discharge cleaning involves placing the substrates to be cleaned in a glow, so that they are bombarded by low energy ions and electrons. Sometimes the cleaning is carried out in an oxygen discharge. This has the advantage, that there will be an effective oxidation of the organic impurities on the surface by atomic oxygen formed dissociatively in the discharge, and these oxides will generally be volatile. Residual oxygen on the surface can even form an intermediate layer and in the subsequent deposition enhance film adhesion to the substrate.

Sometimes it is also necessary to sputter clean the surface with inert gas ions such as Ar^+ to remove also the oxide layer. In contrast to the glow discharge, sputtering is encouraged and the substrate is cleaned by removal of its surface. Glow discharge alone is ineffective in removing the native oxide layers or other compounds from metal or silicon surfaces.

The material of the substrate holder will also be target for energetic ions. The holder material can also be sputtered and deposit on the substrate as an unwelcome impurity. It is hence necessary to previously cover the substrate holder with an appropriate material (usually Nb has been used as covering

material for holders). In this way it is guaranteed, that any *backsputtered* material from the holder plate will not be an undesired contamination.

Chapter 4

DC-Measurements

During fabrication, success can only be controlled optically. This allows sometimes to identify if some step has not worked properly but many failures often remain unnoticed.

DC measurements are a powerful tool to retrospectively evaluate the fabrication process and characterize the HEBs. Since many devices can be DC tested in a short time, statistical data are easy to obtain. The heterodyne behaviour can still not be predicted by DC data but damaged devices can be identified. A relative comparison is possible: A series of devices with almost identical DC features can be expected to show similar RF performance, as needed for pixel arrays.

DC measurements take place using a *dipstick*, a measuring probe which can be dipped into a standard liquid helium (LHe) transport dewar (see fig. A.1 in the appendix A). The wafer is diced into 30 small pieces with 23 devices each[1] and glued to a (copper) probe holder. The devices are electrically bonded to a circuit board on the probe holder which can be easily handled and inserted into the dipstick socket. It is then possible to switch manually any single device.

During this thesis a new dipstick was designed and manufactured in cooperation with the mechanical and electronic workshops at KOSMA. The new dipstick can contact 44 devices at once and includes a temperature sensor. Cooling down the dipstick from room temperature to LHe temperature and warming it up after measurements takes about one hour.

[1] During fabrication the devices are connected by a ground loop. Before DC testing the wafer is diced in smaller pieces separating individual devices electrically. On each wafer piece there are 23 devices. A wafer piece measures $\approx 3 \times 5$ mm^2.

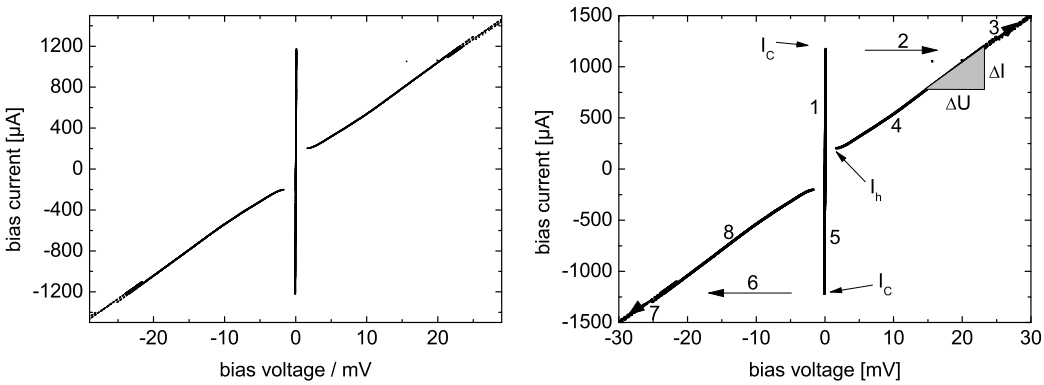

Fig. 4.1: *Current vs. voltage characteristic of a HEB device at 4.2 K (left: without labels). The hysteretic behaviour is indicated on the right by the order numbers. The critical current I_C is the current needed to suppress superconductivity. The normal conducting bridge dissipates heat, superconduction is restored at the current $I_h < I_c$. The normal state resistance of the device is read from the graph slope as indicated.*

4.1 Critical Current and Critical Temperature

Two types of measurements are usually performed:

- The devices are at LHe temperature. Current vs. voltage is measured and an I/V-plot is produced.
- The dipstick is slowly immersed into the LHe (or pulled out of it) and the device is biased at a constant current bias. Resistance to temperature is measured (R/T plot).

These two measurements can be performed using the same dipstick, but the readout is done on different measurement setups.

4.1.1 Current vs. Voltage Characteristics

The devices are cooled down to LHe temperature and a PC-controlled bias box scans the operating points to obtain an I/V graph as shown in illustration 4.1. The bias supply box sweeps the bias current for the device and amplifies the returning voltage.

An exemplary HEB I/V plot is shown in fig. 4.1. The superconducting state of the HEB is indicated by current transport at $V = 0$ V (vertical line in the graph). The maximum current at $V = 0$ V is the critical current of

the device I_c. For larger currents $I > I_c$ resistance sets in and a voltage is measured. The resistance measured for $I > I_c$ is referred to as the normal state resistance and is taken from the I/V plot slope as indicated in fig. 4.1 (right side). The device shows a hysteretic behaviour and does not return to the $V = 0$ V line when the bias current is again reduced to $I = I_c$. The measured voltage becomes zero again when the bias current is reduced down to $I_h < I_c$.

This I/V behaviour is usually explained in terms of the superconducting transition of the bolometer bridge. Superconductors can carry dc-currents without dissipation (zero voltage) up to a definite critical current density $J_c(T) = I_c(T)/A$, being A the cross area of the superconductor. A voltage is measured (the normal conducting state sets in) when the critical current density $J_c(T)$ is surpassed somewhere in the superconductor, due to the current $I > I_c$ (with constant A) or due to a constriction in the device $A < I_c/J_c$.

Devices having good RF performance showed in the I/V plot a sharp transition from the superconducting state into the normal conducting state as exemplary shown in fig. 4.1. Some devices show steps in the DC-I/V curves or a gradual-continuous transition from the superconducting state which hint at discontinuities, weak spots in the device or a deteriorated superconducting film. These devices were not used for mixers.

When the HEB is in the normal conducting phase, reducing the dc-current under the critical value I_c does not immediately lead the bridge to recover the superconducting phase. This is usually explained by the self-heating effect originated by the heat dissipation in the thin bridge by the dc-current ($P = I \cdot V$). The temperature increase lowers the value of the critical current. I_h is the minimum current to sustain a normal conducting region in the bolometer bridge.

During the RF measurements as a heterodyne mixer the HEB is usually kept at LHe temperature and a bias box sweeps the I/V curve of the HEB. The HEB is heated up to its working temperature by the radiation power of the local oscillator P_{lo}, which is coupled into the HEB. The P_{lo} is adjusted to suppress the hysteretic behaviour of the I/V curve.

Fig. 4.2 shows the power dissipated at I_h, $P_h = I_h \cdot V_h$ for several devices plotted against the HEB volume. The DC values originate all from HEBs from the same batch having the same NbTiN film and contacts. The spread probably originates from the fact that it is difficult to exactly determine P_h, since the HEB and the measuring electronics are in an unstable state at I_h.

For some devices, the required LO-power has been carefully estimated from RF measurements using the isothermal method (see chapter 6 and com-

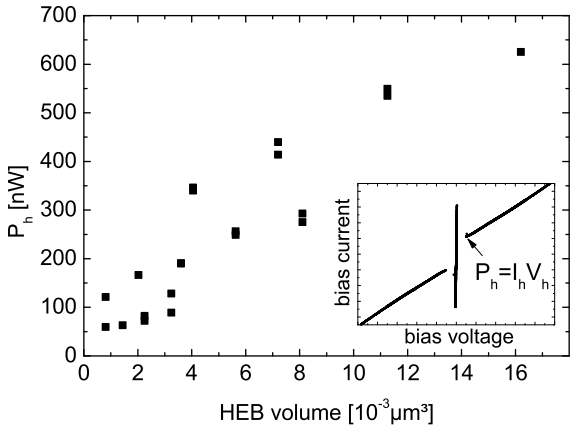

Fig. 4.2: *The power dissipated for I_h has been calculated (see inset) and is displayed for some devices of a batch with variations in the bolometer bridge volume.*

Mixer	RF-Estimation	P_h
2010 [70]	300 nW	415 nW
312 [71]	400 nW	356 nW
311 [72]	350 nW	360 nW
519	200 nW	230 nW

Tab. 4.1: *The estimated LO-power need of some devices is compared to the calculated P_h value.*

pared to their P_h-value. These data are listed in table 4.1. There seems to be a correlation between both values which should be further investigated. Knowing the approximately required P_{lo} prior to RF measurements would be a useful tool.

4.1.2 Resistance vs. Temperature Characteristics

The superconducting transition temperature is obtained varying the temperature at a constant current bias and measuring the resistance dependence on temperature with a four-point measurement. The precision obtained with the R/T setup is much better since Lock-In-Amplifiers are used to eliminate noise. This leads to a resolution in resistance of 20 mΩ which can resolve tiny resistance variations like the ones caused by proximity effects, or as it is needed for Van der Pauw measurements [27]. Synchronously the temperature at the sample is monitored and logged together with the measured resistance.

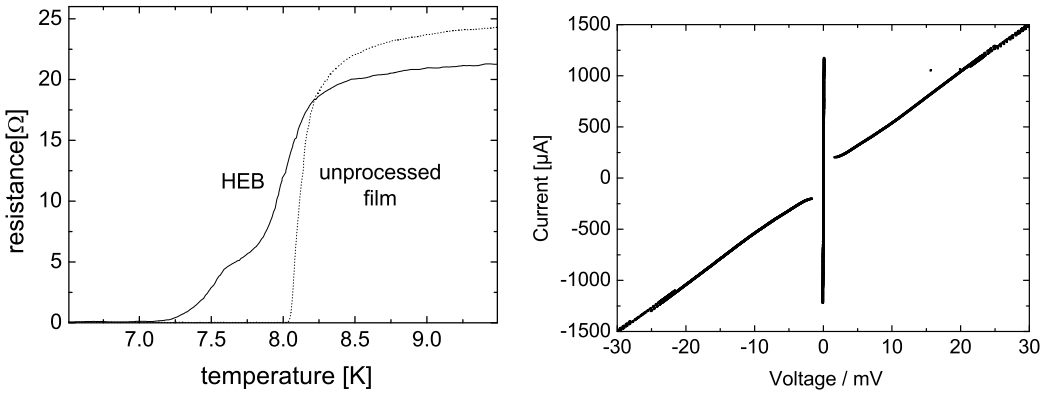

Fig. 4.3: *Measured resistance dependence on temperature of a HEB showing two superconducting transitions at $T_{c1} = 7.45$ K and $T_{c2} = 7.99$ K. The superconducting transition for the same film before processing is also shown at $T_c = 8.13$ K (dotted line). The bias current for both measurements was 1 μA. The corresponding I/V graph of the same device is shown on the right.*

To vary the temperature, the dipstick is slowly pulled out of the LHe or slowly immersed into it. If this measurement is done at different fabrication stages, the negative effect of processing on the transition temperature for different batches can be compared. A measurement of T_c is normally done right after the deposition of the bridge layer and then after completion of the fabrication sequence. A reduction of $\approx$ 1 K in the critical temperature is a realistic figure [73].

The R/T graph of a finished device shows more than one superconducting transition (see fig. 4.3). This can be explained using the superconducting proximity effect. When a superconductor S is brought in good electrical contact with a non-superconductor N, both metals influence each other at the interface (proximity effect). Cooper pairs can leak from S to N. The result is that the critical temperature of the superconductor at the interface is lowered and to an extent the normal conducting metal becomes superconductor. At low temperatures, the proximity effect has a macroscopic length scale. For instance in gold at 1 K, the penetration length is of the order of 1 μm [74]. For the very thin films used in this thesis the proximity effect extends over their whole thickness.

There are several models (for instance [74, 75, 76]) to predict exactly to which extent the critical temperature of a superconductor S_1 is influenced by another superconductor S_2 or by a normal conductor N. Certain material parameters must be known: Thickness, resistivity, Fermi velocity, electronic

diffusion, electronic mean free path, effective electronic mass and interface transparency. Many of these values are either not available for $\sim$5-nm NbTiN films or the values found in the literature are contradictory. This shows that the film deposition conditions, its growth structure and so forth have a major influence on electronic characteristics.

In our case the complexity additionally increases, since a multilayer sandwich of two superconductors must be considered. On top of the NbTiN bolometer bridge film a superconducting contact layer has been deposited to enhance RF performance (see below).

A qualitative interpretation of the observed R/T plots is though interesting to optimize fabrication parameters and characterize the parameter variations which lead to better RF performance. This is the main focus of the following sections.

4.2 Heat Sinks Fabrication Parameters

In this section DC measurements of many HEB devices are systematically studied. Certain parameters, such as bridge geometry, layer composition and clean parameters can be systematically altered to identify how the resulting R/T curves measurements are exactly influenced.

As already mentioned before, the heat sinks seem to have a large influence on RF-performance. In conventional phonon-cooled HEB devices the heat sinks are made of gold (mostly using a very thin, 5–10 nm, titanium buffer layer) and there is no additional superconductor. A usual problem is the *contact resistance* at the interface which arises from the native oxide layer growing on the bridge layer during processing. The originating series resistance has a non-reproducible nature and results on a spread of coupling impedances for devices which are otherwise identical. Besides some of the RF power is dissipated at this resistive interface loosing therefore sensitivity and heating up the bridge in an unpredictable manner.

The oxide layer can be removed by sputter cleaning the surface previous to heat sink deposition as has been done for the previously shown batch. This is a critical step since the bridge layer itself is only a few nanometres thick and can be easily damaged.

The improved interface transparency enhances the superconducting proximity effect too. The superconducting properties of the bridge layer underneath the normal metal heat sinks are hence depleted. To counteract this effect, and the fact that the bridge layer can be damaged by the sputter etch step, the additional superconducting layer has been introduced yielding

an improvement in RF mixing properties [60]. The noise temperature of the receivers based on the mixers with optimized contacts reaches 1000 K at RF 2.5 THz. In this case, the mixers with non optimized contacts of the same volume demonstrate noise temperature of 2200 K. However, close values of the noise temperature have also been achieved in other laboratories without additional superconductor, but for larger-volume mixers (1300 and 3100 K at local-oscillator frequencies 2.5 and 3.8 THz, respectively) [77].

To investigate this effect a batch has been produced with different clean parameters for different regions of the wafer. The wafer was processed as a whole ensuring that all other fabrication parameters were identical for all devices. While heat sink deposition the wafer was covered by a metallic plate covering the whole wafer except for the chosen region containing 15–20 devices. From a total of eight different clean and deposition parameters only three different variations will be discussed[2]. Unfortunately, an uncleaned device with fully normal conducting heat sinks could not be processed:

1. No clean
   8 nm NbTi + 50 nm Au.

2. O_2 clean, 3 W, 6 s, 142 V
   Ar clean, 6 W, 5 s, 240 V
   15 nm NbTiN + 50 nm Au.

3. O_2 clean, 3 W, 6 s, 142 V
   Ar clean, 6 W, 5 s, 240 V
   15 nm NbTiN + 50 nm Au.

For each experiment at least ten devices with different dimensions could be dc-measured. The variation in the bridge geometry is very useful to interpret data[3].

4.2.1 No Clean

In the first experiment, the heat sinks consisting of an 8 nm NbTi - 50 nm Au bilayer were directly deposited on the bridge layer[4] without previous clean.

[2]The other five were unfortunately not correctly processed due to local variations in plasma intensity while etching the bridge layer away. While some of the devices located in the center of the wafer were correctly etched, other located aside were only partly etched.

[3]Only through the statistical comparison of many devices it is possible to identify fabrication failures.

[4]The transition temperature for a 300 nm thick film of NbTi (300 nm hot sputtered and annealed) is $T_c = 10.6$ K [78]. The transition temperature of the NbTi used here is much

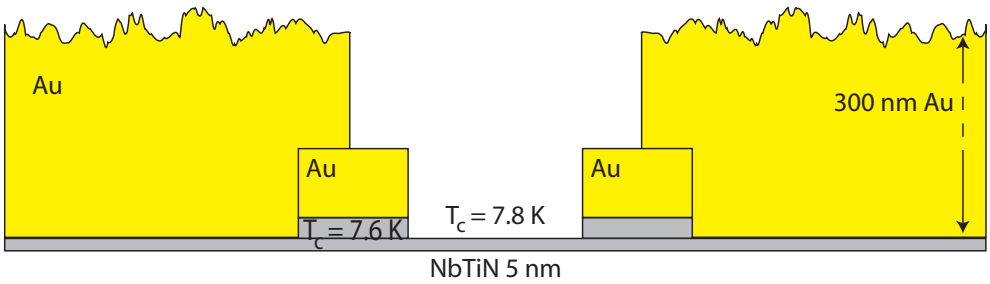

Fig. 4.4: *Schematic cross view of a HEB. For I/V measurements at $T = 4.3$ K, dc currents flow through the superconducting bridge layer, which extends over the whole wafer. The indicated critical temperatures are taken from fig. 4.6.*

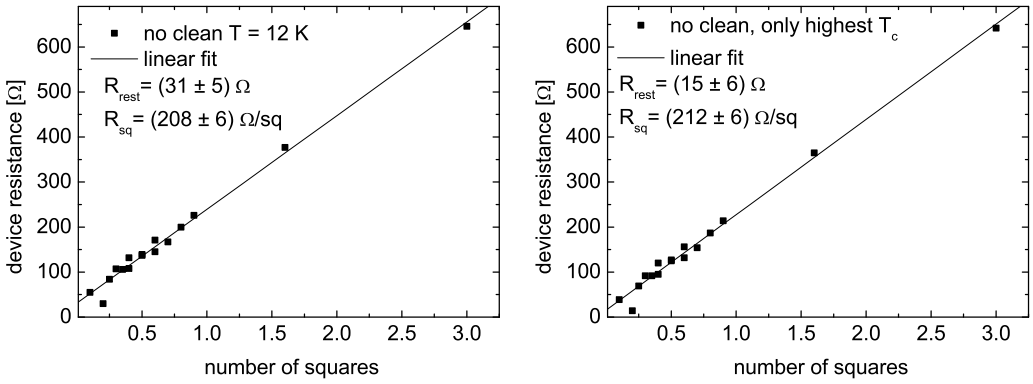

Fig. 4.5: *Plot representing the dependence of device resistance on bridge dimensions (length/width). Data were obtained from the corresponding R/T graphs (measured at $T > T_c$). The resistances in the right plot correspond only to the superconducting transition with the highest T_c (see text).*

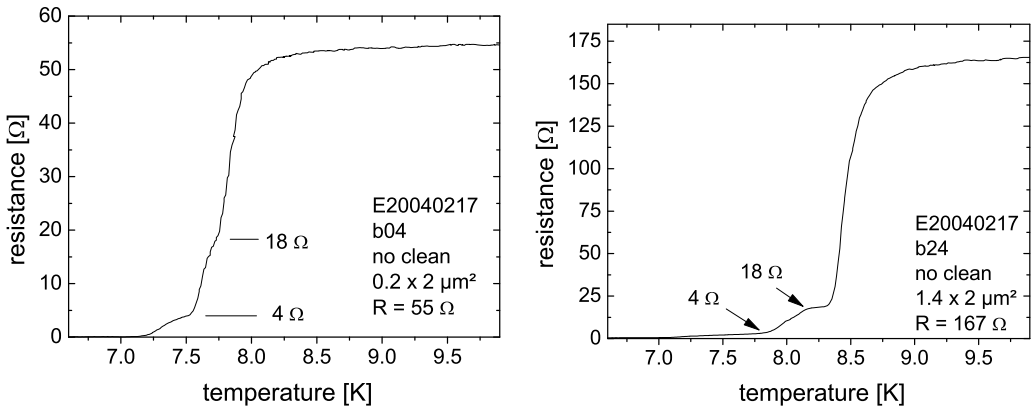

Fig. 4.6: *R/T plots for two exemplary mixers (short and long bolometer bridge).*

In fig. 4.5 (left) the resistance measured at the R/T graph for several devices of this batch is plotted against their square number (device length/device width).

The R/T graphs of these devices show three superconducting steps (fig. 4.6). The steps with the lowest transition temperature add to 18 Ω and are independent of device dimensions. Therefore, it has been assumed that these steps do not arise at the bolometer bridge but at the NbTi of the contact pads and the NbTiN underneath the filter lines, see fig. 4.4).

The plot on fig. 4.5 on the right shows the resistance of only the highest T_c transition (see fig 4.6) against the square number of the bolometer bridges. The interpolated resistance of a zero-square bolometer bridge shows a residual resistance of 15$\pm$6 Ω. This resistance could be due to the contact resistance or eventually to the recently studied intrinsic resistivity of the superconducting bridge at the normal-metal superconductor interface [45]. It should be noticed that the linearity of the plots shown on fig. 4.5 was not expected for an uncleaned interface.

4.2.2 Soft Clean: 5 s Ar

In the second batch the heat sinks were deposited on a sputter cleaned surface. A soft (6 s, 3 W) O_2 clean was performed followed by a 5 s, 6 W Ar sputter clean. The O_2 plasma removes organic and PMMA rests but oxidizes the surface. The following 5 s Ar sputter clean serves to remove metallic or oxide

lower due to its thickness.

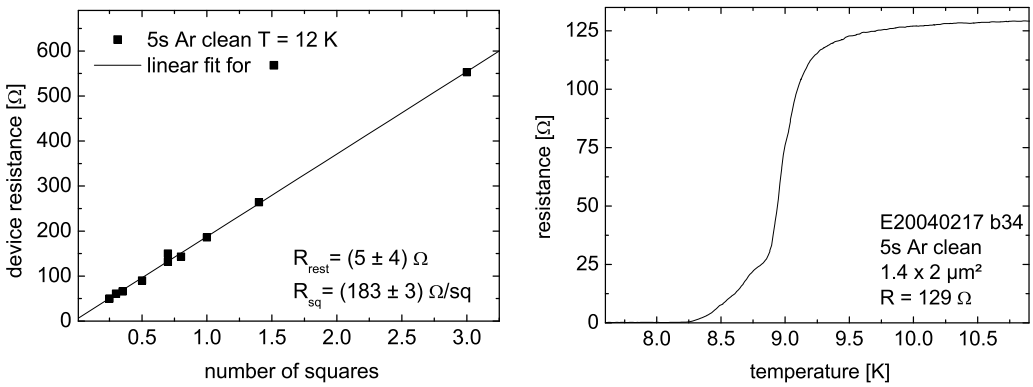

Fig. 4.7: *Plot representing the dependence of device resistance on bridge dimensions (length/width). Data were obtained from the corresponding R/T graphs at $T > T_c$. On the right the R/T graph of an exemplary test device is shown.*

impurities, which are preferentially removed by mechanical means.

The heat sinks consist of a 15 nm NbTiN / 50 nm Au bilayer. The dependence of the resistance on the number of squares for mixers of this batch is shown in fig. 4.7 on the left side. The interpolated resistance value for a zero-squares bolometer bridge is already much lower than the 31 Ω from the uncleaned device. Due to the soft Ar clean the contact resistance is lower as for the non-cleaned devices.

4.2.3 Medium Clean: 10 s Ar

The third batch of this test wafer has been cleaned with a soft (6 s, 3 W) O_2 clean followed by a 10 s, 6 W Ar sputter clean. The longer Ar-clean should remove oxide residues more efficiently.

The interpolated contact resistance in this batch is (3 $\pm$ 2)Ω as can be seen in fig. 4.8 on the left plot. The R/T plots (see fig. 4.8 on the right) show again several superconducting transitions. The assignment of superconducting transitions to the different parts of the device becomes increasingly difficult, since now the different regions are better coupled and influence each other.

When the critical temperature of the cleaned region is reached and this becomes normal conducting, a small part of the bridge becomes normalconducting too, as well as a small part of the heat sinks. The lowest transition is then composite of the heat sinks and a part of the bridge as well. This can be easily proven by showing that the resistive transition of the heat sinks +

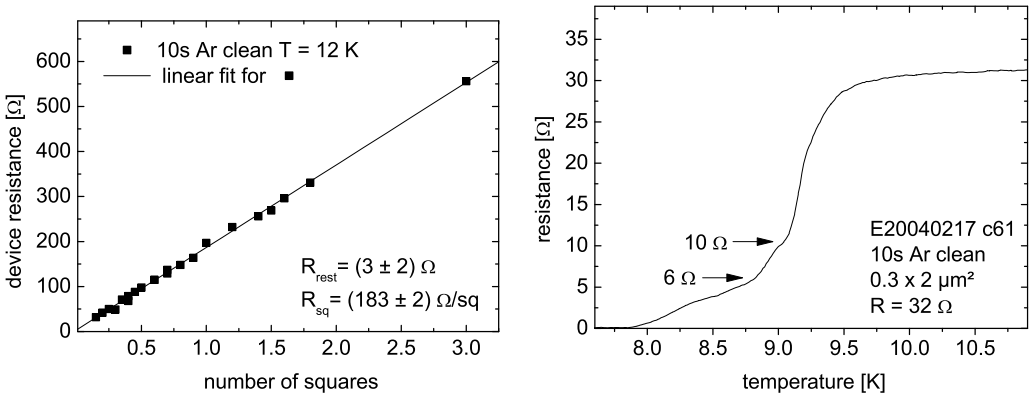

Fig. 4.8: *Left: Dependence of device resistance on bridge dimensions (length/width). Data were obtained from the corresponding R/T graphs. On the right R/T graph of an exemplary HEB test mixer.*

bridge (the lowest transition temperatures) depends on the bridge width. In this batch this cannot be shown because there are only two different widths.

4.2.4 A new batch: Width variations.

In this wafer the performed clean was the same for all mixers and consisted in a 6 s, 3 W O_2 clean and a 10 s, 6 W Ar clean. The heat sinks are made of a 15 nm NbTiN/50 nm Au bilayer. There were four different device lengths (300–600 nm) and three different square numbers, resulting in twelve different device widths. The R/T plots from three devices having the same length (300 nm) but different widths are shown in fig. 4.9 (left).

As discussed above, the resistance changes at the lowest transition temperatures are probably due to the heat sinks and partly to the adjacent parts of the bridge, which become normal conducting too. To confirm this, the resistance of the superconducting transitions with the lowest T_c is plotted on the right plot (fig. 4.9) against the bridge width. The reciprocal dependence on the bridge width means that at least a part of the resistance is bridge width dependent.

$$R = R_0 + R_\square \frac{l}{w}, \tag{4.1}$$

being R_0 the part of the resistance not arising at the bridge, l the bridge normal conducting length and w the bridge width. From the fit data we can

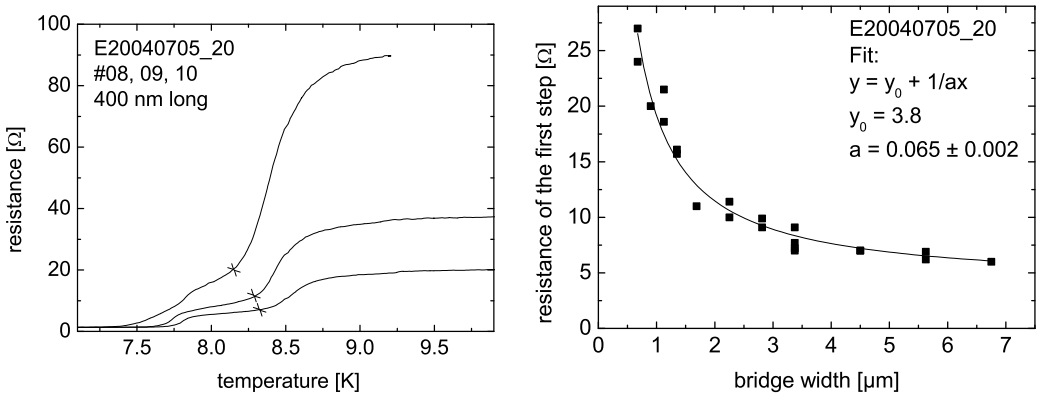

Fig. 4.9: *Left: Three devices of the same batch with the same bridge length but different bridge widths. Crosses mark the points at which the resistance of the heat sinks has been determined. Right: The resistance of the heat sinks plotted against the bridge width. A reciprocal function is used to fit the measured data.*

calculate the length of the bridge normal conducting region:

$$l = \frac{1}{R_{\square} \cdot 0.065} = (0.068 \pm 0.008) \quad \mu m, \tag{4.2}$$

using $R_{\square} = 225 \pm 25 \Omega/\square$. The resulting length $l = 68 \pm 8$ nm is for both sides together. Hence, the proximity effect reaches up to 30 to 40 nm into the bridge from each side. In this model, when the heat sinks become normal conducting, the sides of the bolometer bridge adjacent to the heat sinks become normal conducting too. It has been shown that there is a bridge width dependent part of the resistance, which seems to corroborate this model. Nevertheless, the length of 30–40 nm into the bridge seems to be too large regarding the coherence length of thin film NbTiN in the dirty limit $\xi \sim 2.4$ nm [79].

The proximity effect alone can therefore not account for the full resistance step. An additional source of resistance which has already been demonstrated for thin superconducting bridges at NS interfaces [45] can be the reason for the width-dependent resistance in HEBs.

Understanding the origin of resistance in the bolometer bridge can help to design better models of the mixing characteristics and therefore improve their design and RF performance.

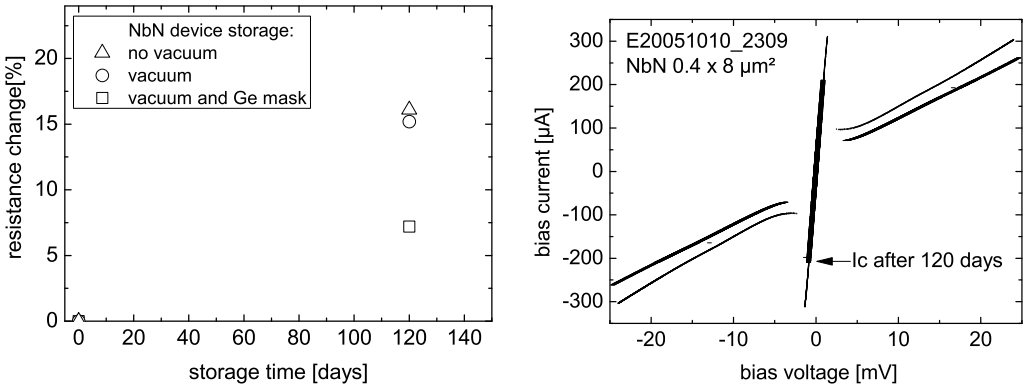

Fig. 4.10: *Left: Device resistance in % after fabrication and after four months under different storage conditions. Right: I/V plot of an exemplary device after fabrication (thin line) and after 120 days stored under atmospheric pressure (thick line).*

4.3 Shelf life of NbN Devices

A very important feature when considering HEB devices for their use in a telescope receiver is their shelf life. The thin superconducting layer can readily get oxidized in ambient conditions. Concerning this issue it actually makes a great difference if the bridge material is NbTiN or NbN. Most of the HEBs produced in this thesis use NbTiN as bridge material. Devices were partly stored under vacuum conditions and partly in clean room, but under non-vacuum conditions and still could be successfully tested even after eighteen months storage.

Devices made of NbN show already during processing a noticeable susceptibility to the oxidizing properties of air and specially of water. To protect the devices from oxygen, a protecting Ge layer has been evaporated over the bridge area. A NbN wafer has been only partly protected by Ge to enable comparison. The device resistance at helium temperature (using a bias current $I > I_c$) has been measured after fabrication and after four months storage time, both for devices stored in vacuum and under atmospheric pressure. The increase of the device resistance is a direct measure of the deterioration of the devices.

Surprisingly, devices stored in vacuum are hardly less deteriorated than devices stored under normal laboratory conditions. Devices protected with Ge show the smallest variation of parameters after four months storage. Other groups report similar success with SiO_x passivation layer [80].

Chapter 5

Membrane Preparation and Mixer Block Assembly

The main scope of this thesis was to produce HEB mixers operating at RF frequencies of 1.4 THz and 1.9 THz. At these frequencies quasi-optical mounts are normally used to couple the free space wave into the mixer device. Waveguides for wavelengths as short as 150 μ are much more difficult to manufacture. Not only the dimensions of the waveguide become tiny but also the wall roughness becomes increasingly important. The skin depth of the electric field on the conducting waveguide walls decreases with increasing frequency and small irregularities caused by the machining tool lead to signal power loss. A further complication is the waveguide probe: A considerable part of the signal can be coupled into the dielectric substrate instead into the microstrip lines. This leads to a drain of valuable power into the substrate which is therefore converted in heat without being mixed. To diminish the power dissipated in substrate modes, the substrate thickness must be considerably reduced. The normally used dielectric substrate is quartz and for RFs of 1.9 THz its thickness should be less than 10 μm.

Despite all these difficulties, waveguides have many advantages: Integration in an existing receiver system is much easier: The beam of a waveguide mixer with an appropriate horn antenna can be matched to the telescope beam much better and with less losses than a quasi-optic mixer (see chapter 1). Compact array designs are possible and many more devices can be manufactured on a wafer since there is no antenna structure needing extra space.

The requirements on waveguide fabrication have been mastered in the mechanical workshop at KOSMA: Copper mixer blocks with waveguide lateral dimensions smaller than 60 μm have been successfully machined. A newly

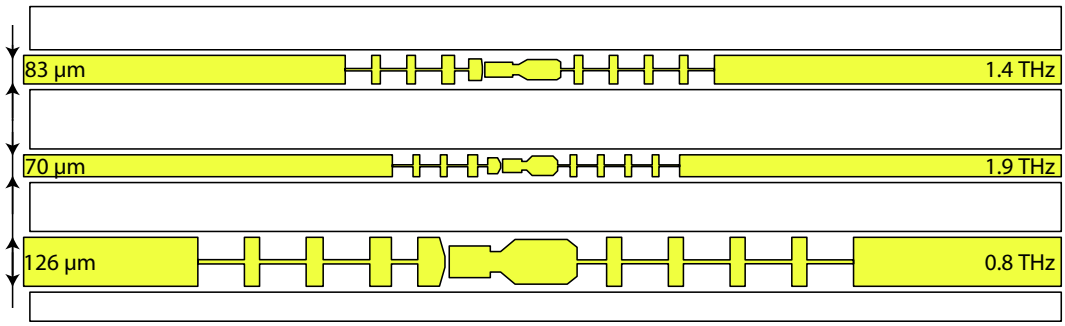

Fig. 5.1: *Illustration of three mixers for 1.4 THz, 1.9 THz and 0.8 THz.*

introduced Inductively Coupled Plasma (ICP) etch facility will enable us to etch even smaller waveguides in silicon.

Reducing the quartz substrate thickness to 10 μm or less is a very difficult task because the substrate becomes very brittle. Instead of a Si substrate a 2 μm low stress Si_3N_4 membrane produced at [55] has been used. The membrane is deposited on a Si carrier wafer which is etched away after device fabrication and DC-characterization.

In the following sections the fabrication steps which append to fabrication and DC measurements will be presented. Also the integration of the devices into a mixer block will be described. The work in this thesis bases upon the work published in [27]. Therefore, the explanation of the different steps will often relate to [27] and only explain in detail the aspects which have been optimized during this thesis.

5.1 Si_3N_4-Etch Step

The silicon nitride membrane extends over the whole wafer and must be cut into strips delimiting the different devices. This step is performed *previous* to the DC measurements since lithography becomes complicated when the wafer has already been diced into small pieces.

The width of the strips depends on the RF frequency as can be seen on fig. 5.1 and is defined by uv-lithography. These strips are the membrane beams which will span freestanding through the substrate channel and across the RF waveguide channel (see fig. 5.9).

Si_3N_4 is inert to most chemicals [81]. The Si_3N_4 membrane is cut with a Reactive Ion Etch (RIE) step using a fluor based process gas. The highly aggressive F^+ ions chemically attack the silicon nitride and build volatile com-

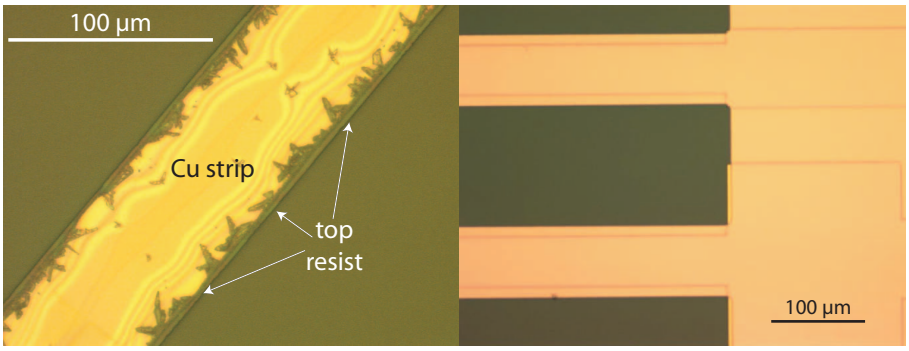

Fig. 5.2: *Microscope photographs of HEB strips covered by a copper mask, which is being patterned. The picture on the left shows isotropic etch. The picture on the right shows reliable results after process optimization. Note the much better definition. The different colour has to do with the microscope used and not with the new process.*

pounds which are pumped out by a turbo pump. The process gas from the original recipe, NF_3 (6 scm^3, 100 μbar, 80 V), has been exchanged for safety reasons by a mix of SF_6 (12 scm^3) and Ar (2 scm^3), also operating at 100 μbar and 80 V. Additional cooling breaks have been introduced (every minute instead of every two minutes). Keeping the wafer cool is beneficial for the sensitive bridge layer but reduces the chemical activity and increases the etching time. The etch time increased from 12 min to 20 min. To protect the HEBs from etching, a mask must be lithographed which can withstand the long F^+ ion etch and be removable after the RIE step without damaging the devices. Besides, the existing topography on the wafer demands a mask which covers the edges efficiently. A UV-resist is spun over the wafer which can cover the existing structures sufficiently. A copper layer (180 nm) is evaporated[1] on top of the resist. A second resist is used on top to pattern the copper layer (see fig. 5.3). The copper is patterned by etching with a filtered and highly thinned $Fe(III)Cl_2$ etch solution.

The wet etch is very isotropic and the copper beneath the resist was strongly damaged as can be seen in fig. 5.2 on the left. To solve this problem a new positive resist was tested. The UV-resist AZ7212 was substituted by the UV-resist MIR701. Instead of using an IR-oven to bake the resist as mentioned in [27], the resist layers were baked on the hot plate at 90 °C for 90 s. An O_2 clean on the evaporated copper layer previous to the second resist has turned out to be superfluous and has been eliminated too. The new recipe to pattern the copper is much more reliable and copper underetch

[1] Sputtering would expose the resist, since sputtering takes place in a plasma discharge.

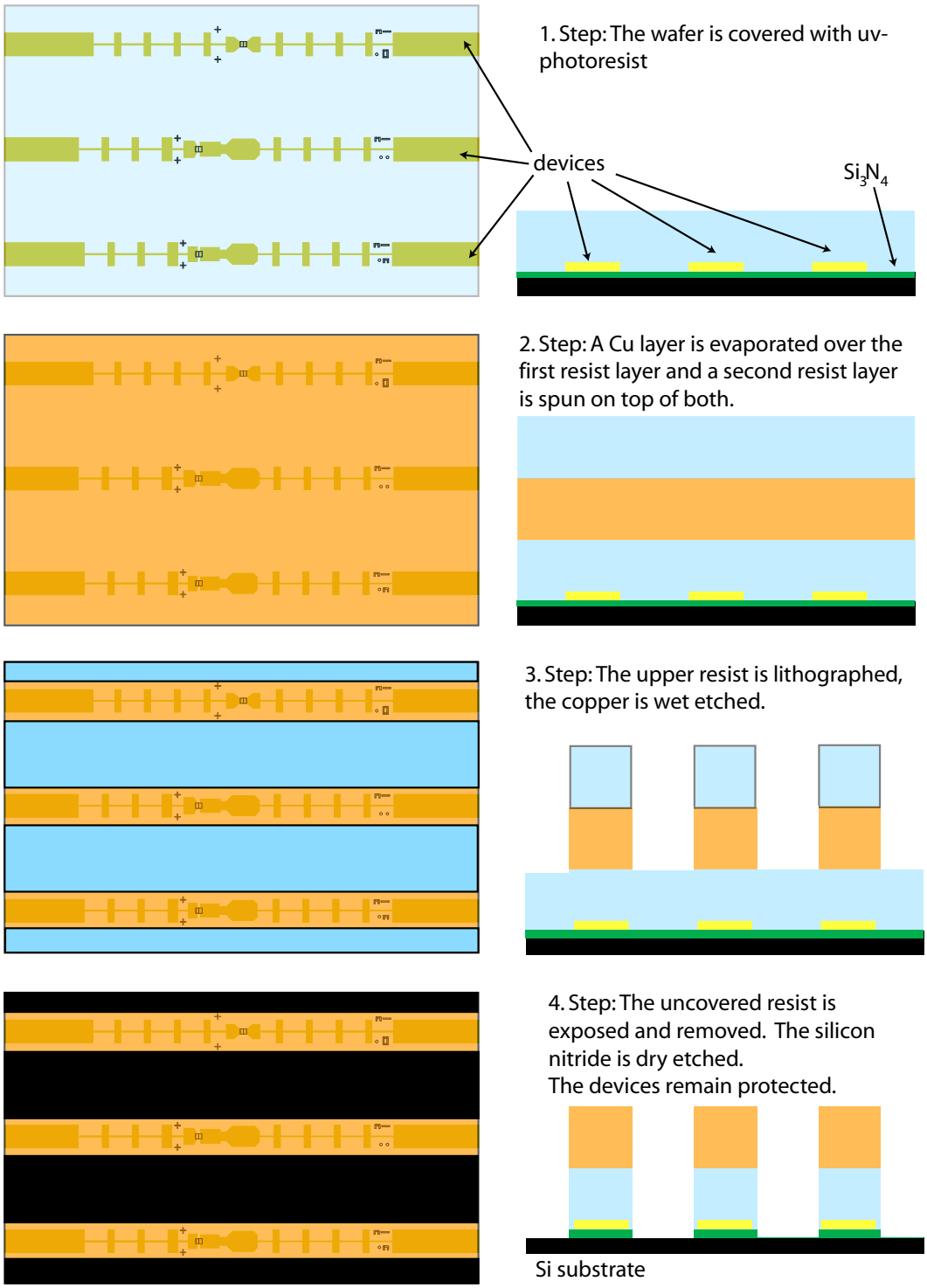

Fig. 5.3: *Schematic representation of the process sequence to pattern the copper mask and to etch the silicon nitride layer. Left pictures: Top view. Right pictures: Cross section.*

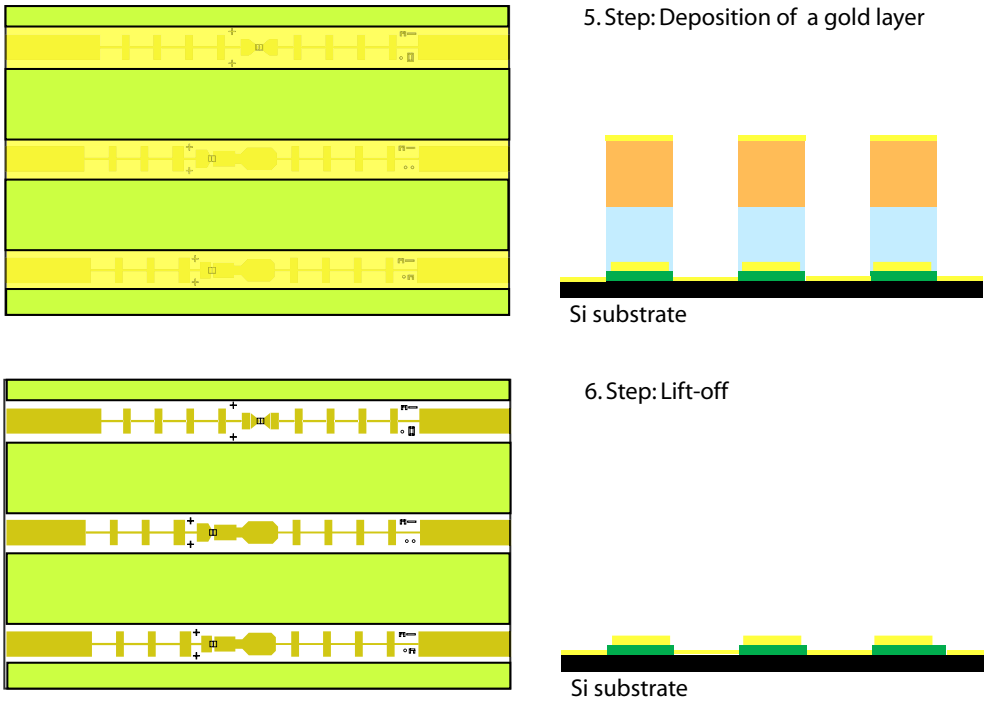

Fig. 5.4: *Schematic representation of the self-aligned lift-off process sequence to deposit a gold layer on the bare silicon. Left pictures: Top view. Right pictures: Cross section.*

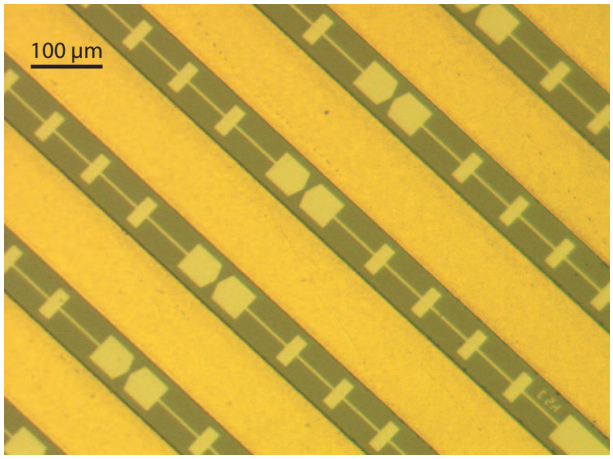

Fig. 5.5: *Microscope picture of the device strips. The Si_3N_4 membrane between the strips has been etched away and substituted by 500 nm sputtered gold.*

problems have not been observed (see fig. 5.2, right side).

In the future, this complicated mask sandwich could be eventually substituted by a newly produced uv-resist (AZ9260) which is 5–6 μm thick and RIE-etch resistant. After cutting the Si_3N_4 membrane in strips a 500 nm gold layer is deposited to cover the blank Si area between the strips using the same photoresist-copper mask for lift-off (self-aligned lift-off). This gold film seals the cut membrane strips and protects the HEBs when the Si carrier substrate is removed by the wet etch solution when it breaks through from the backside.

Lift-off in hot aceton delivers the result shown in fig. 5.5.

5.2 Silicon etch

After DC-testing, the wafer pieces holding the selected devices are prepared for the etch step releasing the membranes from the Si carrier substrate. The devices are on the front side of the membrane and have to be protected from the etch solution in the backside to avoid deterioration or even total loss at this last microfabrication step.

For the DC measurements the devices are electrically bonded to a circuit board. The bond wires are removed but remains (wire butts) on the bond pads must be diced away, since the wafer piece must be completely flat. The devices are still connected by the common ground line. The wafer is then glued using w-wax [82] with the HEBs facing to an auxiliary glass wafer.

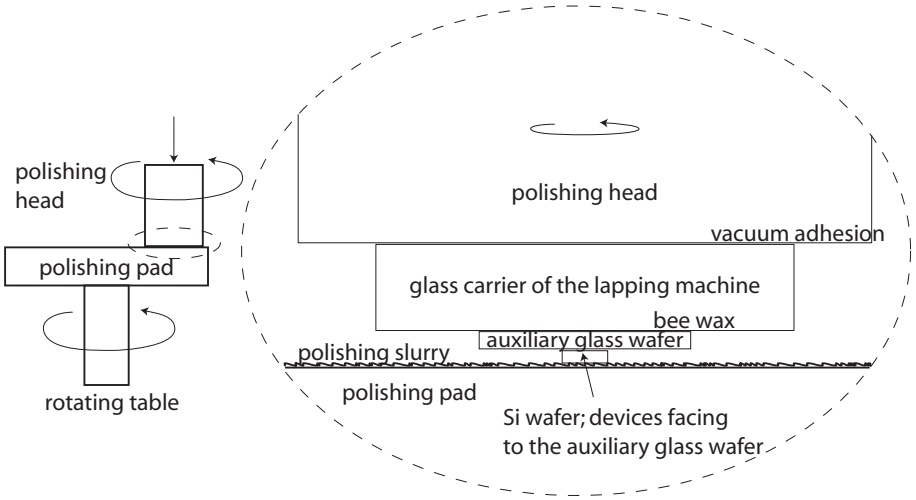

Fig. 5.6: *Schematic side view of the polishing process. A close-up of the polishing interface is shown on the right. The Si wafer is glued to an auxiliary wafer with the devices facing towards it. During the polishing process the wafer sandwich is pressed by the rotating polishing head against the likewise rotating polishing pad.*

The levelling tolerance must be smaller than 5 μm. The wafer/auxiliary-wafer sandwich is glued with bee wax onto the glass carrier of the polishing machine. In difference to the previous step, standard bee wax with a considerably lower melting point is used here. This will enable the easy removal of the wafer sandwich from the glass carrier after polishing. The silicon wafer is polished in two slurry steps down to a thickness of 70 μm. The final thickness leaves a bit of tolerance as the silicon is going to be fully removed during the next step. The silicon is etched using an etch solution containing

- three volume parts of acetic acid (CH_3COOH 100% vol.),
- five volume parts of nitric acid (HNO_3 65% vol.),
- and three volume parts fluoric acid (HF 48% vol.).

The concentration ratio can be varied to control the rate and the etch fashion, e. g. isotropy and surface roughness. This ratio 3:5:3 has an etch rate of $\approx$ 25 μm/min in average: The etch rate in the outer parts is slightly faster than for the silicon in the center. In this way the probability of damaging the HEB devices is reduced because they are located in the center part of the wafer. The etch solution stops at the silicon nitride membrane and at the gold layer, but the etchant can still diffuse to the HEBs via pin-holes in the gold

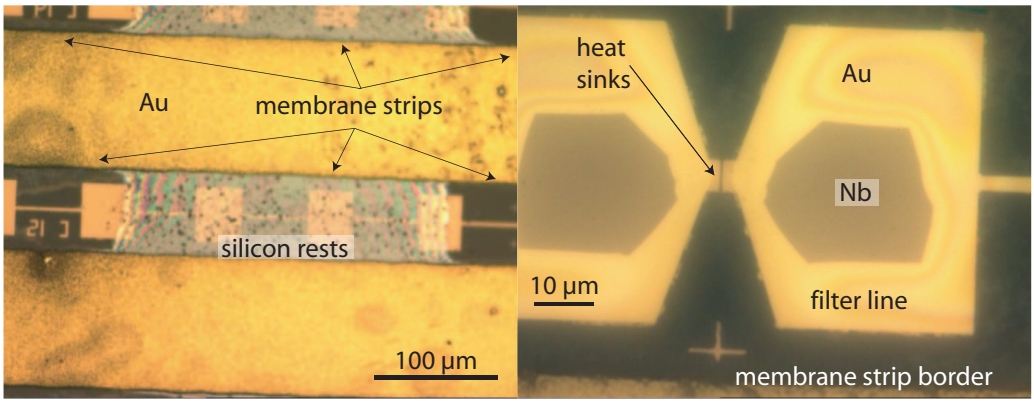

Fig. 5.7: *The microscope picture on the left shows two membrane strips from the back side after wet etch which still have some thin silicon rests. The microscope picture on the right shows a close up of the HEB area of a membrane strip from the backside which has been totally damaged by the etch solution. The Nb of the filter lines has been etched away but for a small region in the center. The bridge layer underneath the heat sinks has been completely removed.*

layer or at the boundary between the silicon nitride and the gold. The w-wax can slow down the F^+ ions a bit, but generally the wafer cannot be kept too long in contact with the etch solution. A gradient in the wafer thickness can be originated by non levelled lapping process. If the etch time gradient in a wafer is too big, due to a thickness slope or to the etch solution behaviour, some parts of the wafer are overetched while others still show silicon rests (see fig. 5.7). After successful etching the wafer is rinsed in water for at least ten minutes. This cleans the wafer from remaining F^+ ions which would damage the devices even after the wafer is no more dipped in the etch solution.

The gold layer between the membrane strips is removed in a I/IK aqueous gold etch solution. The w-wax protects the devices during this etch step. Finally, the w-wax can be dissolved and the membrane strips —connected by the ground line— are released from the auxiliary glass wafer (see fig. 5.8).

The membrane strips are still connected through their common ground line forming a comb which can be easier handled as single membrane strips. The Si_3N_4 membrane material is relatively strong. It can be bent to certain angles. In our experiments, the intrinsic stress of the used material was so low, that the membrane does not bend when the bulk wafer has been totally removed.

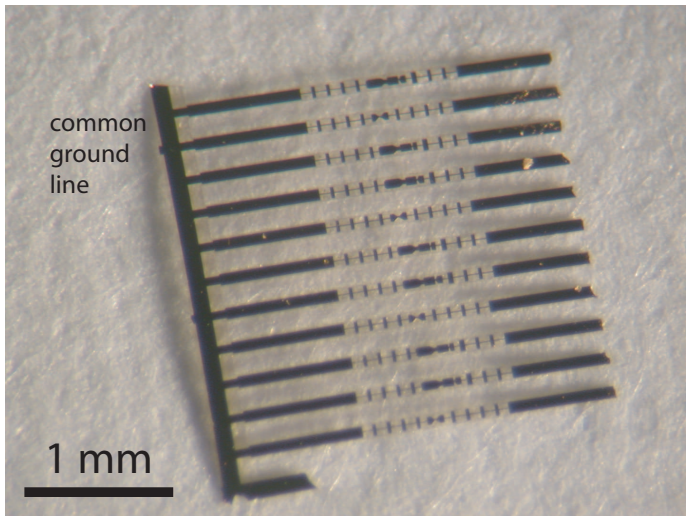

Fig. 5.8: *Microscope picture of eleven devices on membrane strips. They are connected (left side) by the common ground line. Handling is easier as for single membrane strips.*

5.3 Assembly into the waveguide mount

The freestanding membrane must be span over a substrate channel at a definite height. A single membrane strip is attached to a frame as shown in picture 5.9. The frame is glued to a copper waveguide mount. The membrane spans freestanding in the substrate channel with the waveguide probe suspended at the correct height in the RF waveguide backshort. The membrane device is electrically contacted with wire bonds. The frame and the devices are fabricated separately. There are approaches which fabricate the membrane devices and the supporting frames on the same wafer as for instance [84, 85]. This is connected with a loss of wafer state for devices and an additional deterioration risk for the devices as the frame fabrication is done. Separating the fabrication of both subsystems brings also a certain process flexibility, since fabrication of one subsystem can be optimized without taking into a account the possible disadvantages for the other subsystem. Otherwise the mounting onto the waveguide mount is more involved.

The silicon frames are patterned using standard microfabrication techniques. The silicon is anisotropically etched using a TMAH solution at 80 °C. The frames are lapped-thinned to the desired height (usually 80 μm) and have two gold pads on opposite sides.

After fabrication the frames are selected under the microscope according to their height, which can vary a little depending on the position on the frame

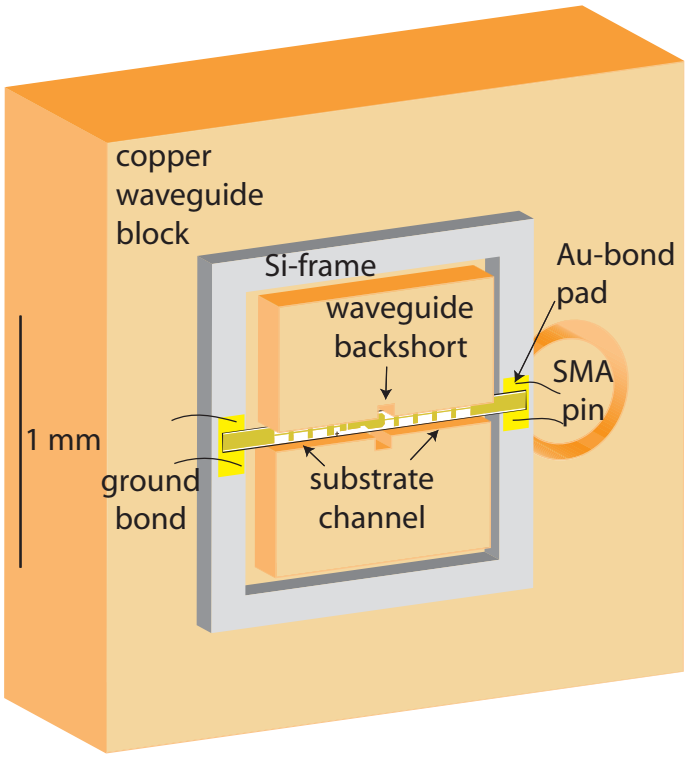

Fig. 5.9: *Schematic representation of the membrane/frame integration into a copper waveguide mount. The membrane is attached to the silicon frame and span freestanding in the substrate channel. It does not lay on its bottom. The device is facing to the frame and is electrically bonded through the Au bond pads to ground and to a SMA pin.*

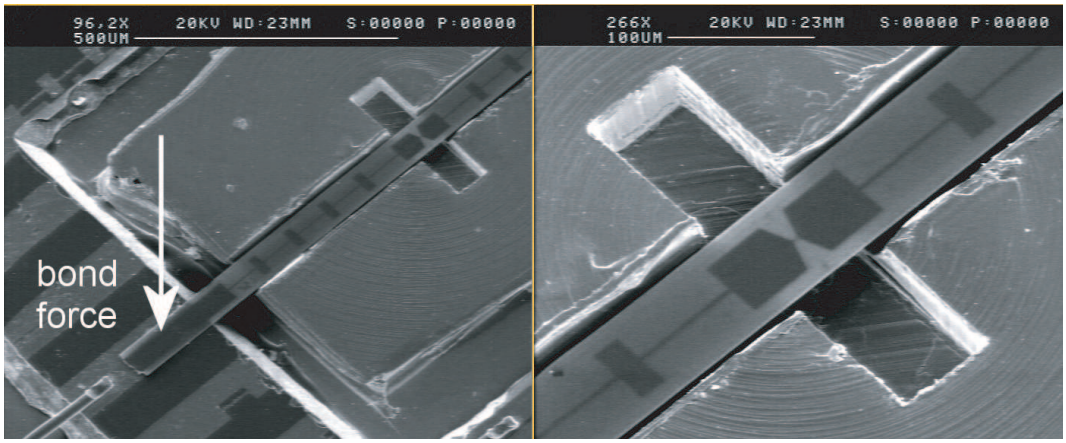

Fig. 5.10: *Scan Electron Microscope (SEM) picture of a device already integrated in the waveguide block. This picture has been taken from [83].*

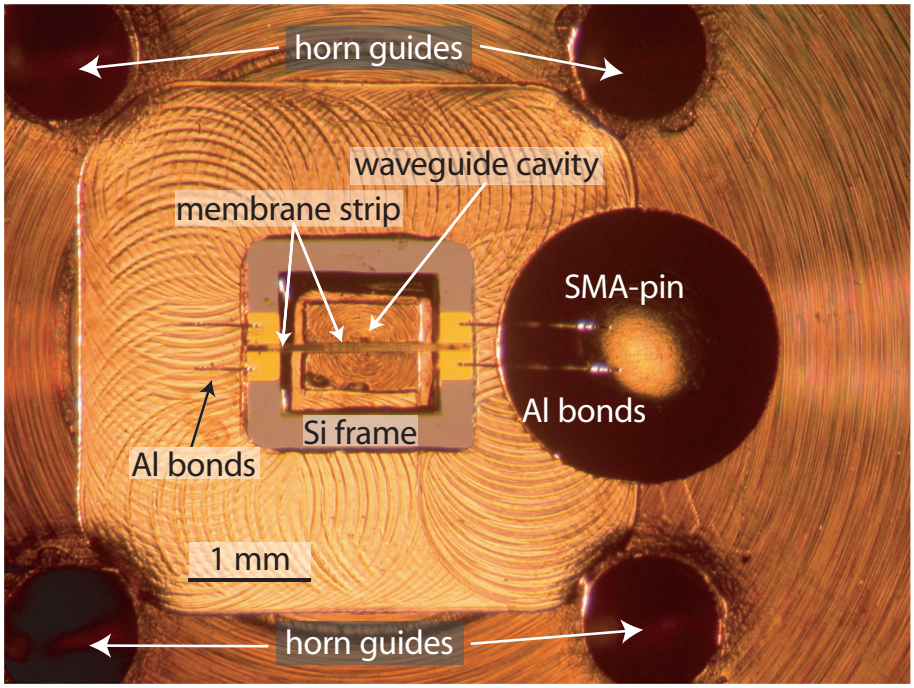

Fig. 5.11: *Microscope picture. Top view of a waveguide block holding a 1.4 THz membrane HEB mixer*

wafer. The selected frame is cleaned and carefully glued on the waveguide mount with hot w-wax. The frame must be pressed a bit down to ensure that no air bubbles remain between the frame and the copper. Air bubbles can lead to detachment of the frame when the mixer is rapidly cooled down ($\Delta T \approx 265$ K) in vacuum.

A cooling cycling test has been performed under vacuum conditions for two mixers with frames glued to the waveguide blocks using two different wax makes: w-wax and w100-wax. The w100-wax has a lower melting point and is therefore softer. Both mixers were evacuated in a cryogenic container, which was subsequently cooled down to liquid nitrogen temperature and warmed up in vacuum. Even after 30 cycles no deterioration of any of both wax types could be observed.

The membrane strip comb as shown in fig. 5.8 can be picked up from the storage box with a single-hair ESD[2] brush and be placed on the waveguide mount-frame system. The comb is carefully pushed until the desired strip falls

[2]ElectroStatic Discharge (ESD) tools are grounded through a high resistance (1 MΩ) to avoid high current discharges originating at isolating surfaces which could damage discharge-sensitive devices. As soon as the HEBs are diced in individual devices for the DC-measurements great care must be taken to protect the HEB devices from ESD.

into the substrate channel with the metallization side looking downwards. The strip is broken off the rest of the comb, which is picked up by the brush hair and stored again.

The next step is to attach the membrane strip with the desired HEB device to the gold pads of the silicon frame. To do this, a special bonding needle presses the membrane (on the back side) against the gold pad and emits a short ultrasonic pulse which bonds the gold on the filter lines with the gold on the frame pads. This is repeated for the other side. Doing this, the membrane strip is attached mechanically and (electrically) to the silicon frame.

Until now the alignment of the probe in the waveguide must not necessarily be done accurately. The copper mount can be heated to $\approx 85\ ^{\circ}C$ to re-melt the w-wax allowing the frame to be carefully pushed from the side to align the waveguide probe with the waveguide backshort. To move the frame a microassembly stage [86] with piezo-driven nanomotors is used. The waveguide probe can be aligned very precisely in the waveguide.

When the w-wax is hardened, the waveguide mount is ready for bonding the electrical connections. With this step the fabrication of the waveguide environment and the assembly of the device is almost finished.

5.3.1 Horn alignment

After device contacting a waveguide horn is screwed to the backshort block. The horn has guiding pins at a definite distance from the waveguide channel which can be inserted into tight guiding boreholes on the waveguide block. For frequencies below 1 THz this method has proven to be accurate enough. For higher frequencies the waveguide dimensions are much smaller and a misplacement of only 10 μm is equivalent to a mismatch over 17% of the waveguide width. The horn mounts for higher frequencies do not have guiding pins but are aligned using a dedicated tool. The horn mount is placed on the backshort block. The horn can be shifted in both directions parallel to the interface plane using two micrometer screws. The alignment can be optically controlled while shifting the horn as shown in fig. 5.12. When the horn waveguide matches the backshort both mounts are tight screwed. The mismatch with this method is low enough (<3 μm) for THz frequencies.

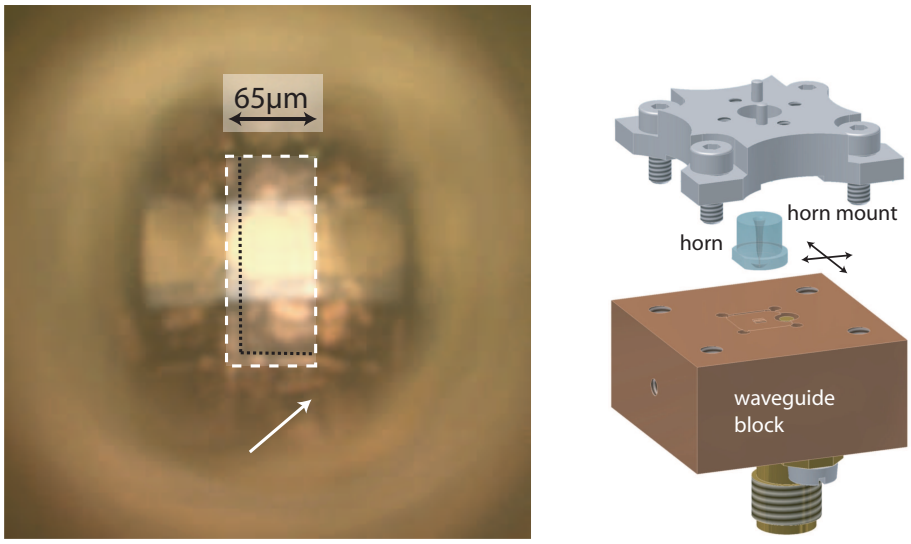

Fig. 5.12: *Microscope picture of the waveguide probe and the backshort taken while the horn was not aligned to the backshort. The clear dashed line marks the borders of the horn waveguide, while the dark dots mark the part of the backshort which is visible. The horn must be shifted in the arrow direction to match the backshort. On the right a simplified drawing of the waveguide block with the waveguide backshort and the horn.*

Chapter 6

RF Measurements

In this chapter three types of measurements are discussed:

The receiver noise temperature is usually measured to characterize the mixer. From the receiver noise temperature, the mixer noise temperature and mixer gain can be determined. The IF bandwidth can be also estimated from these data if the receiver noise temperature is measured as a function of IF.

A Fourier transform spectrometer is used to measure the power response of the bolometer as a function of RF frequency. This measurement checks the RF design and the assembly.

Stability measurements are performed to characterize the maximum integration time for real observations.

6.1 Receiver noise temperature

In this section the measurements of the receiver noise temperature T_{rec} are considered. To measure T_{rec} the standard Y method has been used. The mixer noise T_{mix} can be calculated using this data and the noise temperature of the IF components at the output side of the mixer and the optics characteristics at the input side of the mixer.

The IF noise bandwidth is defined as the IF at which the mixer noise has increased by a factor of two from the minimum noise temperature (at the lowest measurable IF). Unfortunately the IF bandwidth of the used IF amplifiers (band pass from 1.2 – 1.8 GHz) was smaller than that of the mixer and consequently the noise bandwidth cannot be determined from the measurements.

6.1.1 Basic theory

In a Y-factor measurement, two noise sources (hot and cold loads at 300 K and 77 K respectively) are connected subsequently to the receiver input and the ratio Y of the receiver output powers $P_{out,hot}$, $P_{out,cold}$ is measured:

$$Y \equiv \frac{P_{out,hot}}{P_{out,cold}} = \frac{G_{rec} \cdot (P_{rec} + P_{in,hot})}{G_{rec} \cdot (P_{rec} + P_{in,cold})}, \tag{6.1}$$

P_{rec} being the input noise power of the receiver in the considered bandwidth B ($B \ll \nu$, ν is the RF at which the mixer operates), $P_{in,hot}$ and $P_{in,cold}$ the incident power on the receiver in this bandwidth respectively from a hot and a cold load, G_{rec} the receiver gain and $P_{out,hot}$ and $P_{out,cold}$ the measured receiver output power at the IF for the hot and cold loads. The loads are assumed to be blackbody radiators at their well known temperatures (i. e. room temperature and liquid nitrogen temperature).

The input noise power can be deduced by inverting (6.1) into:

$$P_{rec} = \frac{P_{in,hot} - Y P_{in,cold}}{Y - 1}. \tag{6.2}$$

The power radiated from the loads $P_{in,hot}$ and $P_{in,cold}$ can be calculated using the Planck law:

$$P_{Planck} = \frac{h\nu B}{e^{\frac{h\nu}{kT}} - 1}, \tag{6.3}$$

ν being the measured RF, k the Boltzmann constant and T the physical temperature of the hot or cold load.

For submillimeter radiation $h\nu \ll k_b T$ (not for THz radiation) and by Taylor-expanding the exponential factor[1] the Planck law is consequently reduced in first order to the linear Rayleigh-Jeans law:

$$\lim_{kT \gg h\nu} P_{Planck} \rightarrow P_{R-J} = kBT. \tag{6.4}$$

The receiver noise power P_{rec} (equation 6.2) contributed by the receiver can be expressed as a temperature, which is defined (as in equation 6.4) as

$$T_{rec} = \frac{P_{rec}}{kB}. \tag{6.5}$$

[1] $\exp(h\nu/k_b T) \approx 1 + h\nu/k_b/T$

Using (6.2), (6.4) and (6.5), T_{rec} is can be expressed by:

$$T_{rec} = \frac{T^*_{hot} - Y T^*_{cold}}{Y - 1}. \tag{6.6}$$

T^*_{hot} and T^*_{cold} being the physical temperatures T_{hot} and T_{cold} of the loads (in the Rayleigh-Jeans limit). For higher frequencies, at which the condition $h\nu \ll kT$ is not fulfilled, another effective temperature must be used:

$$T^{Planck} = T \left[\frac{\frac{h\nu}{kT}}{e^{\frac{h\nu}{kT}} - 1} \right]. \tag{6.7}$$

For heterodyne receivers with very low receiver noise (i. e. using SIS-mixers), the unavoidable quantum noise is regarded separately and not as part of the receiver noise. This is done by including the zero point fluctuation into the calculation of the power from the loads [87]. The used dissipation-fluctuation theorem or generalized Nyquist theorem of Callen & Welton [88] is given by:

$$P_{C\&W} = \frac{h\nu B}{e^{\frac{h\nu}{kT}} - 1} + \frac{h\nu B}{2}, \tag{6.8}$$

which is simply the Planck formula with an additional half photon per Hz. To obtain T_{rec} using the Callen & Welton law, the equivalent load temperatures must be calculated using

$$T^{C\&W} = T \left[\frac{\frac{h\nu}{kT}}{e^{\frac{h\nu}{kT}} - 1} \right] + \frac{h\nu}{2k} = \frac{h\nu}{2k} \coth\left(\frac{h\nu}{2kT} \right). \tag{6.9}$$

Calculating the load input power with (6.9) is consistent with the quantum mixer theory for SIS junctions [89].

In fig. 6.1 the calculated receiver noise is shown using the Rayleigh-Jeans (R-J), Planck and Callen & Welton (C&W) laws to calculate the equivalent load temperatures for the three different frequencies at which the considered mixers operate. The differences between the curves for R-J and Planck as well as between R-J and C&W are also displayed. Note that the difference becomes larger with increasing RF and decreasing the Y-factor.

For the 0.8 THz receiver the difference obtained in the receiver noise temperature by using the C&W or the R-J model is so small ($\sim$ 6 K)[2] that the much simpler R-J approximation can be used here for calculations. For

[2] Regarding the obtained absolute value of 600 K the error is of only 1%

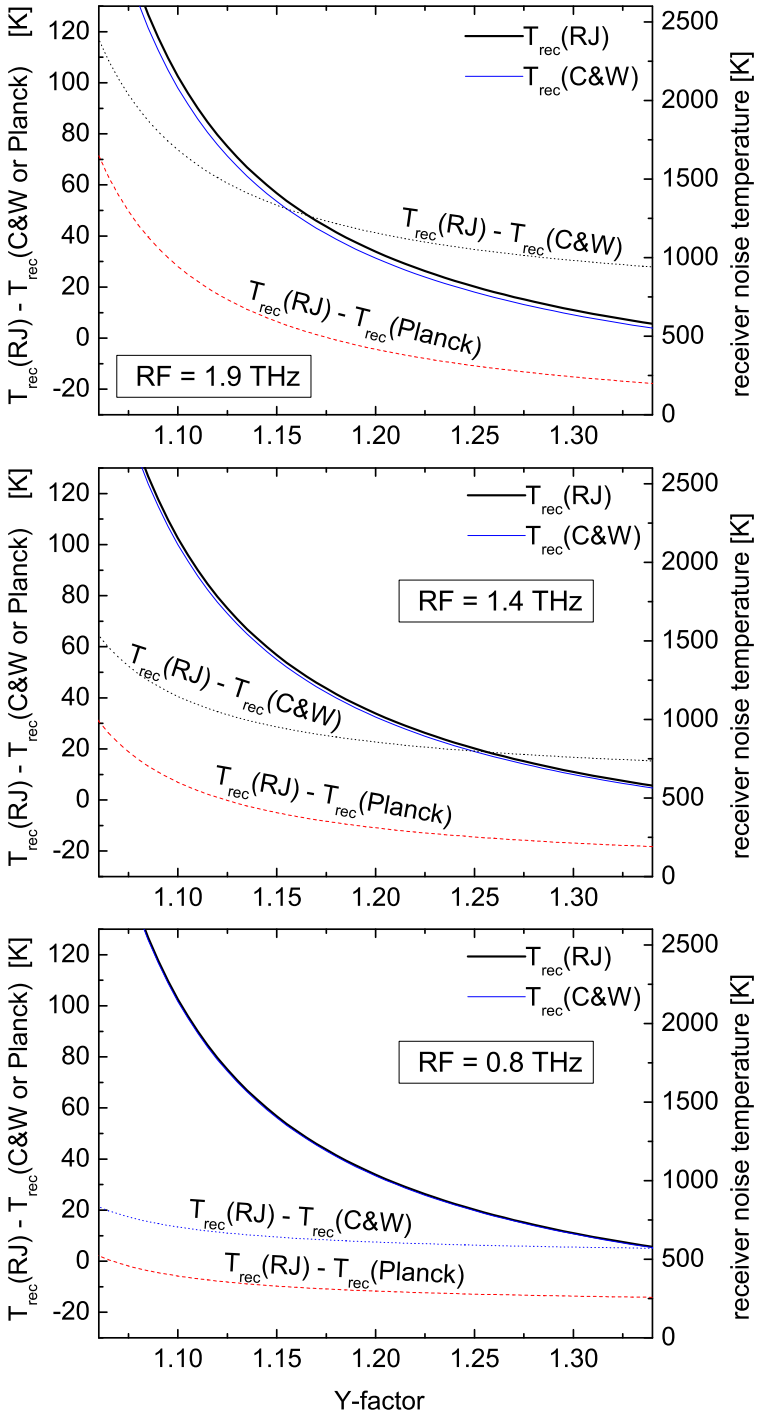

Fig. 6.1: *Receiver noise temperature (right-hand scale) as a function of Y-factor for three receivers at different frequencies (1.9, 1.4 and 0.8 THz) measured with T_{hot} = 300 K and T_{cold} = 77 K. The Rayleigh-Jeans curve (thick line) is obtained when the hot and cold load noise temperatures are equal to their physical temperatures. The Callen & Welton curve is obtained using the equation (6.9) for the hot and cold load noise temperatures. The difference between the Rayleigh-Jeans and Callen & Welton (Planck) curve is shown by the dotted (dashed) line.*

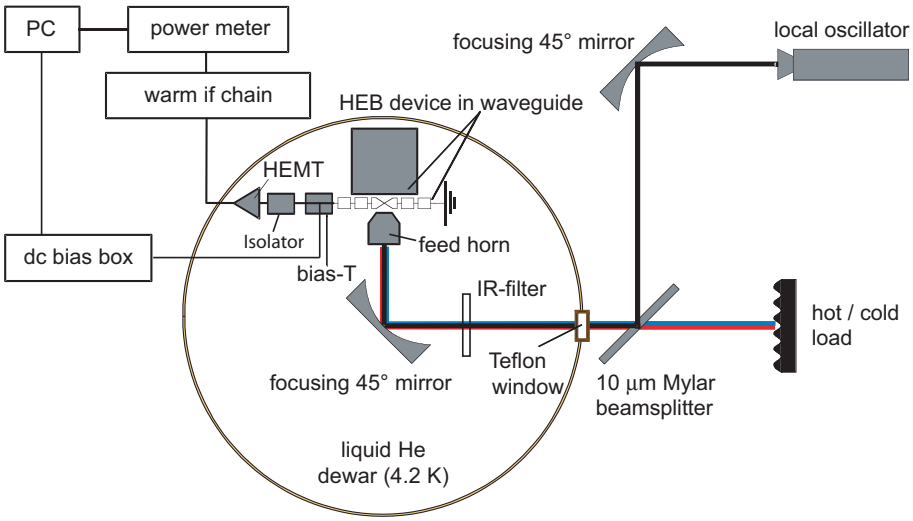

Fig. 6.2: *Setup for heterodyne measurements, adapted from [19]. At 1.4 THz and 1.9 THz a Martin Puppet Interferometer is used instead as diplexer.*

SIS-based receivers with much lower noise temperatures the C&W law is used beyond some hundred GHz (for instance [90, 91]). For the 1.4 THz and 1.9 THz receivers presented here, the C&W formula has been used to compute the equivalent load temperatures. The effect of using the C&W model is the largest for the 1.9 THz receiver since the Y-factor is there also smaller ($Y \approx 1.11$) than for the 1.4 THz ($Y \approx 1.14$) or 0.8 THz ($Y \approx 1.29$) receivers.

6.1.2 Setup

In our heterodyne test receiver the signal from the Local Oscillator (LO) is injected using a 10 μm beam splitter at 0.8 THz or a Martin Puplett Interferometer (MPI) at 1.4 THz and 1.9 THz to diplex the load signal with the LO signal.

To perform the heterodyne measurements, the mixer must be placed on the helium stage of a liquid cryostat (dewar), which is evacuated and cooled down to 4.3 K. The beam enters the dewar through a teflon window and two IR filters (Zitex G108 [92]) at the 77 K and Helium stages. In the dewar the beam is collimated into the waveguide horn using a focusing mirror. For each frequency a different distance from the horn aperture to the mirror is needed. This distance is fixed by the mixer sliding carriage (see fig. 6.3 and 6.4). For each frequency a dedicated sliding carriage has been produced. In the test

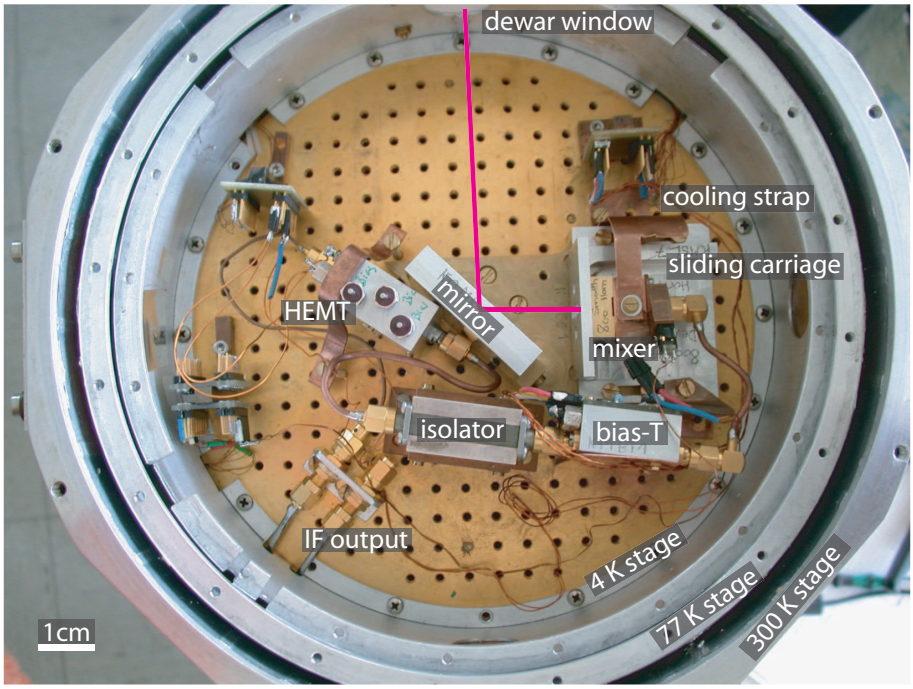

Fig. 6.3: *Top view photograph of the open 4 K stage of the cryostat. The optical path is marked by a red line.*

dewar the same mirror has been used for all frequencies and only the distance has been adapted to optimize the coupling to the different waveguide horns. The transmission of the used optical components at different frequencies are listed in table 6.1.

The passive electronic components (bias-T, isolator) and the first Low-Noise Amplifier (LNA) are also placed on the cold stage to avoid thermal noise contributions. The IF signal generated at the HEB is transported using SMA connections and semirigid steel coaxial cables to the bias T, where the DC bias and the IF signal are separated. The DC bias lines are protected against high voltage pulses which can, for example, be caused by electrostatic discharge (ESD). These voltage pulses are mitigated by a RC-pass at the bias-T since they otherwise damage the HEBs. The bias electronics are connected to a computer controllable DC-Bias-Box, where the DC bias voltage and current can be set and monitored. In the bias T the IF is capacitively coupled to the isolator. The isolator absorbs the power which is reflected at the amplifier input and would otherwise cause undesired standing waves between the mixer and the amplifier. The isolator used for this setup limits the IF bandwidth to 1.2–1.7 GHz. Some measurements have been performed without isolator

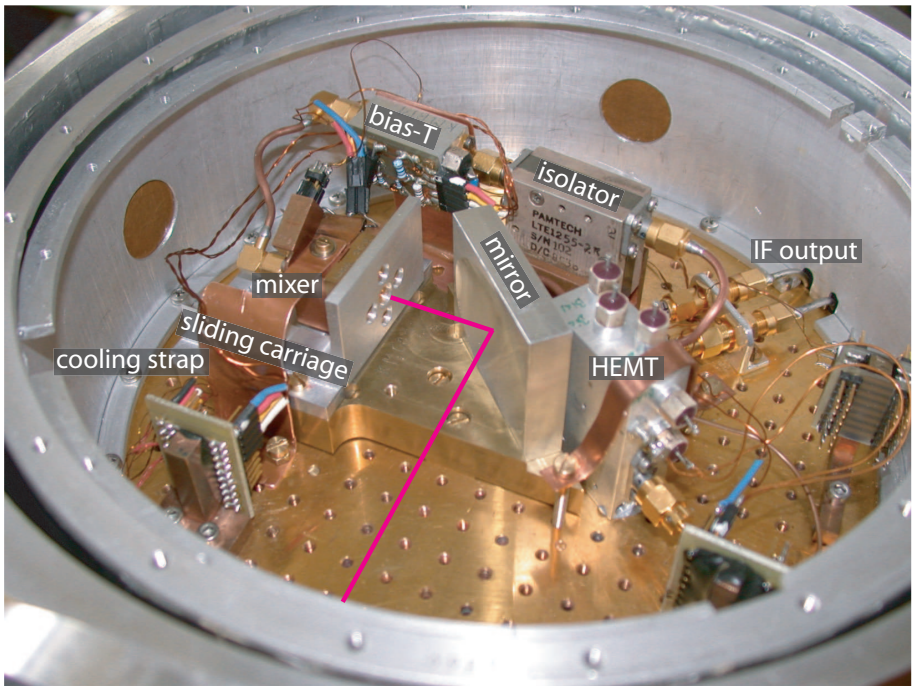

Fig. 6.4: *Side view of the open 4 K stage of the cryostat. The optical path is marked by a red line.*

	0.8 THz	1.4 THz	1.9 THz
Diplexer	0.95	0.96	0.71
Teflon 0.5 mm at 300 K	0.90	0.90	0.82
Zitex G108 2 layers at 77 K	0.94	0.80	0.94
Zitex G108 1 layer at 4 K	0.96	0.95	0.97
Mirror	0.96	0.94	0.90
Horn antenna	0.96	0.95	0.93
Total	0.71	0.59	0.44

Tab. 6.1: *Gain values for the test dewar optics at three frequencies. Measurements by G. Schmidt and A. Wagner using a Fourier Transform Spectrometer (FTS) at KOSMA. The values for the mirror and for the horn antenna are estimated. The diplexer at 0.8 THz and 1.9 THz is a 10 μm beam splitter. The diplexer at 1.4 THz was a Martin Puplett Interferometer.*

for this reason. The IF signal is amplified using a cryogenic High Electron Mobility Transistor (HEMT). Unfortunately many measurements at 0.8 THz have been performed using a HEMT with increasing noise over the measured IF band (7 K at 1.2 GHz rises to 15 K at 1.5 GHz, see fig. 6.6). The measurements performed at 1.4 THz and 1.9 THz have used a new HEMT which is low-noise for 1.0–2.0 GHz.

The following amplification stages can already be placed outside the dewar under non-cryogenic conditions. A tunable IF filter (bandwidth 80 MHz)allows to choose a IF detection frequency at which the noise temperature and the conversion gain are to be measured. The output power is measured by a calibrated power meter.

6.1.3 Local Oscillators

The Local Oscillator (LO) is mixed with the input RF to produce the difference or intermediate frequency (IF). The LO power is much larger than the RF signal power and causes an increase in the temperature of the HEB. This has a clearly visible consequence on the DC I/V curve of the HEB (the HEB is *pumped*). The LO power needed to pump the HEB depends directly on the bridge volume, since it is brought to the operation temperature by the dissipated LO power to serve as a power-law mixer. A larger bridge volume means also a larger amount of Cooper pairs and often a higher critical temperature too (see chapter 4).

A LO source up to $\approx$ 1 THz (and newly also up to 1.9 THz [93]) is the solid state LO based on a Gunn diode followed by whisker contacted Schottky frequency multipliers. Another kind of solid state LO, which was used for the 1.4 THz measurements, consists of a frequency tunable YIG-oscillator at around 19 GHz followed by a frequency multiplier/amplifier chain ($\times$ 2, power amplifier, $\times$ 4 $\times$ 3 $\times$ 3).

For frequencies beyond 1 THz it becomes though increasingly difficult to have a stable and tunable LO source with sufficient power to pump the HEB. The available output power of commercially available LOs decreases exponentially with the output frequency [2]. For frequencies higher than $\approx$ 2 THz there are still no commercial tunable solid state LOs. In this frequency range far infrared gas laser sources or backward wave oscillator (BWO) with multipliers (see below) are typically used. Gas laser sources deliver adequate power but are not tunable and are more difficult to operate and less stable in output power than solid state LOs. New developments in semiconductor laser technology (quantum cascade lasers) seem to be able to break up this

limitation in near future [94]. Quantum cascade lasers are compact in design and deliver tunable continuous wave signals of enough power to operate a heterodyne receiver.

During this thesis the following LOs have been used to pump the HEBs and measure its characteristics. Some of them are new developments, which had to be optimized during the HEB measurements, since HEBs need a very stable LO power output to work as a mixer.

0.8 THz :

- Solid state LO based on a Gunn diode at 133–147 GHz and a multiplier chain ($\times 2 + \times 3$) delivering a maximum power of 112 μW at 804 GHz and being tunable over a bandwidth of 50 GHz.

- Photonic LO: A low-temperature grown GaAs metal-semiconductor-metal (MSM) photonic local oscillator (LO) is illuminated by two near-IR semiconductor lasers, generating a tunable beat frequency in the THz range. This LO source is a new development which is intended to be used at higher frequencies. A HEB with dimensions 4 $\times$ 0.4 $\times$ 0.004 μ m^3 was pumped with the LO delivering 450 nW. Details on these measurements and on the photonic LO can be found at [70].

1.4 THz :

- Solid state LO based on a Gunn diode at 114–125 GHz and a multiplier chain ($\times 3 + \times 4$) delivering a maximum power of 1 μW [95] at 1461 GHz (the manufacturer has measured 3 μW [96]) and being tunable over a bandwidth of 130 GHz (1370 – 1500 GHz).
- YIG oscillator at 19 GHz followed by a frequency multiplier/amplifier chain ($\times 2$, power amplifier, $\times$ 4 $\times$ 3 $\times$ 3), providing 1–3 μW output power at 1.368 THz (the manufacturer specified 4–10 μW [97]. This LO is tunable in the frequency range 1251–1389 GHz and can be expanded up to 1530 GHz with an exchangeable module.

1.9 THz :

- FIR laser system: A CO_2 laser was tuned on the 9P36 line and pumped the methanol line of a following FIR laser at 170,576 μm

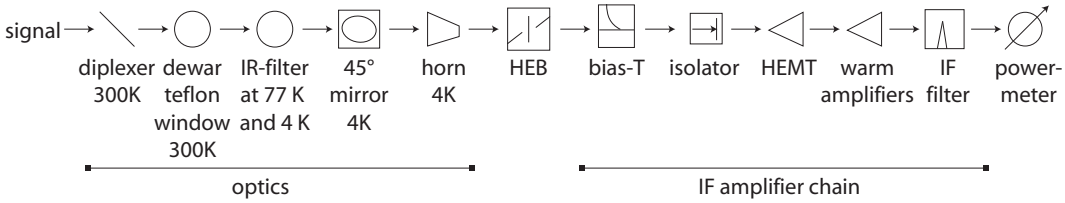

Fig. 6.5: *Flow chart of the receiver components which contribute to the total receiver noise.*

wavelength (1758.75 GHz, which is also in the RF bandwidth of the 1.9 THz HEB mixer). Output LO power was sufficient to comfortably pump the mixer but has not been measured. A further difficulty was that the CO_2 laser line also pumped an additional, much stronger methanol line at 2.5 THz in a blinking, instable manner, which was also coupled into the HEB pumping it up additionally. Some valuable measurements could be performed though, since this effect was not permanent. A 10 μm beam splitter with 29% reflection at 1.9 THz was used which added substantially to the receiver noise.

- 1.9 THz measurements were also performed using the GREAT receiver in its flight configuration for SOFIA. GREAT uses a backward wave oscillator (BWO) at 600 GHz with a frequency tripler for the LO source. The LO frequency used here was 1.890 THz. Using the BWO as a LO source for HEBs was a new development too. Details can be found in [71].

6.1.4 Mixer noise temperature and mixer gain.

The equivalent noise temperature of a receiver can be measured using the standard Y-factor method. In order to determine the HEB mixer performance as a part of the receiver, it is necessary to estimate the losses and the noise in different parts of the setup. Figure 6.5 shows the signal path through the optical and electrical components of the receiver.

To calculate the mixer noise the general expression for the equivalent receiver noise temperature can be used [6]:

$$T_{rec} = T_{opt} + \frac{T_{mix}}{G_{opt}} + \frac{T_{IF}}{G_{opt}G_{mix}} + \mathcal{O}\left(\frac{1}{G_{IF}}\right), \tag{6.10}$$

T_{opt} and G_{opt} being the equivalent noise temperature and the gain caused at the optics before the mixer, T_{mix} and G_{mix} the noise temperature and the

gain of the mixer, and T_{IF} and G_{IF} the noise temperature and gain of the subsequent amplification IF chain (cryogenic low noise amplifier and warm amplifiers previous to the power measurement — backend). Since the gain of the amplifier chain G_{IF} is very high, the last terms are small and can be approximated to zero.

The gain of the optics can be measured or estimated using computer simulation. To measure the transmission loss, a Fourier Transform Spectrometer (FTS) is used. From the ratio of two measurements, one with the optical component in the optical path and another outside of it, the transmission of the component is determined as a function of frequency. Often the actual component cannot be measured in this way. A component of the same dielectric material is then used. The transmission of the actual components is then calculated assuming the same material parameters and perfect planparallel plate of dielectric.

The equivalent noise temperatures of the optics is given by:

$$T_{opt} = \frac{1 - G_{opt}}{G_{opt}} T, \tag{6.11}$$

T being the physical temperature of the optical component.

The gain and equivalent noise temperature of the IF-amplifier chain can be easily obtained. The mixer block is heated to different temperatures beyond the superconducting transition temperature of the HEB (8–30 K) and the output power at the end of the IF-chain is measured for several IFs in a well defined bandwidth B. The hot mixer behaves then as a Johnson noise source which is amplified by the IF chain[3]. The generated noise power can be calculated using the Rayleigh-Jeans limit (ν_{IF} =1–2 GHz)

$$P_{load} = kBT \tag{6.12}$$

and compared to the measured output power for different temperatures. The total input power $P_{IF,in}$ is the sum of the load power P_{load} and the noise generated by the IF-amplifier chain $P_{IF,noise}$. The oputput power P_{out} is given by

$$P_{IF,out} = P_{IF,in} \cdot G_{IF} = P_{load} \cdot G_{IF} + P_{IF,noise} \cdot G_{IF}. \tag{6.13}$$

We can plot the dependence of $P_{IF,out}$ on P_{load} for different temperatures and fit a linear dependence assuming the gain G_{IF} to be constant. According to

[3]Separate measurements using a heated 50 Ω load showed that the results were identical to those measurements performed using the mixer block as a load.

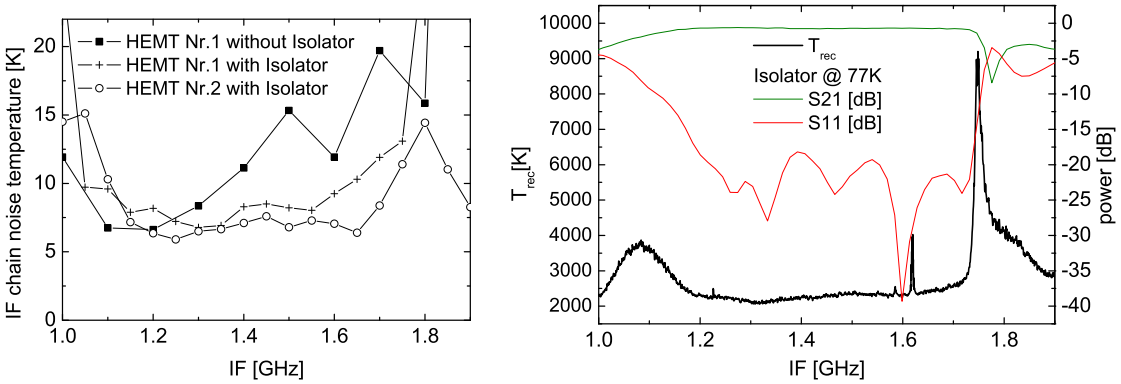

Fig. 6.6: *Left: Equivalent noise temperature for three different IF chains over the IF. Right: Receiver noise temperature (left-hand scale) over the IF of an exemplary mixer (#312 at 1.9 THz) and transmission (S11) and reflection (S12) (right-hand scale) of the used isolator at 77 K (independently measured with a network analyzer). Note that the isolator bandwidth corresponds well to the receiver IF bandwidth.*

equation 6.13 the slope of the linear regression is G_{IF} and the axis intercept $y_0 = P_{IF,noise} \cdot G_{IF}$. The equivalent noise temperature of the IF-chain can be calculated using Rayleigh-Jeans:

$$T_{IF} = \frac{P_{IF,noise}}{kB} = \frac{1}{kB}\frac{y_0}{G_{IF}}. \tag{6.14}$$

The mixer gain G_{mix} is calculated using the relation:

$$G_{rec} = G_{opt} \cdot G_{mix} \cdot G_{IF} \Rightarrow G_{mix} = \frac{G_{rec}}{G_{opt} \cdot G_{IF}}. \tag{6.15}$$

Using the obtained results for G_{opt}, T_{opt}, G_{mix} and T_{IF} the mixer noise temperature T_{mix} can be calculated using equation 6.10:

$$T_{mix} = (T_{rec} - T_{opt}) \cdot G_{opt} - \frac{T_{IF}}{G_{mix}}. \tag{6.16}$$

The calculation of the mixer noise temperature is important in order to compare devices which have been measured using different optics or different IF chains (see section 6.1.6 below). This method has limitations, since it is not always possible to measure the real losses of the optics or at the IF chain with the desirable accuracy. Besides, the mixer and the IF chain are interdependent and influence each other. Three selected measurements of the IF chain noise temperature are presented in fig. 6.6. All measurements

were performed using the same IF components with exception of the HEMT amplifier and the isolator. The isolator limits the measurement bandwidth on the low side but helps eliminate standing waves for higher IFs. Many measurements have been performed using the HEMT Nr. 1 without isolator due to availability. The HEMT Nr. 1 does not deliver a flat noise amplification above 1.5 GHz IF — also with isolator. The calculations done for the mixer noise temperature T_{mix} of devices which have been measured with HEMT Nr. 1 also show a similar characteristic behaviour (roll-off at 1.6 GHz IF). Devices originating from the same batch which have been measured using the HEMT Nr. 2 do not show an increase of the mixer noise temperature over the IF and specially a peak at 1.3 GHz and 1.6 GHz. This has to be taken into account when considering measurements using the HEMT Nr. 1. The IF chain with the HEMT Nr. 2 shows a constant low noise temperature for IFs from 1.15–1.70 GHz. In this case the bandwidth is mainly narrowed by the isolator, as could be confirmed measuring the isolator characteristics with an network analyzer.

6.1.5 Noise bandwidth

There are two basic IF bandwidth numbers. The first considers the mixer gain and is defined as the IF at which the mixer gain is reduced by 3 dB, i. e. to the half of its value at low IF (*gain* bandwidth). The second definition considers the equivalent mixer noise and is defined as the IF at which the mixer noise is doubled as compared to the value at low IF (*noise* bandwidth). Since the gain and the noise could not be measured at low IF it is supposed that the HEB performance is nearly equal up to a certain IF, from which it starts to rapidly decrease. This IF is also referred to as the *roll-off* frequency.

To measure the noise bandwidth, a receiver noise temperature measurement is performed for different IFs in 50 or 100 MHz steps. As back end a powermeter with a tunable IF filter is used. The measurements are performed subsequently in a stable non-chopped manner for each IF. During the measurements the bias conditions of the mixer (the LO power and the bias voltage) must not change. In fig. 6.1 results are presented for three different receivers.

A basic limitation regarding our measurements is the very reduced bandwidth of the heterodyne setup of only 500 MHz. The highest IF at which measurements could be done was 1.7 GHz, since the used isolator has a very narrow band (1.2–1.7 GHz). Besides, as commented above, using an amplifier with a slope in its noise characteristics does not allow to make reliable IF

	0.8 THz	1.4 THz	1.9 THz
G_{opt}	0.74	0.60	0.55
T_{opt}	60 K	100 K	180 K
G_{IF}	102 dB	103.4 dB	107.4 dB
T_{IF}	6.7 K	8.29 K	7.11 K
G_{mix}	-6 dB	-13 dB	-19 dB

Tab. 6.2: *Parameters used for the calculation of the mixer noise temperature. The optical gain parameter for the optics in the test dewar at 0.8 THz and 1.4 THz are taken from table 6.1. The data for the GREAT receiver are taken from Wagner [98]. The equivalent noise temperatures for the optics are obtained using equation 6.11. The mixer gain is obtained using equation (6.15). Values for G_{IF}, T_{IF} and G_{mix} given at 1.4 GHz IF only.*

noise bandwidth measurements. The devices measured with the HEMT Nr. 2 (with almost equal noise over the measured band) do not show a roll-off below the measured IF bandwidth.

6.1.6 Different mixers with the same dimensions

In this section three devices which have the same nominal dimensions are compared. The considered devices were designed for 0.8 THz, 1.4 THz and 1.9 THz waveguide mixers and were integrated in different receiver setups with different horns.

At 0.8 THz a test receiver as shown in fig. 6.3 and 6.4 has been used with the IF chain without isolator and with the HEMT Nr. 1. A solid state LO [96] at 804 GHz has been used. The signal was diplexed using a 10 μm beam splitter with 5% LO transmission. The LO had to be detuned to reduce its output power for optimal HEB operation. Data on the optical setup are given in table 6.1. A Potter horn [99] was used.

The measurements at 1.4 THz were performed using the same test dewar but with an isolator and the HEMT Nr. 2 in the cryogenic amplifier chain. The optical path is shown in fig. 6.8 using a different mirror, sliding carriage and a corrugated horn. The optical path length in air was approximately one meter including a Martin Puplett Interferometer (MPI) for diplexing signal and LO. A rotatable grid was placed between the LO source and the MPI to reduce the LO power for optimal HEB operation. The optics for this experiment were designed by K. Rettenbacher [100]. Unfortunately, a design mistake resulting in a slight tilt of the mixer was not realized until the measurements were completed. This alignment failure can explain the comparably large 1.4 THz

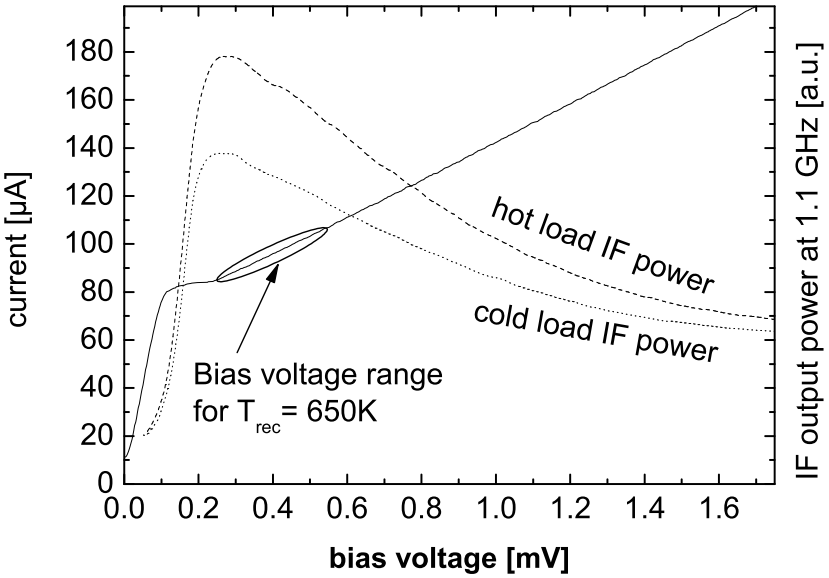

Fig. 6.7: *Heterodyne performance at 0.8 THz. The continuous line shows the pumped I-V curve. Dashed and dotted lines show the IF output power for a hot and a cold load signal, respectively. The system noise temperature is 650 K in the 0.2-0.6 mV bias range (IF 1.1 GHz, IF bandwidth 80 MHz).*

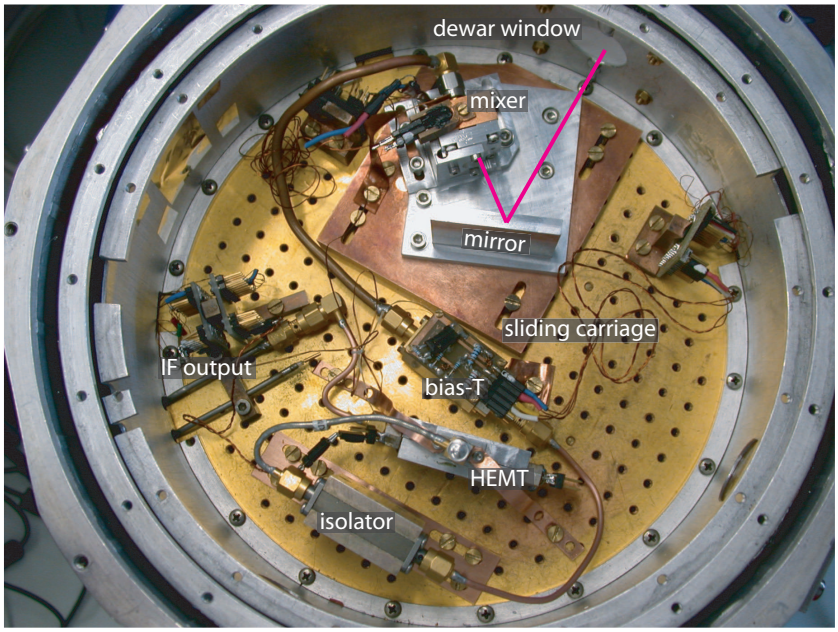

Fig. 6.8: *Top view of the open 4 K stage of the cryostat with the optics arranged for the 1.4 THz measurements. The optical path is marked by a line.*

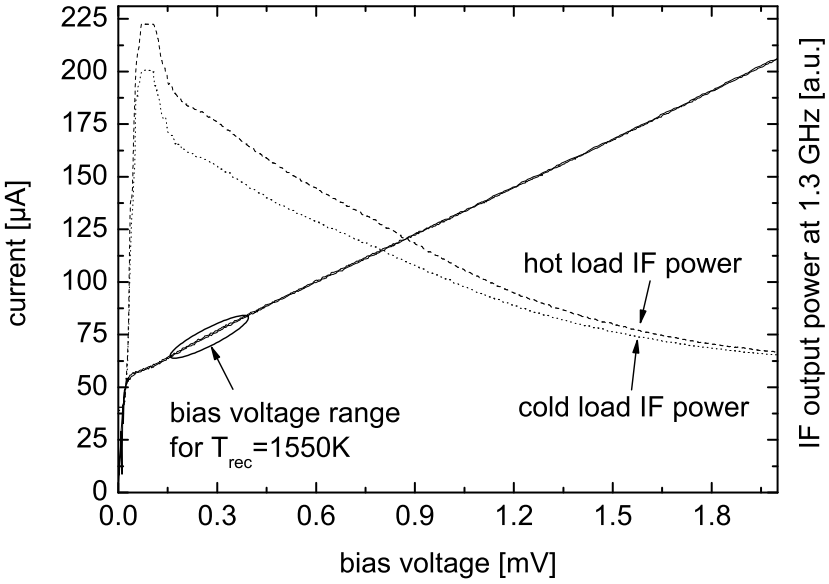

Fig. 6.9: *Heterodyne performance at 1.4 THz. The continuous line shows the pumped I-V curve. Dashed and dotted lines show the IF output power for a hot and a cold load signal, respectively. The system noise temperature is 1550 K in the 0.2-0.5 mV bias range (IF 1.3 GHz, IF bandwidth 80 MHz).*

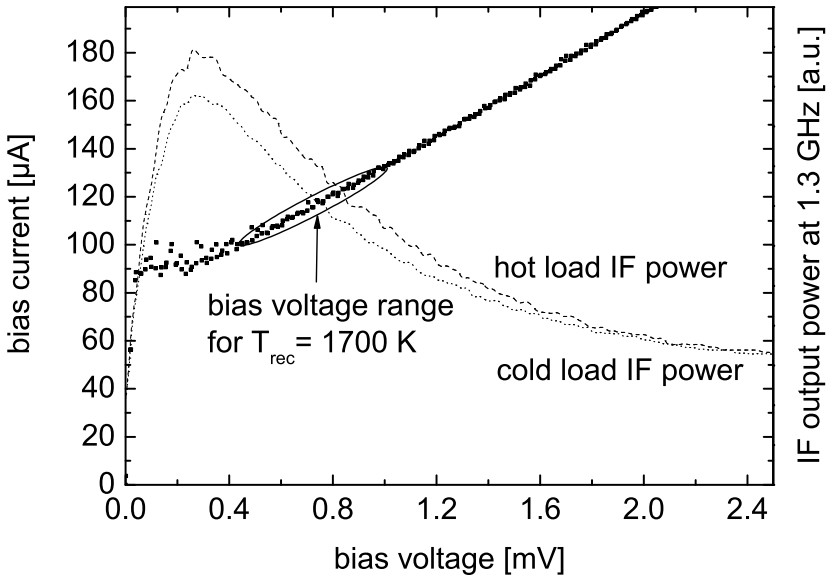

Fig. 6.10: *Heterodyne performance at 1.9 THz. The continuous line shows the pumped I-V curve. Dashed and dotted lines show the IF output power for a hot and a cold load signal, respectively. The system noise temperature is 1700 K in the 0.5-1.0 mV bias range (IF 1.3 GHz, IF bandwidth 80 MHz).*

mixer noise (see fig. 6.11). Another possible reason for even a lower optical gain could be the 1 m optical path in lab air, which was very humid during measurements (relative moisture $\sim$87% at 28°C while measurements). The receiver at the APEX telescope in Chile showed a receiver noise temperature $T_{rec} = 1600$ K, while the lab measurements using the same mixer (#311) showed $T_{rec} = 2000$ K. The large difference cannot be explained by air humidity alone.

The 1.9 THz measurements were performed using the GREAT receiver in its flight configuration for SOFIA. GREAT uses a backward wave oscillator (BWO) at 600 GHz with a frequency tripler. The LO frequency used here was 1.890 THz. The LO power can be adjusted directly by manipulating the heating current on the BWO [71]. The optics of GREAT are evacuated and also use a MPI for diplexing. Fig. 6.10 shows the pumped IV-characteristics of the HEB, together with the IF output power at 1.3 GHz as a function of bias voltage. In this setup the voltage bias is slowly scanned for the hot load and for the cold load in separate measurements.

The DSB receiver noise temperature has been measured with the standard Y-factor method. Fig. 6.11 shows the uncorrected receiver noise temperature

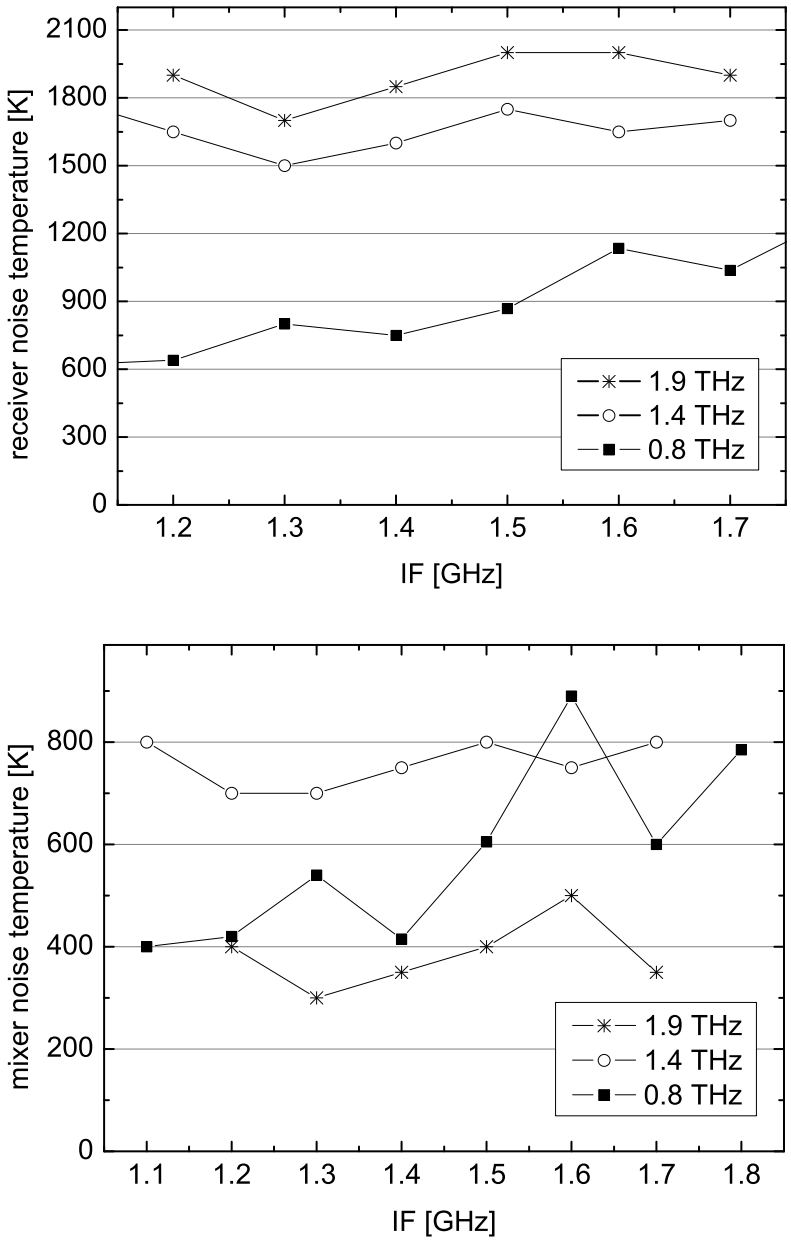

Fig. 6.11: *Up: Uncorrected receiver noise temperature for three HEB receivers. All devices were from the same batch and had the same bridge dimensions (0.4 × 4.5 μm^2). The values have been obtained from Y-factor measurements using the C&W formula to calculate the equivalent load temperatures. The measurements at 0.8 THz were performed with the HEMT Nr. 1 (with increasing noise in the measured band). Bottom: Mixer noise temperature calculated using equation (6.16) and data from table 6.2*

of all three receivers over the IF band. The measurements were performed at a constant bias voltage in a non-chopped, static measurement.

The *mixer* noise temperature has been calculated from these measured receiver noise temperatures using equation (6.16). Results are shown in fig. 6.11. The data used for these calculations are listed in table 6.2. The mixer at 0.8 THz shows a roll-off in the mixer noise at 1.5 GHz. This probably originates from the HEMT Nr. 1 and not from the mixer, since the features of the IF chain noise and of the mixer noise are comparable (see fig. 6.6 and fig. 6.11). The high values for the 1.4 THz mixer noise can be due to unconsidered optic losses (i. e. air water vapor in 1 m non-evacuated optics, horn and especially the mentioned misalignment) and encourages further improvements. Data for the 1.9 THz mixer noise were obtained at the GREAT receiver under vacuum. The optical losses for its setup have been very well studied [98].

The three mixers shown here have equal dimensions, originate from the same batch and could therefore be expected to show similar mixing performance. The calculation of the mixer noise —considering the misalignment of the optical path at the 1.4 THz measurement— clearly corroborates this assumption and speaks for the reproducibility of the fabricated mixers.

On the contrary, the data for the mixer gain seem to suggest a RF frequency dependence. In our data set the mixer gain decreases with increasing RF. The change cannot be explained alone by the worse signal matching at higher frequencies. Therefore, an intrinsic effect in the HEB may be responsible for the mixer gain loss at higher RF frequencies. Unfortunately, there is yet no explanation for this effect.

6.1.7 Devices with different dimensions

In this section measurements of three mixers are compared. The mixers are from the same fabrication batch and differ only in their bridge width. The devices were designed to have different impedances; the waveguide probes have been designed to match the respective impedance (see 3.1.5 and [23]) to the waveguide. All three mixers have been measured using the same setup.

The already described test receiver at 0.8 THz was used for these measurements. An isolator and HEMT Nr. 2 have been used for the cryogenic IF chain. The back-end was a power meter with a tunable IF filter. The devices are held at a constant bias point and the output power is measured for a hot (290 K) and a cold (77 K) load in a static non-chopped way keeping the LO power constant. The measurements were also done by sweeping the bias

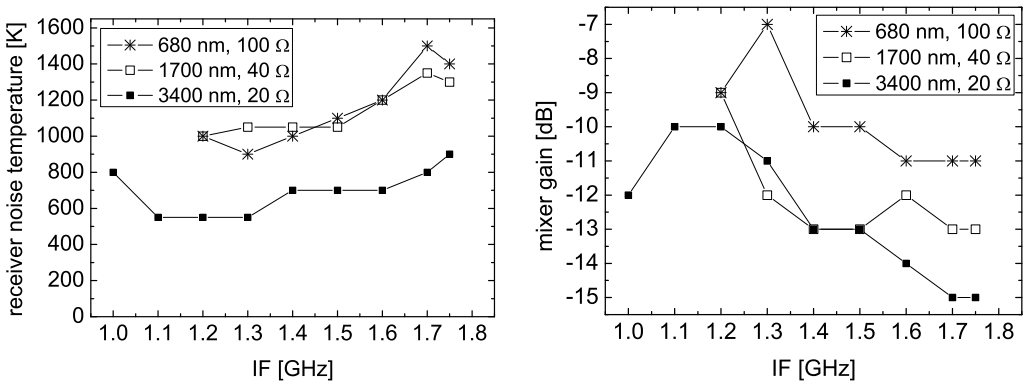

Fig. 6.12: *Uncorrected receiver noise temperature for three HEB receivers at 0.8 THz. All devices had the same length (300 nm) but different widths (given in the inset). On the right the calculated mixer gain (using equation 6.15) for the three HEB mixers. The correction was the same for all three devices, since G_{opt} and G_{IF} was the same in all measurements.*

voltage (at constant LO power) for the hot and the cold load.

The receiver with the narrowest device (680 nm, 100 Ω) shows the highest conversion gain (see fig. 6.12 on the right) but the lowest receiver noise temperature is measured for the widest device (3400 nm, 20 Ω) as can be seen in fig. 6.12 on the left.

6.1.8 LO-power requirement

The LO power requirement is an important issue since the available power from available solid state LOs decreases exponentially with frequency [2, 101]. This is a technological fact rather than a physical limit. The required coupled power increases with the HEB volume [32]. Hence, the available LO power constrains the size of the device. Since the performance of HEB mixers usually deteriorates when reducing the HEB device size (bridge area) [102, 101, 48] the available LO power constrains the maximum device size and therefore also the performance.

The required LO power can be calculated from material parameters [32]:

$$P_{LO} = \frac{1}{\alpha} A \cdot V (T_c^n - T^n - n T_c^{n-1} \Delta T_c), \tag{6.17}$$

with V the film volume, A and n material dependent constants ΔT_c the width of the resistive transition and α the coupling factor of radiation to the mixer.

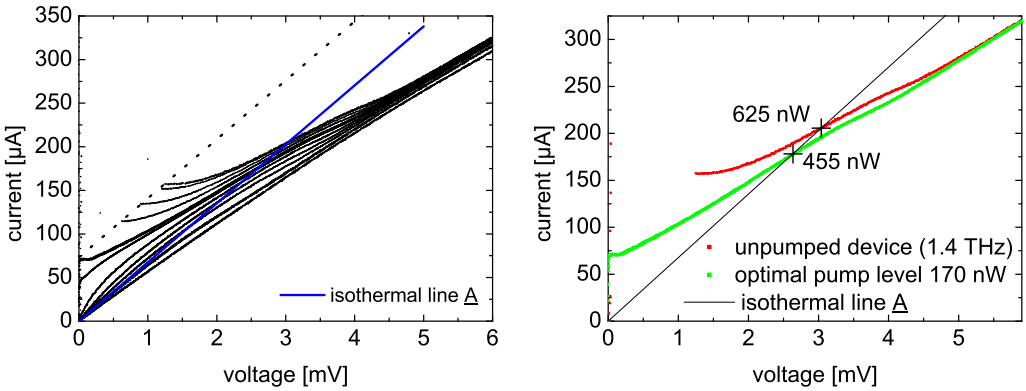

Fig. 6.13: *I/V characteristics of a selected HEB device (311) for many different pump levels. The criterion used in this thesis to determine the slope of the isothermal line $\bar{A}$ is shown by the dotted line, which connects the I_h values. This is an arbitrary criterion. The plot on the right shows only the two I/V curves which are needed to determine the required LO power for optimal operation.*

T is the bath temperature and it is assumed that P_{LO} is capable of heating the electron gas to the critical temperature of the bridge. In this expression it is assumed that the phonon temperature equals the bath temperature. Unfortunately the material parameters A and n have to be determined from empirical measurements which have a low absolute accuracy.

An empirical method to estimate the LO power requirement is the isothermal method [103]. In the isothermal method the basic assumption is that the absorption of DC or RF power has the same influence on the HEB device resistance. The absorbed LO power is derived from two I/V curves with different LO powers. At each point of a constant resistance line the total power absorbed by the HEB device is given by

$$P_{LO} + V_a I_a = \alpha P_{LO} + V_b I_b, \tag{6.18}$$

where α is the attenuation factor for the two different LO levels.

The attenuation factor is $\alpha = 0$ if one of the I/V curves corresponds to an unpumped HEB. In this case equation 6.18 is simply:

$$P_{LO} = V_{unpumped} I_{unpumped} - V_a I_a. \tag{6.19}$$

The absorption of the DC and RF power is more uniform when the HEB is normal conducting. Therefore, the isotherms are chosen to intersect the I/V graphs at values in which the HEB is normal conducting [104].

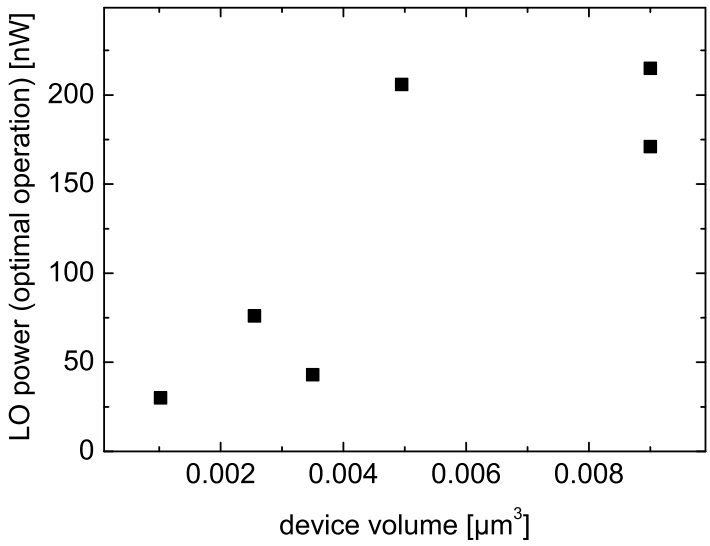

Fig. 6.14: *The required LO power for optimal mixing performance has been estimated using the isothermal technique as described. The device volume values are taken for assumed 5 nm film thickness and nominal fabrication lateral dimensions. All devices employed in this plot belong to the same fabrication batch.*

The results strongly depend on model parameters such as the slope of the line $\bar{A}$ chosen to determine V_a and I_a. A convention is called for to make measurements on different mixers comparable, since the value of the absorbed power varies considerably depending on the slope of the isotherm. In this thesis an arbitrary criterion has been set to determine the isothermal resistance making independent measurements of different mixers comparable. Some I/V curves with different pump levels are considered for the evaluation of one mixer. The curves which are insufficiently pumped show a hysteretic behaviour; the corresponding I_h/V_h values just before the HEB reenters in the superconducting state are connected by a straight line $\bar{p}$ (see dotted line in fig. 6.13). The isotherm line $\bar{A}$ is —in this thesis— parallel to $\bar{p}$ (and goes through the origin).

Using this convention the required LO power has been determined for some mixers as shown in table 6.3. The plot on fig. 6.14 the required LO power versus the bolometer bridge volume. The scattering is caused to some extent by the uncertainty for the device dimensions and also by the large tolerances of the isothermal method.

The calculated LO power requirements using the isothermal method is

mixer	ν [THz]	l [μm]	w [μm]	V [μm^3]	P_{max} [nW]	P_{opt} [nW]	P_{opt}/P_{max}
2001	0.8	0.3	0.68	0.001	56	30	0.53
2005	0.8	0.3	1.7	0.002	179	76	0.42
519	1.4	0.25	2.8	0.004	161	43	0.26
2004	0.8	0.3	3.3	0.005	352	206	0.58
311	1.4	0.4	4.5	0.009	626	171	0.27
2010	0.8	0.4	4.5	0.009	557	215	0.38

Tab. 6.3: *Required LO power for several devices. l, w and V are nominal device length, width and volume. P_{max} is the LO power needed to fully suppress device superconductivity at zero DC-bias. P_{opt} is given for optimal mixer performance.*

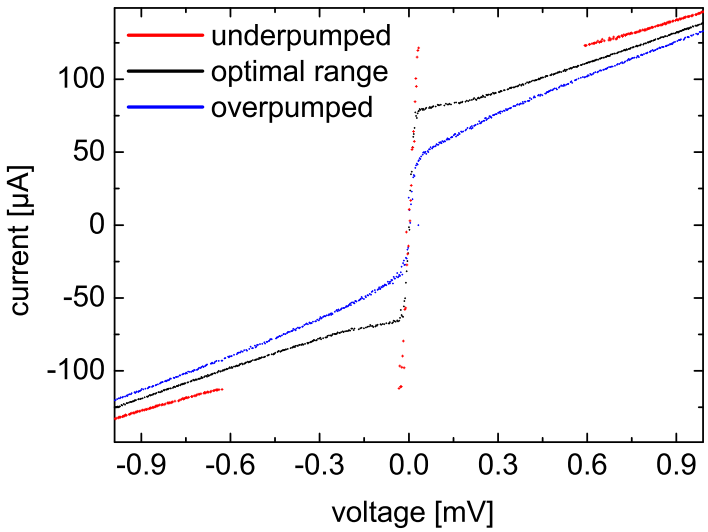

Fig. 6.15: *RF-I/V curves of a HEB mixer pumped with three different LO powers. The mixer performance is optimal when the LO power just suppresses the hysteretic behaviour.*

consistent with the LO power measurements which have been done at the LO output side before optics for mixers 312 [71] and 2010 [70] after subtraction of the optic losses.

From our experience, optimal mixer performance is achieved, when the LO power just suppresses the hysteretic feature in the I/V plot (see fig. 6.15). This has been observed for all tested membrane mixers. Differently, HEBs based on thick Si substrates need to be pumped more strongly for best performance. The LO power must be then increased until the I/V shows a "soft" transition from the superconducting $V = 0$ bias region into the ohmic part of the I/V plot. The "overpumped" I/V plot on fig. 6.15 illustrates an optimally pumped HEB in the case it is deposited on a thick substrate. This behaviour has been observed on NbTiN HEB mixers made inhouse [1] and also by other groups (see for instance [105]).

Model calculations made on membrane-based HEBs [51] had already predicted this behaviour due to the lower heat capacity of the membrane(see also chapter 2).

6.2 Fourier transform spectroscopy measurements

The frequency response of the receiver is determined by operating the HEB as a direct detector in a Fourier Transform Spectrometer (FTS).

The FTS consists of a Michelson interferometer and a broadband mercury arc lamp, which emits radiation in the submillimeter frequency range. One of the Michelson mirrors is fixed, while the other can be moved. Due to the Fourier transformation, the frequency resolution is defined by the maximum mirror displacement. In the FTS setup at KOSMA, a maximum mirror travel path of 43 mm leads to a resolution of 3.5 GHz. The FTS optics and the optical path including the interface to the dewar can be evacuated to reduce the absorption by water vapour in air. To this purpose, a new dewar window has been designed that acts as a vacuum flange to the FTS optic chamber.

The broadband source is chopped and the electrical response of the device is measured using a lock-in technique. The HEB is brought close to its transition temperature by heating it slightly and it is biased to a voltage at which the direct detection efficiency is as high as possible. The absorbed light heats the bolometer bridge and its resistance increase is registered by the change in DC bias current.

Illustrations 6.17 and 6.19 show FTS measurements of two selected HEB

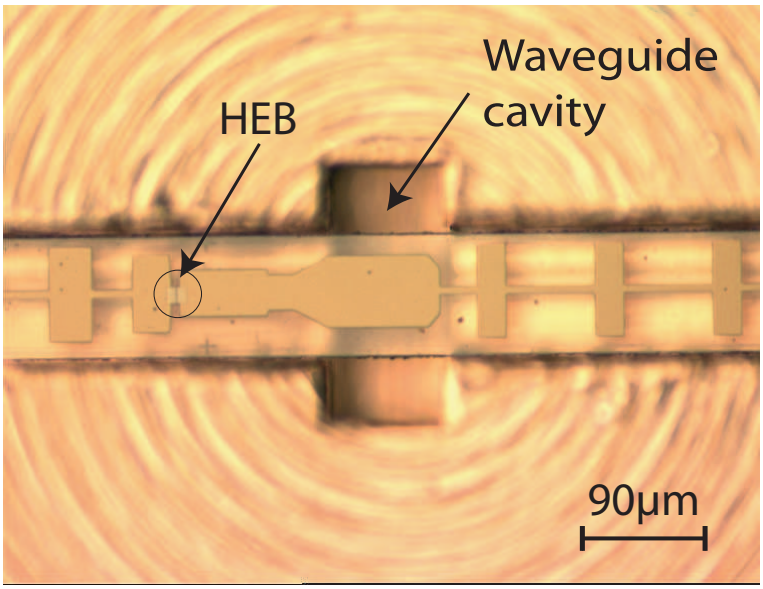

Fig. 6.16: *Microscope photograph of the HEB membrane device 519 (1.4 THz) with its probe aligned in the waveguide mount. The waveguide design required the probe to look to be slightly "displaced".*

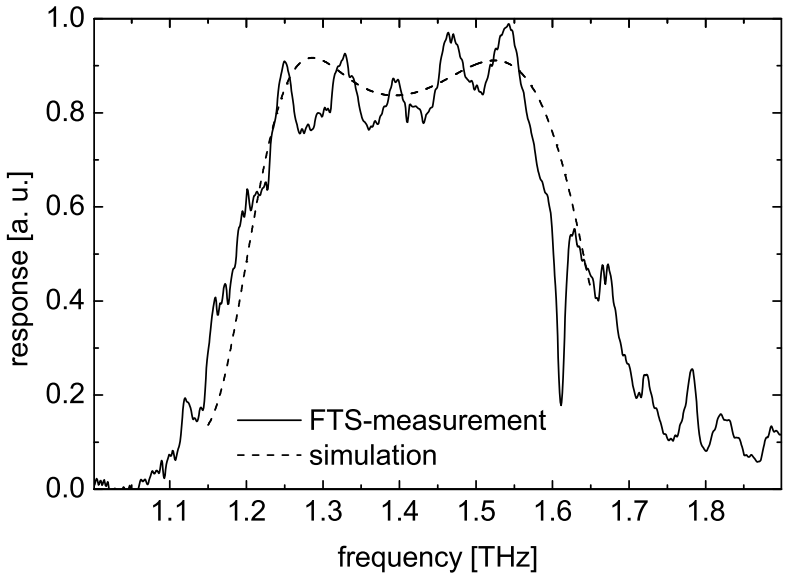

Fig. 6.17: *Normalized FTS spectrum of the HEB mixer with the device displayed above (fig. 6.16). The results fit the simulated data very well, which confirms the good positioning of the probe in the waveguide. Simulation from [23].*

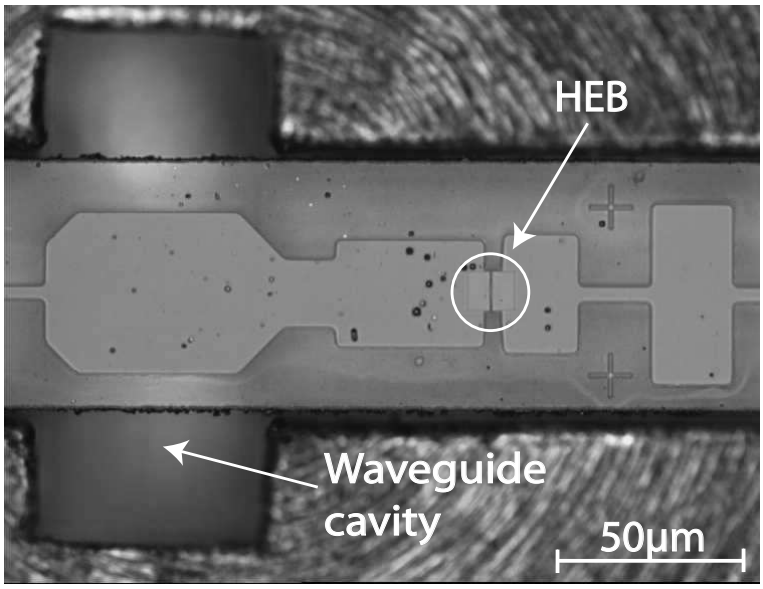

Fig. 6.18: *Microscope photograph of the HEB membrane device 312 with its probe aligned in the waveguide mount. The waveguide probe has been designed by T. Tils [23].*

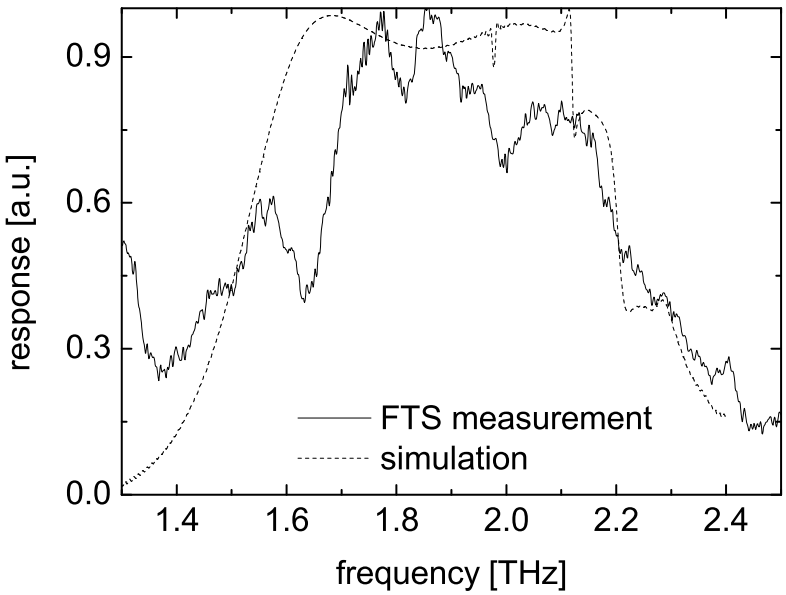

Fig. 6.19: *Normalized FTS spectrum of the HEB mixer at 1.9 THz considered above (device 312). The simulations have been performed by T. Tils [23]. Measured data show a mean fit to the simulated data. The measurements were performed at 1–2 mbar air pressure.*

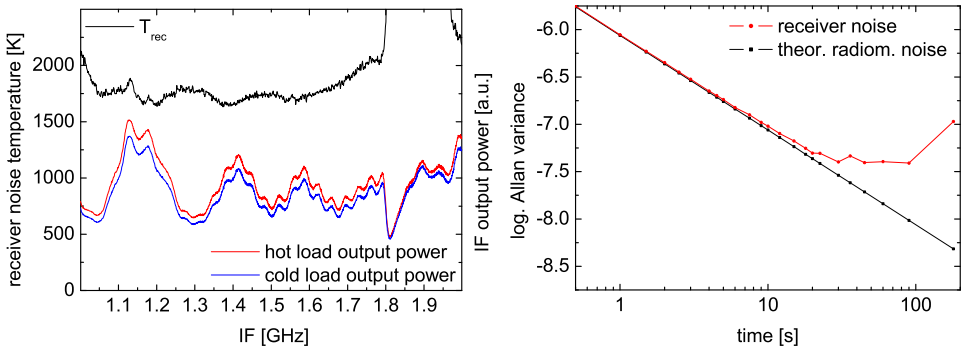

Fig. 6.20: *Receiver noise temperature of the mixer 519 (250 nm bridge length times 2.8 µm bridge width) at 1.4 THz measured in the test dewar over the IF measured with the standard Y-factor method for a fixed bias voltage using an Acousto-Optic Spectrometer (AOS) as backend. On the right the measured spectral allan variance for this device is shown.*

mixers with their corresponding simulated coupling efficiency. The FTS setup was optimized for measurements at 600 GHz. The obtained data show that the RF coupling for the 1.4 THz device is much closer to the simulation than the 1.9 THz device.

6.3 Stability measurements

Increasing the measuring time (integration time) leads to a decrease of the minimum detectable signal temperature ΔT^A_{min}:

$$\Delta T^A_{min} = \frac{T_{rec}}{\sqrt{\Delta\nu\tau}} \,. \tag{6.20}$$

Here $\Delta\nu$ is the detection bandwidth (fluctuation bandwidth at the resolution desired for the observation) and τ the integration time of the measurement (only for the white noise). The noise of any receiver can be seen as a combination of two terms: white noise and drift. There is a maximum integration time, known as the minimum Allan time τ_A, beyond which the signal/noise ratio drops slower than the white noise, or even increases.

There are two main different ways to measure τ_A. In all of them a series of measurements of a constant source are analyzed. In the first one, the variance of the base line fluctuations over time, called total power Allan variance [106], determines τ_A. The total power Allan variance registers the instability from a common gain variation across the whole band.

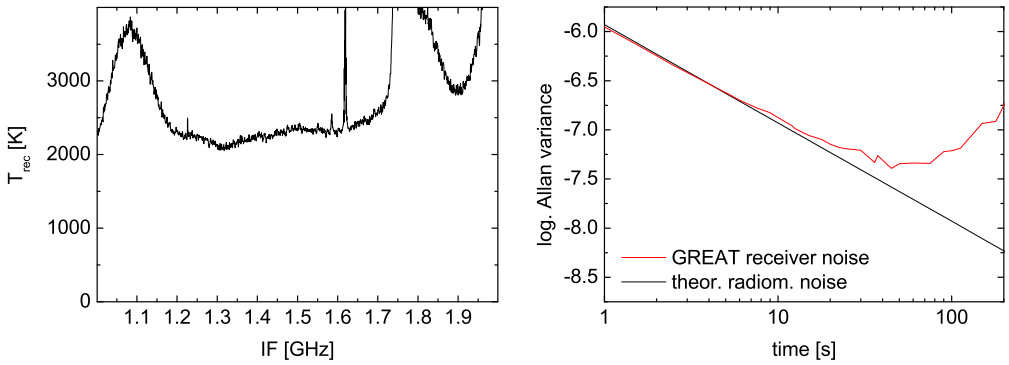

Fig. 6.21: *Receiver noise temperature of the mixer 312 over the IF measured in the GREAT receiver with the standard Y-factor method for a fixed bias voltage using an AOS as backend. On the right the measured spectral allan variance for this device is shown.*

The second way of calculating τ_A is based on the spectroscopic Allan variance [107]. The baseline fluctuations are not considered and a zero order correction is performed previous to calculation. The band is divided in several narrow channels and the spectroscopic Allan variance considers the relative variations of the different channels over a series of measurements.

Most astronomical heterodyne observations are eventually not intended for an accurate determination of the continuum level but for the measurement of lines on top of a constant baseline which is typically taken to be zero. In this case only fluctuations which do not influence all channels in the same way result in a degradation of the calibrated astronomical data, often seen as ripples or steps in the baseline. Therefore, the spectroscopic Allan variance time has the greater significance for HEB heterodyne mixers.

To measure the spectroscopic minimum Allan time a multi-channel Acousto-Optic-Spectrometer (AOS) has been used as a backend which simultaneously measures all channels over the whole receiver bandwidth. This is actually the standard receiver configuration for operation at the telescope. The mixer has been biased to the voltage at which it has shown the best receiver noise temperature and a control Y-factor measurement with a hot and cold load has been done delivering a IF-frequency dependent receiver noise temperature as shown in fig. 6.20. For the stability measurement the AOS repeatedly registers the signal produced by a hot load and the spectral Allan time can be computed out of the scans in the way presented in [108].

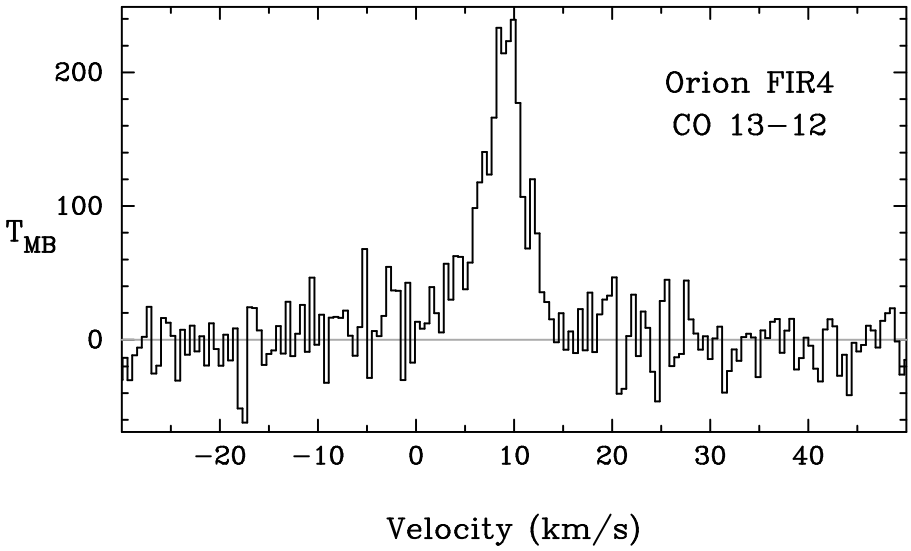

Fig. 6.22:

6.4 Astronomical Observations

The 1.4 THz CONDOR receiver has been installed at the APEX telescope in November 2005 using a 4 K pulse tube refrigerator and was successfully used to measure spectra of the carbon monoxide (J=13–J=12) rotational transition at 1.493 THz in several galactic sources (see fig. 6.22). The receiver noise temperature at APEX was $\sim$ 1600 K [3] for device 519, which is even below the laboratory measurements (see fig. 6.17). This can be due to the water vapor in laboratory air as compared to the very dry air at APEX. Also the Allan time stability measurements have been reproduced at the telescope.

Appendix A

Technical facilities.

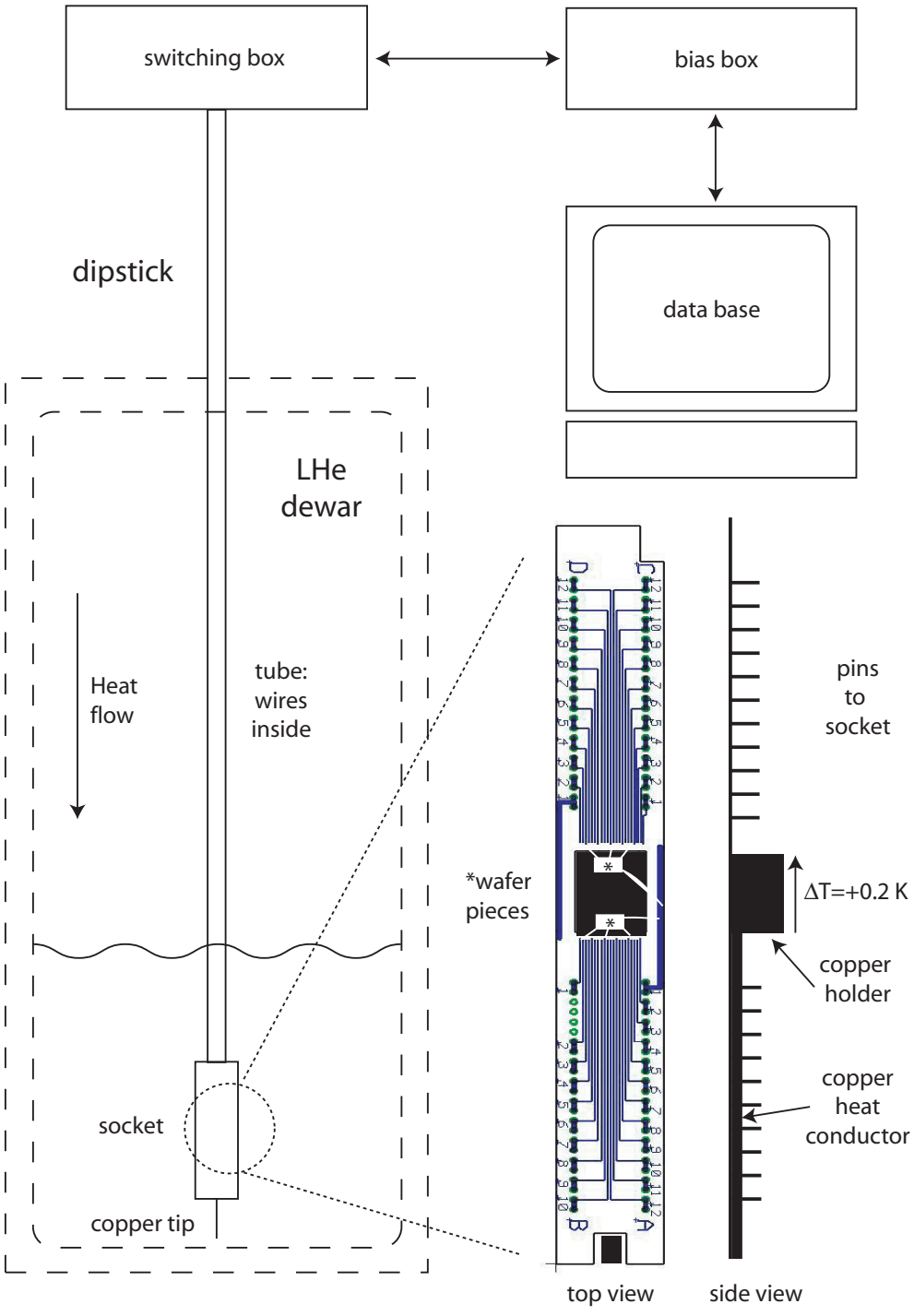

Fig. A.1: *Symbolic illustration of a dipstick setup. The socket is immersed in liquid helium but can also hang above it if the device is to be measured at temperatures T >4.2 K. The wafer pieces have 23 devices each. Only few bonding wires are shown for clarity. Inside the copper holder there is a temperature diode to register the device temperature. Since the heat is transported by the wiring inside the tube from outside the dewar, there is a certain temperature gradient at the copper holder of 0.2 K.*

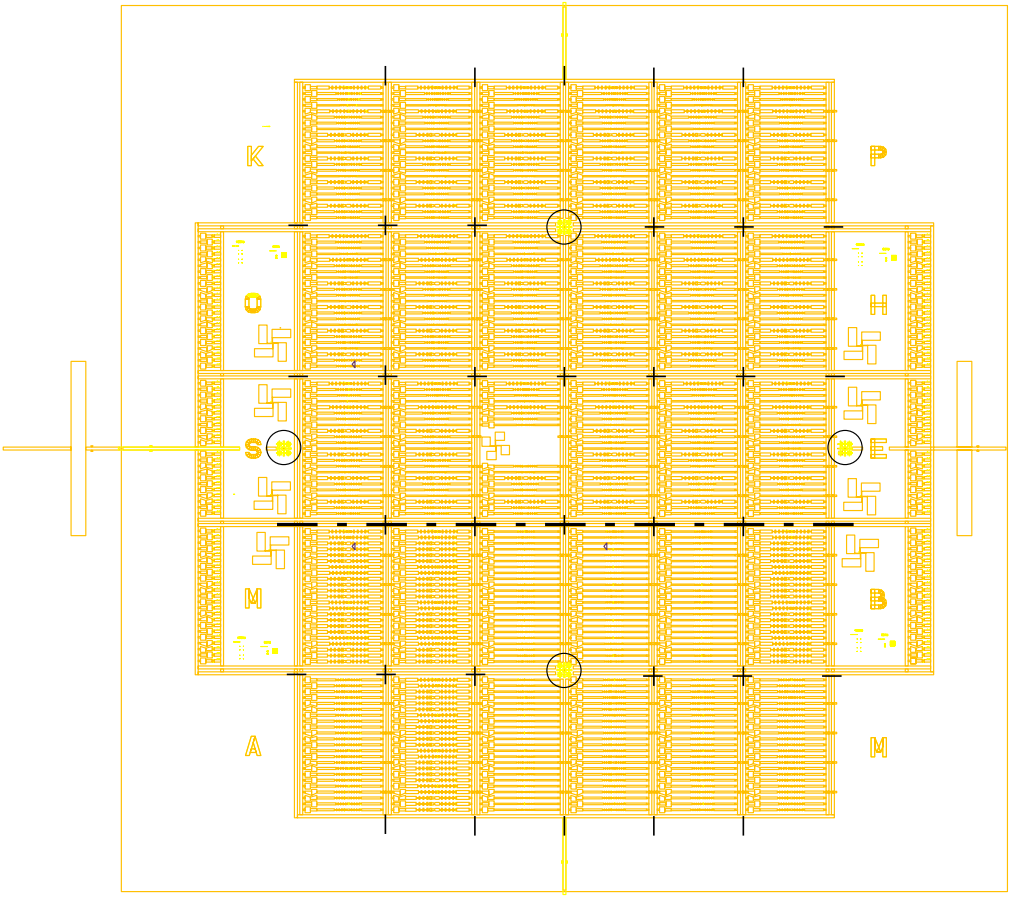

Fig. A.2: *The new layout for 30 mm square Si wafers. 690 devices for 0.8, 1.2, 1.4 and 1.9 THz RF optimized each for 20, 40 and 100* Ω *HEB impedance. The devices are distributed in 30 columns. Their limits are marked on the illustration by black crosses. The top eighteen columns have each devices for every RF and impedance while the bottom twelve are each dedicated only to one RF. The global marks —for wafer alignment— are marked with a circle on the illustration.*

Bibliography

[1] S. Bedorf. *Development of ultrathin niobium nitride and niobium titanium nitride films for THz hot-electron bolometers*. Dissertation (PhD thesis), KOSMA, 1. Physikalisches Institut der Universität zu Köln, 2005.

[2] D. L. Woolard, E. R. Brown, M. Pepper, and M. Kemp. Terahertz frequency sensing and imaging: A time of reckoning future applications? *Proc. of the IEEE*, 93:1722–1743, 2005.

[3] M. C. Wiedner, G. Wieching, F. Bielau, K. Rettenbacher, N. H. Volgenau, M. Emprechtinger, U. U. Graf, C. E. Honingh, K. Jacobs, B. Vowinkel, K. M.Menten, L. Nyman, R. Güsten, S. Philipp, D. Rabanus, J. Stutzki, and F. Wyrowski. First observations with CONDOR, a 1.5 THz heterodyne receiver. *Astronomy & Astrophysics.*, 454:L33–L36, 2006.

[4] C. Gal. *Development of a Wide Bandwidth Array Acousto-Optical Spectrometer for the Herschel Satellite Mission.* Dissertation (PhD thesis), KOSMA, 1. Physikalisches Institut der Universität zu Köln, 2005.

[5] C.M. Caves. Quantum limits on noise in linear amplifiers. *Physical Review D*, 26(8):1817–1839, 1982.

[6] O. Hachenberg and B. Vowinkel. *Technische Grundlagen der Radioastronomie*. B.I.-Wissenschaftsverlag, 1982.

[7] J. D. Kraus. *Radio Astronomy*. Cygnus-Quasar Books, 2nd edition, 1986.

[8] S. Ariyoshi, H. Matsuo, C. Otani, H. Sato, HM Shimizu, K. Kawase, and T. Noguchi. Characterization of an STJ-based direct detector of submillimeter waves. *Applied Superconductivity, IEEE Transactions on*, 15(2):920–923, 2005.

[9] M. Kenyon, PK Day, CM Bradford, JJ Bock, and HG Leduc. Background-limited membrane-isolated TES bolometers for far-IR/submillimeter direct-detection spectroscopy. *Nuclear Inst. and Methods in Physics Research, A*, 559(2):456–458, 2006.

[10] D. Prober. Ultrasensitive Quantum-Limited Far-Infrared Detectors. *American Physical Society, APS March Meeting, March 13-17, 2006, abstract# K5. 002*, 2006.

[11] A. Poglitsch, C. Waelkens, O.H. Bauer, J. Cepa, H. Feuchtgruber, T. Henning, C. van Hoof, F. Kerschbaum, D. Lemke, E. Renotte, et al. The photodetector array camera and spectrometer (PACS) for the Herschel Space Observatory. *Proceedings of SPIE*, 6265:62650B, 2006.

[12] Stefan Glenz. *Fabrication and Characterization of $Nb-Al/Al_2O_3-Nb$ Superconductor-Insulator-Superconductor Devices with NbTiN Based Tuning Circuits for the Herschel Space Observatory*. PhD thesis, KOSMA, 1. Physikalisches Institut der Universität zu Köln, 2005.

[13] J.R. Tucker and M.J. Feldman. Quantum detection at millimeter wavelengths. *Reviews of Modern Physics*, 57(4):1055–1113, 1985.

[14] J. R. Tucker. Quantum limited detection in tunnel junction mixers. *IEEE J. Quant. Electron.*, QE-15(11):1234–1258, 1979.

[15] Patrick Pütz. *Fabrication of superconductor-insulator-superconductor devices for heterodyne mixer applications with electron beam lithography*. Dissertation (PhD thesis), KOSMA, 1. Physikalisches Institut der Universität zu Köln, 2003.

[16] B. Bumble, H. G. LeDuc, J. A. Stern, and K. G. Megerian. Fabrication of Nb/Al-N_x/NbTiN junctions for SIS mixer applications. *IEEE Trans. Appl. Supercond.*, 11(1):76–79, 2001.

[17] A. Karpov, D. Miller, F. Rice, J. A. Stern, B. Bumble, H. G. LeDuc, and J. Zmuidzinas. Low noise SIS mixer for far infrared astronomy. In J. Zmuidzinas, W. S. Holland, and S. Withington, editors, *Proc. SPIE*, pages 616–621, Bellingham, WA, USA, June 2004. SPIE–The International Society for Optical Engineering.

[18] J. Schubert, A. Semenov, G. Gol'tsman, H.-W. Hübers, G. Schwaab, B. Voronov, and E. Gershenzon. Noise temperature of an NbN hot-electron bolometric mixer at frequencies from 0.7 THz to 5.2 THz. *Superconductor Science Technology*, 12:748–750, November 1999.

[19] Jörg Stodolka. *Fabrikation und Analyse supraleitender diffusionsgekühlter Hot-Electron-Bolometer als Terahertz-Heterodynmischer*. Dissertation (PhD thesis), KOSMA, 1. Physikalisches Institut der Universität zu Köln, 2003.

[20] D. E. Prober. Superconducting terahertz mixer using a transition-edge microbolometer. *Appl. Phys. Lett.*, 62(17):2119–2121, April 1993.

[21] E.M. Gershenzon, G.N. Gol'tsman, Y.P. Gousev, A.I. Elant'ev, and A.D. Semenov. Electromagnetic radiation mixer based on electron heating in resistive state of superconductive Nb and YBaCuO films. *IEEE Trans. Magn.*, 27(2):1317–1320, September 1990.

[22] GM Rebeiz. Millimeter-wave and terahertz integrated circuit antennas. *Proceedings of the IEEE*, 80(11):1748–1770, 1992.

[23] T. Tils. *Design and 3-D electromagnetic modeling of terahertz waveguide mixers and components*. Dissertation (PhD thesis), KOSMA, 1. Physikalisches Institut der Universität zu Köln, 2006.

[24] T.G. Edwards. *Foundations for Microstrip Circuit Design*. J. Wiley & Sons, 1980.

[25] Michael Schultz. Private communication.

[26] C. Ye, Z. Ning, M. Shen, S. Cheng, and Z. Gan. Microstructure and dielectric properties of silicon nitride films deposited by electron cyclotron resonance plasma chemical vapor deposition. *Journal of Applied Physics*, 83(11):5978–5984, 1998.

[27] M. Brandt. *Superconducting Hot Electron Bolometers on Silicon Nitride Membranes for Terahertz Waveguide Mixers*. Dissertation (PHD thesis), KOSMA, 1. Physikalisches Institut der Universität zu Köln, 2004.

[28] T.G. Phillips and K.B. Jefferts. A low temperature bolometer heterodyne receiver for millimeter wave astronomy. *Rev. Sci. Instrum.*, 44:1009–1014, August 1973.

[29] E.M. Gershenzon, M.E. Gershenzon, G.N. Gol'tsman, A.D. Semenov, and A.V. Sergeev. Nonselective effect of electromagnetic radiation on a superconducting film in the resistive state. *JETP Lett.*, 36:296–299, October 1982.

[30] R. Barends, M. Hajenius, J. R. Gao, and T. M. Klapwijk. Current-induced vortex unbinding in bolometer mixers. *APL*, 87:263506, 2005.

[31] P. J. Burke. *High frequency electron dynamics in thin film superconductors and applications to fast, sensitive THz detectors*. PhD thesis, Yale University, 1997.

[32] B.S. Karasik and A.I. Elantiev. Noise temperature limit of a superconducting hot-electron bolometer mixer. *Appl. Phys. Lett.*, 68:853–855, February 1996.

[33] W. J. Skocpol, M. R. Beasley, and M. Tinkham. Self-heating hotspots in superconducting thin-film microbridges. *J. Appl. Phys.*, 45(9):4054–4066, 1974.

[34] WJ Skocpol and M. Tinkham. Fluctuations near superconducting phase transitions. *Reports on Progress in Physics*, 38(9):1049–1097, 1975.

[35] D.W. Floet. *Hotspot mixing in THz niobium superconducting hot electron bolometer mixers*. PhD thesis, Technische Universiteit Delft, 2001.

[36] T.M. Klapwijk, R. Barends, J. Gao, M. Hajenius, and J.J.A. Baselmans. Improved superconducting hot-electron bolometer devices for the THz range. *Proceedings of SPIE*, 5498:129, 2004.

[37] R. Barends, M. Hajenius, J. R. Gao, and T. M. Klapwijk. Direct correspondence between heb current-voltage characteristics and the current-dependent resistive transition. In *Proc. 16th Int. Symp. on Space Terahertz Technology*, 2005.

[38] H. Pothier, S. Guéron, N.O. Birge, D. Esteve, and MH Devoret. Energy distribution of electrons in an out-of-equilibrium metallic wire. *Zeitschrift für Physik B Condensed Matter*, 104(1):178–182, 1997.

[39] H. Pothier, S. Guéron, N.O. Birge, D. Esteve, and MH Devoret. Energy Distribution Function of Quasiparticles in Mesoscopic Wires. *Physical Review Letters*, 79:3490, 1997.

[40] EM Gershenzon, AI Elant'ev, GN Gol'tsman, BS Karasik, and SE Potoskuev. Intense electromagnetic radiation heating of electrons of a superconductor in the resistive state. *Sov. J. Low Temp. Phys*, 14:414–420, 1988.

[41] RS Nebosis, AD Semenov, YP Goussev, and KF Renk. Rigorous Analysis of a superconducting hot-electron bolometer mixer: theory and comparison with experiment. *Proceedings of the 7 thSymposium on Space Terahertz Technology, Charlottesville, Seiten*, pages 601–613, 1996.

[42] EM Gershenzon, GN Gol'tsman, IG Gogidze, YP Gusev, AI Elant'ev, BS Karasik, and AD Semenov. Millimeter and submillimeter range mixer based on electronic heating of superconducting films in the resistive state. *Sov. Phys. Superconductivity*, 3:1582, 1990.

[43] H. Araujo and G.J. White. Numerical modelling of the diffusion cooling response in superconducting hot-electron mixers. *IEEE Transactions on Applied Superconductivity*, 9(2):4229–4232, 1999.

[44] M. Hajenius, JJA Baselmans, JR Gao, TM Klapwijk, PAJ de Korte, B. Voronov, and G. Gol'tsman. Low noise NbN superconducting hot electron bolometer mixers at 1.9 and 2.5 THz. *Supercond. Sci. Technol*, 17:S224–S228, 2004.

[45] GR Boogaard, AH Verbruggen, W. Belzig, and TM Klapwijk. Resistance of superconducting nanowires connected to normal-metal leads. *Physical Review B*, 69(22):220503, 2004.

[46] P. Santhanam, S. Wind, and D.E. Prober. Localization, superconducting fluctuations, and superconductivity in thin films and narrow wires of aluminium. *Phys. Rev. B*, 35:3188–3206, March 1987.

[47] K.S. Il'in, I.I. Milostnaya, A.A. Verevkin, G.N. Gol'tsman, E.M. Gershenzon, and R. Sobolewski. Ultimate quantum efficiency of a superconducting hot-electron photodetector. *Appl. Phys. Lett.*, 73:3938–3940, December 1998.

[48] T. Berg, S. Cherednichenko, V. Drakinskiy, P. Khosropanah, H.F. Merkel, E.L. Kollberg, and J.W. Kooi. Stability of HEB receivers at THz frequencies. *Astronomical Structures and Mechanisms Technology. Edited by Antebi, Joseph; Lemke, Dietrich. Proceedings of the SPIE,*, 5498:605–615, 2004.

[49] H.C. Barshilia and KS Rajam. A Raman-scattering study on the interface structure of nanolayered and multilayer thin films grown by reactive dc magnetron sputtering. *Journal of Applied Physics*, 98(1):14311–14311, 2005.

[50] S.B. Kaplan. Acoustic matching of superconducting films to substrates. *Journal of Low Temperature Physics*, 37(3):343–365, 1979.

[51] J. Baubert, H. Merkel, M. Salez, and P. Khosropanah. A Hot Spot Model for Membrane-Based HEB Mixer. *Proceedings of the 14 thIntl. Symp. on Space Terahertz Technology*, pages 393–404, 2003.

[52] A.F Andreev. The thermal conductivity of the intermediate state in superconductors. *Sov. Phys. JETP*, 19:1228–1231, 1964.

[53] P. A. M Benistant, H. van Kempen, and P. Wyder. Direct Observation of Andreev Reflection. *Physical Review Letters*, 51(9):817–820, 1983.

[54] Muñoz, E. KOSMA technical report.

[55] Berkeley microfabrication laboratory, university of california, berkeley.

[56] M. Tinkham. *Introduction to Superconductivity*. McGraw-Hill International Editions, second edition edition, 1996.

[57] B. Chapman. *Glow Discharge Processes*. John Wiley & Sons, 1980.

[58] P. R. Broussard. *Superconducting Film Devices*.

[59] P. Yagoubov, G. Gol'tsman, B. Voronov, L. Seidman, V. Siomash, S. Cherednichenkov, and E. Gershenzon. The bandwidth of HEB mixers empoying ultrathin NbN films on sapphire substrate. In *Proc. 7th Int. Symp. on Space Terahertz Technology*, 1996.

[60] J.J.A. Baselmans, M. Hajenius, J.R. Gao, T.M. Klapwijk, P.A.J de Korte, B. Voronov, and G Gol'tsman. Doubling of sensitivity and bandwidth in phonon cooled hot electron bolometer mixers. *J. Appl. Phys.*, 84(11):1958–1961, March 2004.

[61] Y. Todokoro. Double-layer resist films for submicrometer electron-beam lithography. *Electron Devices, IEEE Transactions on*, 27(8):1443–1448, 1980.

[62] S. Yasin, DG Hasko, and H. Ahmed. Comparison of MIBK/IPA and water/IPA as PMMA developers for electron beam nanolithography. *Microelectronic Engineering*, 61:745–753, 2002.

[63] M. MOHSIN and J. M. G. COWIE. Enhanced sensitivity in the electron beam resist poly (methyl methacrylate) using improved solvent developer. *Polymer(Guildford)*, 29(12):2130–2135, 1988.

[64] DG Hasko, S. Yasin, and A. Mumtaz. Influence of developer and development conditions on the behavior of high molecular weight electron beam resists. *Journal of Vacuum Science & Technology B: Microelectronics and Nanometer Structures*, 18:3441, 2000.

[65] JS Papanu, DS Soane Soong, AT Bell, and DW Hess. Transport models for swelling and dissolution of thin polymer films. *Journal of Applied Polymer Science*, 38(5):859–885, 1989.

[66] Y. Uzawa, S. Miki, Z. Wang, A. Kawakami, M. Kroug, P. Yagoubov, and E. Kollberg. Performance of a quasi-optical NbN hot-electron bolometric mixer at terahertz frequencies. *Superconductor Science & Technology*, 15(1):141–145, 2002.

[67] J. D. R. Buchanan, T. P. A. Hase, B. K. Tanner, P. J. Chen, L. Gan, C. J. Powell, and W. F. Egelhoff. Anomalously large intermixing in aluminum–transition-metal bilayers. *Phys. Rev. B*, 66(10):104427, Sep 2002.

[68] CST Microwave Studio from CST GmbH, Bad Nauheimer Str. 19, D-64289 Darmstadt, Germany. Internet: www.cst.de.

[69] Rose Technology GmbH, Bergisch Gladbach, Germany.

[70] I. C*á*mara Mayorga, P. Muñoz Pradas, EA Michael, M. Mikulics, A. Schmitz, P. van der Wal, C. Kaseman, R. Güsten, K. Jacobs, M. Marso, H Lüth, and P. Kordoš. Terahertz photonic mixers as local oscillators for hot electron bolometer and superconductor-insulator-superconductor astronomical receivers. *Journal of Applied Physics*, 100(4):43116–43119, 2006.

[71] M. Philipp, U. U. Graf, A.Wagner-Gentner, D. Rabanus, and F. Lewen. Development of a compact 1.9 THz BWO local oscillator for GREAT,. *Int. J. of Infrared and Millimeter Waves*, sent for publication, 2006.

[72] M.C. Wiedner, S. Bedorf, F. Bielau, M. Emprechtinger, U. Graf, C. E. Honingh, K. Jacobs, P. Muñoz, M. Olbrich, D. Paulußen, K. Rettenbacher, G. Schmidt, O. Siebertz, J. Stutzki, and N. Volgenau. CONDOR — an astronomical heterodyne receiver at 1.25 – 1.5 THz. In *Union Radio Scientifique Internationale Proc. of the XXVIII General Assembly, New Delhi, India, 23 to 29 October*, 2005.

[73] Sven Bedorf. "private communication".

[74] G. Deutscher. Coherence length, proximity effect and fluctuations. In J. Evetts, editor, *Concise Encyclopedia of magnetic & superconducting materials*. Pergamon Press Ltd, 1992.

[75] A.A. Golubov. Superconducting superlattices and multilayers. In I. Bozovic, editor, *Proc. SPIE*, volume 215, page 353, Bellingham, WA, 1994.

[76] A.A. Golubov, E.P. Houwman, I.G. Gijsbertsen, V.M. Krasnov, J. Flokstra, H. Rogalla, and M.Yu. Kupriyanov. Proximity effect in superconductor-insulator-superconductor josephson tunnel junctions: Theory and experiment. *PRB*, 51:1073–1089, 1995.

[77] Y. B. Vachtomin, S.V. Antipov, S.N. Maslennikov, K.V. Smirnov, S.L. Polyakov, N.S. Kaurova, E.V. Grishina, B. M. Voronov, and G.N. Goltsman. Noise temperature measurements of NbN phononcooled hot electron bolometer mixers at 2.5 and 3.8 THz. In *Proc. 15th Int. Symp. on Space Terahertz Technology*, page 236, 2004.

[78] H.J. Spitzer. Preparation and superconducting properties of thin films of some binary transition metal alloy systems. *J. Vac. Sci. Technol.*, 8(1):184, 1971.

[79] Lei Yu, N. Newman, and J.M. Rowell. Measurement of the coherence length of sputtered $Nb_{0.62}Ti_{0.38}N$ thin films. *IEEE Transactions on Applied Superconductivity*, 12(2):1795–1798, 2002.

[80] M. Hajenius, Z.Q. Yang, J.J.A. Baselmans, and J.R. Gao. Lifetimes of NbN hot electron bolometer mixers. In *Proc. 16th Int. Symp. on Space Terahertz Technology*, 2005.

[81] K.R. Williams and R.S. Muller. Etch rates for micromachining processing. *IEEE Journal of microelectromechanical systems*, 5(4):256–269, 1996.

[82] W-Wax by Apiezon, Manchester, UK.

[83] M. Brandt, P. P. Muñoz, J. Stodolka, T. Tils, C. E. Honingh, and K. Jacobs. Superconducting hot electron bolometers on fused quartz and on freestanding silicon nitride membrane strips. In *Proc. of the 6th European Conference on Applied Superconductivity*, pages 2978–2985. Institute of Physics Publishing, 2003.

[84] GM Rebeiz, DP Kasilingam, Y. Guo, PA Stimson, and DB Rutledge. Monolithic millimeter-wave two-dimensional horn imaging arrays. *Antennas and Propagation, IEEE Transactions on*, 38(9):1473–1482, 1990.

[85] P. H. Siegel, R.P. Smith, M.C. Graidis, and S.C Martin. 2.5-THz GaAs monolithic membrane-diode mixer. *IEEE Trans. Micowave Theory and Techniques*, 47(5):596–604, May 1999.

[86] Dr. Voker Klocke Nanotechnology, Aachen, Germany.

[87] A. R. Kerr. Suggestions for revised definitions of noise quantities, including quantum effects. *Microwave Theory and Techniques, IEEE Transactions on*, 47(3):325–329, Mar 1999.

[88] H. B. Callen and T. A. Welton. Irreversibility and Generalized Noise. *Phys. Rev.*, 83(1):34–40, July 1951.

[89] J. R. Tucker and M. J. Feldman. Quantum detection at millimeter wavelenghts. *Rev. Mod. Phys.*, 57(4):1055–1113, 1985.

[90] A. Karpov, J. Blondel, M. Voss, and K.H. Gundlach. A three photon noise SIS heterodyne receiver at submillimeter wavelength. *Applied Superconductivity, IEEE Transactions on*, 9(2):4456–4459, 1999.

[91] J. Kawamura, J. Chen, D. Miller, J. Kooi, J. Zmuidzinas, B. Bumble, H. G. LeDuc, and J. A. Stern. Low-noise submillimeter-wave NbTiN superconducting tunnel junction mixers. *Appl. Phys. Lett.*, 75(25):4013–4015, 1999.

[92] Zitex G 108, Saint-Gobain Performance Plastics. http://www.labpure.com/nzitexmembranes.html, 2004.

[93] J. Ward, F. Maiwald, G. Chattopadhyay, E. Schlecht, A. Maestrini, J. Gill, and I. Mehdi. 1400–1900 GHz Local Oscillators for the Herschel

Space Observatory. *14th International Symposium on Space Terahertz Technology*, pages 94–101, 2003.

[94] J. Stutzki, U.U. Graf, C.E. Honingh, K. Jacobs, R. Schieder, and O. Siebertz. Terahertz receivers for astronomy. In IEEE Proc., editor, *Proc. of the IRMMW-THz 2005*, pages 403–404 vol. 2, 2005.

[95] Martina Wiedner. Private communication.

[96] RPG Radiometer Physics GmbH, D-53340 Meckenheim, Germany, Internet: www.radiometer-physics.de.

[97] Virginia Diodes Inc., Charlottesville, VA, USA, Internet: www.virginiadiodes.com.

[98] Armin Wagner. *PhD Thesis in preparation*. Dissertation (PhD thesis), KOSMA, 1. Physikalisches Institut der Universität zu Köln, 2006.

[99] P.D. Potter. A new horn antenna with suppressed sidelobes and equal beamwidths. *Microwave J*, 6(6):71–78, 1963.

[100] A. K. Rettenbacher. *Entwurf und Aufbau der Optik für den 1.4 THz-Empfänger CONDOR*. Diplomarbeit (degree in physics), KOSMA, 1. Physikalisches Institut der Universität zu Köln, 2004.

[101] A.D. Semenov, H. Richter, K. Smirnov, B. Voronov, G.N. Gol'tsman, and H.W. Hübers. The development of terahertz superconducting hot-electron bolometric mixers. *Supercond. Sci. Technol.*, 17:436–439, April 2004.

[102] S. Cherednichenko, M. Kroug, H. Merkel, P. Khosropanah, A. Adam, E. Kollberg, D. Loudkov, G. Gol'tsman, B. Voronov, H. Richter, and H.W. Hübers. 1.6 THz heterodyne receiver for the far infraed space telescope. *Physica C*, 372–376:427–431, 2002.

[103] H. Ekström et al. Superconducting bolometric mixer. *IEEE Microw. Guid. Wave Lett.*, 4:253, 1994.

[104] P. Yagoubov, M. Kroug, H. Merkel, E. Kollberg, G. Gol'tsman, S. Svechnikov, and E. Gershenon. Noise temperature and local oscillator power requirement of NbN phonon-cooled hot electron bolometric mixers at terahertz frequencies. *Appl. Phys. Lett.*, 73(19):2814–2816, November 1998.

[105] J. Kawamura, C.Y.E. Tong, R. Blundell, DC Papa, TR Hunter, F. Patt, G. Gol'tsman, and E. Gershenzon. Terahertz-frequency waveguide NbN hot-electron bolometer mixer. *Applied Superconductivity, IEEE Transactions on*, 11(1):952–954, 2001.

[106] D. W. Allan. Statistics of Atomic Frequency Standards. *Proc. IEEE*, 54(2):221–230, 1969.

[107] R. Schieder. Characterization and measurement of system stability. *SPIE, Instrumentation for Submillimeter Spectroscopy*, 598, 1985.

[108] V. Ossenkopf. A unified allan variance computation scheme. 2003, unpublished.

Danksagung

An erster Stelle möchte ich Herrn Professor Dr. Jürgen Stutzki danken, der mir die Gelegenheit gab, diese Arbeit am I. Physikalischen Institut der Universität zu Köln durchzuführen.

Professor Dr. Jan Jolie erklärte sich freundlicherweise bereit, das Zweitgutachten zu erstellen. Außerdem bedanke ich mich bei Professor Dr. Susanne Crewell für die Übernahme des Prüfungsvorsitzes.

Dr. Karl Jacobs und Dr. Netty Honingh danke ich für ihre Rundumhilfe, Beratung in schwierigen Momenten und Ihr Da-Sein. Ferner danke ich ihnen für die umfassende Unterstützung bei der Endfassung und Korrektur dieser Arbeit.

Außerdem möchte ich mich bei Dr. Bedorf für die Bereitstellung der ultradünnen NbTiN Filmen bedanken, sowie bei allen anderen Kollegen der SIS & HEB-Gruppe und allen Mitarbeitern des I. Physikalischen Instituts, die mich in meiner Zeit hier begleitet haben und für eine gute Arbeitsatmosphäre mitgesorgt haben.

Außerhalb des Instituts möchte ich mich besonders bei Iván Cámara Mayorga, mit dem ich wunderbare Mess-Marathons gefeiert habe, die zum Entstehen meines ersten Papers (als Koautor) geführt haben.

Ganz besonderer Dank gilt natürlich meinen Eltern, meine Freunde außerhalb des Instituts und insbesondere meiner geliebten Meditationsmeisterin, ohne deren selbstlose Unterstützung dieses Studium nicht möglich gewesen wäre (oder zumindest nicht so freudig).

Diese Arbeit wurde im Rahmen des Sonderforschungsbereichs 494 „Die Entwicklung der Interstellaren Materie: Terahertz-Spektroskopie in Weltall und Labor" angefertigt und durch die Deutsche Forschungsgemeinschaft gefördert.

Teilpublikationen:

[1] P. P. Muñoz, S. Bedorf, M. Brandt, T. Tils, N. Honingh, and K. Jacobs. THz waveguide mixers with NbTiN HEBs on silicon nitride membranes. In *IEEE Microwave and wireless components letters*, vol. 16, pp. 606–608, 2006.

[2] I. Cámara Mayorga, P. Muñoz Pradas, E. A. Michael, M. Mikulics, A. Schmitz, P. van der Wal, C. Kaseman, R. Güsten, K. Jacobs, M. Marso, H. Lüth, and P. Kordos. Terahertz photonic mixers as local oscillators for hot electron bolometer (HEB) and superconductor-insulator-superconductor (SIS) astronomical receivers. In *J. Appl. Phys.*, vol. 100, pp. 43116–43119 , 2006.

[3] M.C. Wiedner, S. Bedorf, F. Bielau, M. Emprechtinger, U. Graf, C. E. Honingh, K. Jacobs, P. Muñoz, M. Olbrich, D. Paulußen, K. Rettenbacher, G. Schmidt, O. Siebertz, J. Stutzki, and N. Volgenau. CONDOR — an astronomical heterodyne receiver at 1.25 – 1.5 THz. In *Union Radio Scientifique, Internationale Proc. of the XXVIII General Assembly*, New Delhi, India, 23 to 29 October, 2005.

[4] P. Muñoz, S. Bedorf, M. Brandt, T. Tils, M. Wiedner, M. Brüll, N. Honingh, and K. Jacobs. Phonon-cooled hot electron bolometers on freestanding 2-μm Si_3N_4 membranes for THz applications. In *Proc. 15th Int. Symp. on Space Terahertz Techn.*, 2004.

[5] P. Muñoz, S. Bedorf, M. Brandt, T. Tils, N. Honingh, and K. Jacobs. Fabrication and characterization of phonon-cooled hot-electron bolometers on freestanding 2-μm silicon nitride membranes for THz applications. In *Proc. SPIE Astronomical Telescopes and Instrumentation*, volume 5498, pages 834–841, 2004.

[6] S. Bedorf, P. Muñoz, M. Brandt, P. Pütz, N. Honingh, and K. Jacobs. Development of phonon-cooled NbTiN HEB heterodyne mixers for THz

applications. In *Digest 29th Int. Conf. on Infrared and Millimeter Waves and 12th Int. Conf. on Terahertz Electronics*, pages 455–456, 2004.

[7] M. Brandt, P. P. Muñoz, J. Stodolka, T. Tils, C. E. Honingh, and K. Jacobs. Superconducting hot electron bolometers on fused quartz and on freestanding silicon nitride membrane strips. In *Proc. of the 6th European Conference on Applied Superconductivity*, pages 2978–2985. Institute of Physics Publishing, 2003.

Erklärung:

Ich versichere, dass ich die von mir vorgelegte Dissertation selbständig angefertigt, die benutzten Quellen und Hilfsmittel vollständig angegeben und die Stellen der Arbeit - einschließlich Tabellen, Karten und Abbildungen -, die anderen Werken im Wortlaut oder dem Sinn nach entnommen sind, in jedem Einzelfall als Entlehnung kenntlich gemacht habe; dass diese Dissertation noch keiner anderen Fakultät oder Universität zur Prüfung vorgelegen hat; dass sie - abgesehen von unten angegebenen Teilpublikationen - noch nicht veröffentlicht worden ist sowie, dass ich eine solche Veröffentlichung vor Abschluss des Promotionsverfahrens nicht vornehmen werde. Die Bestimmungen dieser Promotionsordnung sind mir bekannt. Die von mir vorgelegte Dissertation ist von Prof. Dr. Stutzki betreut worden.

Köln, 23. April 2007